The Dissertation Committee for Xiaolei Song
certifies that this is the approved version of the following dissertation:

Application of Fourier Finite Differences and Lowrank Approximation Method for Seismic Modeling and Subsalt Imaging

Committee:

Sergey B. Fomel, Supervisor

Paul Fowler

Omar Ghattas

Paul Stoffa

Lexing Ying

Application of Fourier Finite Differences and Lowrank Approximation Method for Seismic Modeling and Subsalt Imaging

by

Xiaolei Song, B.S.; M.S.

DISSERTATION

Presented to the Faculty of the Graduate School of

The University of Texas at Austin

in Partial Fulfillment

of the Requirements

for the Degree of

DOCTOR OF PHILOSOPHY

THE UNIVERSITY OF TEXAS AT AUSTIN

December 2012

Dedicated to my family for their patience and encouragement.

Acknowledgments

During the last semester of the high school, I started to think about my future major. In the boarding high school, I felt my life totally isolated from the big world outside. I had no idea what major to pick up for the university. I guessed that applied mathematics might be the right choice, since mathematics is the language of science. However, finally, I was admitted by the Geophysics Department of Peking University. Before that moment, I never heard of the term: geophysics. After an orientation seminar by my undergraduate advisor, Zijian Ni, in the first week at Geophysics Department of Peking University, I got to know that geophysics is the study of the Earth using quantitative physical methods and that it plays an important role in modern science development. Also, geophysics is applied to crucial societal needs, such as mineral and hydrocarbon resources, mitigation of natural hazards, and environmental protection. Most of the courses required by the department were closely related to math, physics and computer science, which were my favorite classes during the high school. So I decided to stay in the geophyscis major. Peking university encourages undergraduate students to start doing research. In my junior year, thanks to two advisors, Weiying Zhong and Zijian Ni, I applied for President's Undergraduate Research Fellowship. Thanks to Dr. Qinghua Huang's guidence, I worked on the effect of rainfall infiltration process on apparent resistivity of the Earth. That was my first experience with modeling. Then I got interested in seismic modeling. With Dr. Huang's advice, I began my Master's study with Dr. Xiaofei Chen. I worked in the Computational Geodynamics Laboratory in Peking Universtiy. With Dr. Chen's advising, I mainly focused on seismic wave propagation in 2D heterogeneous media.

During my Master's program, I fortunately got a lot of help from other MS and PhD students, like Wei Zhang, Haiming Zhang, Rongqiang Wei, Xiaofen Jia, Xiaofei Liang, Hui Huang, Jin Ge, Hejun Zhu, Qiming Liu, Jian Wen and others. They helped and influenced me a lot. During that time, one of my best friends, Weichao Tu, was working on her PhD degree at University of Colorado in Boulder. She called me several times, talking about her life in US and encouraged me to apply for PhD study abroad. Taking some advice from Dr. Xiaofei Chen, Dr. Qinghua Huang and Dr. Jieyuan Ning, I started my application to US universities. In my last year as a MS student, my research interest transfered from global seismology to exploration seismology. Hejun Zhu recommended Dr. Sergey Fomel. I have to say, it was one of the most right things I ever did in my life that I contacted Dr. Sergey Fomel. And it was one of the most fortunate things that ever happened to me that I was accepted by him. I would like to thank my supervisor Sergey Fomel to offer me the opportunity to learn at UT and work with him. Dr. Fomel finds our group funding, develops and maintains our software: Madagascar. He teaches some of the most rewarding courses. Most important, he promotes the research work of our whole group. I've never had to hesitate to stop by his office to ask questions or discuss ideas. Whenever I met challenges, Dr Fomel has always helped to provide advice, suggestions, or ideas. I am heartily thankful to my supervisor, Sergey Fomel. His guidence and support enabled me to develop an understanding of my research subject and encouraged me to finish the subject. He has been not only a great supervisor, but also a true counselor, guide, colleague, and friend.

During my study at UT, several other professors have provided guidance as well. I would like to first thank Dr. Lexing Ying, a professor in Mathematics Department. After I arrived at UT in 2008, Dr. Fomel introduced me to Dr. Ying. They

already started wave extrapolation with lowrank method. And I joined them at that time. Dr. Ying has been generously helpful and inspired me to try new ideas and solve problems. During these years, each time I discussed with Dr. Ying, I could learn from him. Next I would like to thank Dr. Paul Stoffa. Dr. Stoffa has been providing me good suggestions about my research on Fourier finite difference (FFD) and Reverse-time migration (RTM). I would also like to thank Dr. Mrinal Sen and Dr. Omar Ghattas. Taking their courses on inverse theory has been truly useful for my research as well as understanding others' work. I would also like to thank Paul Fowler, who served as my outside committee member. I had a lot of useful discussions with him on the numerical methods I presented in the dissertation. I would like to thank Björn Engquist. I learnt a lot about analysis of partial differential equations (PDEs) from his course "Advanced Numerical Treatment of Differential Equations". And I also benefited from discussions on pseudo-spectral methods with him. I would like to thank Tariq Alkhalifah and Xuxin Ma at King Abdullah University of Science and Technology (KAUST) for hosting me during my visit. During that stay at KAUST, I worked with Tariq and completed most of the work on pseudo-acoustic orthorhombic modeling.

In the Department of Geological Sciences, I would also like to thank Steve Grand, Kyle Spikes, Peter Flemings, Ronald Steel, William Fisher, and Philip Guerrero.

At the Bureau of Economic Geology, I would like to thank Bob Hardage, Stephen Ruppel, Douglas McCowan, Jennifer Logan, Karl Schleicher, Damian Markez, and Lorena Moscardelli.

Within our group (now the Texas Consortium for Computational Seismology—

TCCS), I would like to give special thanks to William Burnett, Vladimir Bashkardin and Yang Liu. I would also like to thank Jules Browaeys, Hesam Kazemeini, Alexander Klokov, Roman Kazinnik, Jingwei Hu, Siwei Li, Yihua Cai, Simin Huang, Guochang Liu, Min Zhang, Maoshan Chen, Shujuan Guo, Jiubing Cheng, Parvaneh Karimi, Shaunak Ghosh, and Salah Alhadab. Outside of our group, I would also like to thank Long Jin, Yang Liu, Yi Tao, Paul Mann, Chunlei Chu, Chaoshun Hu, Henry Campos, Rui Zhang, Gang Luo, and Na Shan at the Institute for Geophysics. I would like to thank our TCCS sponsors for providing funding or data. I would like to thank Chevron Energy Technology Company for publishing permission for the variable density FFD method. I would like to thank BP for releasing benchmark synthetic models as well as permission of real data set from the Gulf of Mexico. I have managed to complete four internships during my PhD studies, each of which has provided practical experience and opportunities to work with some of the best geophysicists in industry. I would like to thank all of these companies for providing me with internship opportunities, and give special thanks to mentors and co-workers along the way: Marta Woodward, Konstantin Osypov, Feng Qiao, Sichao Chen and Xin Cheng at WesternGeco; Anatoly Baumstein, Partha Routh, David McAdow, Rongrong Lu, Raffaella Montelli, Sunwoong Lee, Kaushik Bandyopadhyay, John Anderson,Spyros Lazaratos, Lijian Tan, and Xiaojun Huang at ExxonMobil; Kurt Nihei, Joseph Stefani, Dimitri Bevc, Guojian Shan, and Linbin Zhang at Chevron; and John Etgen, Joe Dellinger, Frederic Billette, Chunlei Chu, Ray Barrett, Imtiaz Ahmed, Adeyemi Arogunmati, Petr Jilek, Zhiyong Jiang, Chandan Kumar, Jin Lee, David Lewis, Rachel Murphy, Rene Salmon, Rusty Sandschaper, Larry Sorensen, Doug Stauber, Jean-Paul van Gestel, Patricia Walker, Jianhua Yu, Min Zhou, Yu Zhou at BP.

I would also like to thank a long list of professors and friends from Peking

University who had tremendous influence on me in geophysics: Xiaofei Chen, Qinghua Huang, Yongshun Chen, Jieyuan Ning, Tianyue Hu, Jun Lei, Yonghong Zhao, Yongen Cai, Shiyong Zhou, Jinzhen An, Yongge Feng, Zengxi Ge, Yanbin Wang, Wei Zhang, Haiming Zhang, Rongqiang Wei, Xiaofen Jia, Hui Huang, Qiming Liu, Hejun Zhu, Yang Luo, Chao Shi, Ge Jin, Han Li and Xiang He. I want to add special thanks to my roommates and best friends in Beijing: Tingting Wang, Weichao Tu and Shuo Yao. I still remember the tough time in girls' dormitory where we worked together on mechanics and learned calculus by ourselves as freshmen.

Next, I would like to thank my parents. My father, Zhiqiang Song, is the source of my earliest interests in mathematics. He answered most of my questions when I was in primary school and interested in Mathematical Olympiad. He encouraged me to apply to Peking University and convinced me to study science there and abroad in US. My mother, Yuhua Wang, started to teach me English when I was five. She said that I would find English quite useful one day. And she is more than right. I would also like to thank my parents-in-law: Bo Sun and Linna Xi. They treat me as a daughter of their own. And last, the most important person I would like to thank is my husband, Ning Sun. We met in high school as classmates and went to Peking University together in 2002. Before we held the wedding in 2011, we had known each other for over 10 years. He understands me even better than myself. I appreciate his encouragement, trust, faith and love during my study in Austin for a Ph.D.

When I was young, I thought success could mainly be achieved individually from hard work. As I grew up through these years, I realized how lucky I was, surrounded by so many great friends and helpful mentors. My family members, professors, friends, colleagues, and mentors helped and supported me all the way. Without them, this dissertation would not exist, and I am very grateful for all of

their help.

XIAOLEI SONG

The University of Texas at Austin

December 2012

Application of Fourier Finite Differences and Lowrank Approximation Method for Seismic Modeling and Subsalt Imaging

Publication No. _____

Xiaolei Song, Ph.D.

The University of Texas at Austin, 2012

Supervisor: Sergey B. Fomel

Nowadays, subsalt oil and gas exploration is drawing more and more attention from the hydrocarbon industry. Hydrocarbon exploitation requires detailed geological information beneath the surface. Seismic imaging is a powerful tool employed by the hydrocarbon industry to provide subsurface characterization and monitoring information. Traditional wave-equation migration algorithms are based on the one-way-in-depth propagation using the scalar wave equation. These algorithms focus on downward continuing the upcoming waves. However, it is still really difficult for conventional seismic imaging methods, which have dip limitations, to get a correct image for the edge and shape of the salt body and the corresponding subsalt structure. The dip limitation problem in seismic imaging can be solved completely by switching to Reverse-Time Migration (RTM). Unlike old methods, which deal with the one-way wave equation, RTM propagator is two-way and, as a result, it no longer imposes dip limitations on the image. It can also handle complex waveforms, including pris-

matic waves. Therefore it is a powerful tool for subsalt imaging. RTM involves wave extrapolation forward and backward in time. In order to accurately and efficiently extrapolate the wavefield in heterogeneous media, I develop three novel methods for seismic wave modeling in both isotropic and tilted transversely isotropic (TTI) media. These methods overcome the space-wavenumber mixed-domain problem when solving the acoustic two-way wave equation. The first method involves cascading a Fourier Transform operator and a finite difference (FD) operator to form a chain operator: Fourier Finite Differences (FFD). The second method is lowrank finite differences (LFD), whose FD schemes are derived from the lowrank approximation of the mixed-domain operator and are represented using adapted coefficients. The third method is lowrank Fourier finite differences (LFFD), which use LFD to improve the accuracy of TTI FFD mothod. The first method, FFD, may have an advantage in efficiency, because it uses only one pair of multidimensional forward and inverse FFTs (fast Fourier transforms) per time step. The second method, LFD, as an accurate FD method, is free of FFTs and in return more suitable for massively parallel computing. It can also be applied to the FFD method to reduce the dispersion in TTI case, which results in the third method, LFFD. LFD and LFFD are based on lowrank approximation which is a general method to handle mixed-domain operators and can be easily applied to more complicated mixed-domain operators. I show pseudo-acoustic modeling in orthorhombic media by lowrank approximation as an example.

Table of Contents

List of Tables

List of Figures

Chapter 1

Introduction

SUBSALT HYDROCARBON EXPLORATION

In geology and exploration geophysics, salt means "halite(NaCl) and other saline minerals deposited as a result of evaporation. Salt has low density (2.1–2.6 g/cm^3, average 2.22 g/cm^3) and high plasticity that results in the creation of salt pillows, domes, walls and allochthonous features and deformation of sediments"(Sheriff, 2002). In the Gulf of Mexico (GOM), many salt bodies were formed as the Gulf separated from the Atlantic Ocean. As water evaporated, salt sank to the bottom of the sea, resulting in thick salt beds. Because of lower density than that of the sediments around it, salt tends to flow up in geological time. Finally, salt beds led to giant salt domes through migration and deformation. In the rocks below or next to salt bodies, carbon rich sediments generated oil and gas (Jackson and Talbot, 1986).

Nowadays, subsalt oil and gas exploration is drawing more and more attention from the hydrocarbon industry. For example, in the Gulf of Mexico (GOM), the Thunder Horse oilfield was the largest of the subsalt discoveries by BP (25% co-owned by Exxon) in 1999. It is now the largest field in the GOM, producing 250,000 barrels of oil and 200 MMCF(million cubic feet) of gas per day (Technology, 2009). On September 5th 2006, Chevron Corporation announced that it successfully completed a record setting production test on the Jack #2 well in the GOM. The Jack #2 well, as

a joint venture between Chevron Corporation (50%), StatoilHydro (25%) and Devon Energy (25%), was drilled to a total of depth of 28,175 feet, breaking Chevron's 2004 Tahiti well test record as the deepest successful well test in the GOM. During the test, the well sustained a flow rate of more than 6,000 barrels of crude oil per day with the test representing approximately 40 percent of the total net pay measured in the Jack #2 well. The maximum estimation of the reservoir volume, 15 billion barrels, represents half of the current estimate of U.S. reserves. (Chevron, 2006). BP made another giant oil discovery: the Tiber Oil Field (usually considered to contain 250 million barrels) in the GOM on September 2nd 2009, reaffirming the Gulf's strategic importance to the industry (REUTERS, 2009). In 2011, Exxon Mobil Corp. found the equivalent of 700 million barrels of oil beneath the Gulf of Mexico. ExxonMobil's Hadrian discovery is the biggest discovery in the region since 1999 (Carroll, 2011).

Hydrocarbon exploitation requires detailed geological information beneath the surface. Seismic imaging is a powerful tool employed by the hydrocarbon industry to provide subsurface characterization and monitoring information. The main purpose of reflection imaging is to migrate reflection events to the position of reflectors. That is why it has another name *migration*. Traditional wave-equation migration algorithms are based on the one-way-in-depth propagation using the scalar wave equation (Loewenthal et al., 1976b; Claerbout, 1985). These algorithms focus on downward continuing the recorded upcoming waves. The first finite-difference migration algorithm introduced to petroleum industry was based on the parabolic approximation to the acoustic wave equation (Claerbout and Doherty, 1972). For waves propagating downward or close to downward, the one-way equation behaves very similarly to the two-way acoustic equation, because it is accurate in a restricted range of angles. Plus,

it supports multi-pathing, and its computational cost is affordable for the petroleum industry (Biondi, 2006). In practice, these algorithms suffer from dip limitations. However, because of the above allochthonous features and deformations, a salt body may have very steep edges (Figure 1.1) which reflect seismic waves to generate turning waves. One recipe to handle the dip limitation is Riemannian wavefield extrapolation (Sava and Fomel, 2005; Shragge, 2008), which generalizes one-way wavefield extrapolation to non-Cartesian coordinate systems. But it is still exceedingly difficult for conventional seismic imaging methods, which have dip limitations, to get a correct image for edges and shapes of salt bodies and the corresponding subsalt structures. Furthermore, seismic velocity in salt (about 4–5 km/s) is significantly higher than that in the surrounding sediment rocks (2–4 km/s). Therefore, subsalt velocity estimation, as a required step in seismic data analysis, is crucially important.

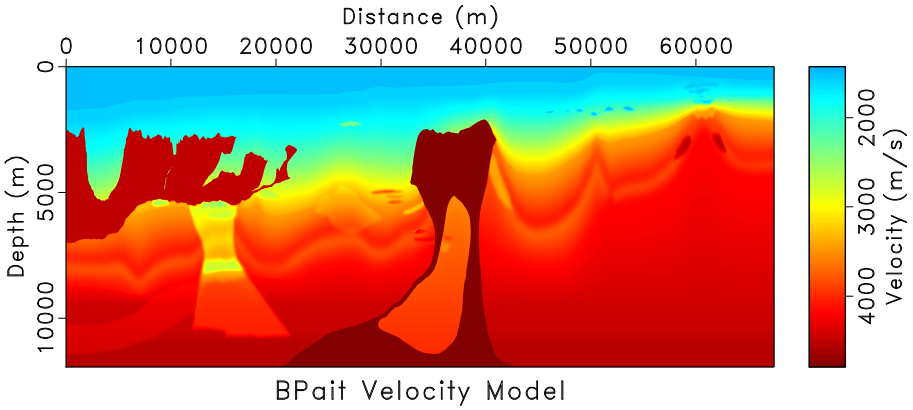

Figure 1.1: BP 2004 Velocity Model chapter-introduction/bpmodel bpaitvel

REVERSE-TIME MIGRATION

The dip limitation problem in seismic imaging can be solved by switching to Reverse-Time Migration (RTM) (Baysal et al., 1983; McMechan, 1983; Whitmore, 1983; Levin, 1984). Unlike conventional methods, which deal with the one-way wave equation, RTM propagator is two-way and, as a result, it no longer imposes dip limitations on the image. In recent years, RTM is attracting more and more attention as the most powerful depth-imaging method (Biondi and Shan, 2002; Mulder and Plessix, 2004; Yoon et al., 2004; Symes, 2007; Chattopadhyay and McMechan, 2008; Fletcher et al., 2009; Fowler et al., 2010a; Liu et al., 2011; Xu et al., 2011). RTM can correctly handle complex structures, including subsalt areas. It can also handle complex waveforms, including prismatic waves. Therefore it is a powerful tool for subsalt imaging. Another advantage of the two-way propagator is its connection to Full Waveform Inversion (FWI) for velocity estimation in geologically complex areas (Tarantola, 1984; Symes, 2008).

Despite virtues listed above, RTM is extremely expensive in both computing resources and computational time due to the forward and time-reversed wavefield propagation using small time steps to avoid instability and reduce dispersion. In order to overcome these problems, a lot of research has been done to develop and analyze high-order schemes of the finite difference method (Wu et al., 1996).

Meanwhile, many alternative algorithms are being developed for seismic wave extrapolation in variable velocity media. In recent years, thanks to advances in supercomputer technology, spectral methods have become feasible for large-scale problems

and are attracting more and more attention. Mast et al. (2001) provided a simplified derivation of the k-space method for computation of ultrasonic wave propagation in tissue, which efficiently accounts for sound speed and density variations, while being able to handle realistic absorption effects. In the k-space method, dispersion errors from the second-order time integration operator are compensated for by a modified spectral operator in the wavenumber domain. This correction is exact for a medium with uniform velocity. Tabei et al. (2002) presented an adaptation of the k-space method, which solves coupled first-order differential equations for wave propagation in inhomogeneous media. Soubaras and Zhang (2008) introduced two-step explicit marching method based on a high-order differential operator, which allows a large extrapolation time step by solving a coefficients optimization problem. Zhang and Zhang (2009) proposed a one-step extrapolation method by introducing a square-root operator. This method can formulate the two-way wave equation as a first-order partial differential equation in time similar to the one-way wave equation. Etgen and Brandsberg-Dahl (2009) modified the Fourier transform of the Laplacian operator to compensate exactly for the error resulting from the second-order FD on the time axis, so as to reduce the grid dispersion that appears in conventional pseudo-spectral methods (Gazdag, 1981; Reshef et al., 1988). A set of dispersion-corrected Laplacian operators for the range of model velocities are constructed and interpolated to allow for seismic modeling in heterogeneous media. This approach can be viewed as an extension of the k-space method from constant to variable velocity. Fowler et al. (2010a) provided an accurate VTI P-wave modeling method with coupled second-order pseudo-acoustic equations. Pestana and Stoffa (2010) presented an application of Rapid Expansion Method (REM) (Tal-Ezer et al., 1987) for forward modeling with one-step time evolution algorithm and RTM with recursive time stepping algorithm.

Chu and Stoffa (2008) replaced the Taylor series expansion with optimized polynomials to enhance stability for time-stepping schemes. Chu and Stoffa (2011) extended the pseudoanalytical method to solve the elastic wave equation on staggered grids. Chu et al. (2011) propose new pure acoustic TTI wave equations, which can be directly solved using either the finite-difference method or the pseudospectral method to produce highly accurate images.

Reverse-Time Migration was first proposed as a method for post-stack migration (Baysal et al., 1983; Whitmore, 1983). The purpose of post-stack migration, based on the exploding reflector concept, is to recover the seismic wavefield at zero time ($t = 0$), where it can give the location and strength of the reflectors (Loewenthal et al., 1976a). Reverse time migration, instead of implementing a conventional depth extrapolation, is formulated as another wave propagation problem. The waves are generated from the time reversed stacked zero-offset section $P(x, z = 0, t)$, which functions as a surface boundary condition. So it is a reverse time extrapolation of stacked data, in which it seems appropriate to use wave equations suppressing internal reflections (Baysal et al., 1984).

In the prestack case, one can propagate the recorded wavefield in a presumed-correct velocity model and form an image by measuring the wave amplitude when it is coincident with the shot wavefield (Etgen, 1986). In other words, the reflectors form at locations, where, at some specific time during back propagation, the shot wavefield and the receiver wavefield coincide.

To migrate a shot record $Q(x, y; x_s, y_s; t)$, one needs to propagate the forward wavefield $p_F(\mathbf{x}; t)$ originating at the source location $(x_s, y_s, z_s = 0)$:

$$\left(\frac{1}{v^2}\frac{\partial^2}{\partial t^2} - \nabla^2\right) p_F(\mathbf{x}; t) = \delta(\mathbf{x} - \mathbf{x}_s) f(t)\,, \tag{1.1}$$

where $v = v(x, y, z)$ is the velocity, $f(t)$ is the source term, and $\nabla^2 = \frac{\partial^2}{\partial x^2} + \frac{\partial^2}{\partial y^2} + \frac{\partial^2}{\partial z^2}$ is the Laplacian operator. And one also needs to propagate backwards in time the recorded receiver wavefield $p_B(\mathbf{x}, t)$:

$$\begin{cases} \left(\frac{1}{v^2}\frac{\partial^2}{\partial t^2} - \nabla^2\right) p_B(\mathbf{x}; t) = 0, \\ p_B(x, y, z = 0; t) = Q(x, y; x_s, y_s; t) \end{cases} \tag{1.2}$$

To obtain a common shot image with correct migration amplitude, one can apply the deconvolution imaging condition (Claerbout and Doherty, 1970),

$$I(\mathbf{x}) = \int \hat{p}_B(\mathbf{x}; \omega)\hat{p}_F^{-1}(\mathbf{x}; \omega) d\omega\ . \tag{1.3}$$

However, this imaging condition is difficult to implement in the time domain for RTM. Bleistein et al. (2005) recasted the deconvolution imaging condition as a correlation imaging formula by averaging over incidence angles at the image point and then transforming into an integral over source locations at the upper surface. A practical and inexpensive alternative in practice is to multiply the two wavefields together; i.e. build the cross-correlation:

$$I(\mathbf{x}) = \int p_B(\mathbf{x}; t) p_F(\mathbf{x}; t) dt\ . \tag{1.4}$$

The core algorithm is the cross-correlation of these above two fields at the same time level, one via forward computation ($p_F(\mathbf{x}; t)$) and the other from backward propagation($p_B(\mathbf{x}; t)$). It is natural to do the forward computation directly, but $p_F(\mathbf{x}; t)$ must be accessible during the backward recursion (Symes, 2007).

The most popular and straightforward way to implement reverse-time migration is the method of explicit finite differences, which has dispersion and stability conditions for space grid sizes (Δx,Δy,Δz) and time-step length (Δt) (Wu et al., 1996; Liu and Sen, 2009). The choice of maximum grid spacing $h_{max} = \max(\Delta x, \Delta y, \Delta z)$ depends on the grid dispersion condition:

$$h_{max} \leq \frac{v_{min}}{p_h \, f_{max}} \,, \tag{1.5}$$

where f_{max} is the maximum frequency, v_{min} is the minimum velocity, and $p_h \geq 2$ is the number of samples per wavelength, which is related to the order of the Finite Difference scheme in space. The dispersion condition in time is

$$\Delta t \leq \frac{1}{p_t \, f_{max}} \,, \tag{1.6}$$

where $p_t \geq 2$ is the number of samples per period, which is related to the order of scheme chosen for Finite Difference in time. The stability condition for the scheme can be expressed (Mufti et al., 1996) as

$$\Delta t \leq \frac{a \, \bar{h}}{v_{max}} \,, \tag{1.7}$$

with

$$\bar{h} = \sqrt{\frac{3}{\frac{1}{\Delta x^2} + \frac{1}{\Delta y^2} + \frac{1}{\Delta z^2}}} \,,$$

where v_{max} is the maximum velocity and a is a parameter determined by the order of scheme in space. Considering both conditions 1.6 and 1.7, we can obtain upper limit for Δt

$$\Delta t \leq \min\left(\frac{1}{p_t \, f_{max}}, \frac{a \, \bar{h}}{v_{max}}\right) . \tag{1.8}$$

For example, given $f_{max} = 30$ Hz, $\bar{h} = 15$ m, $p_t = 2$, $v_{max} = 5$ km/s, $a = 0.5$ (4-th order scheme), one can infer that for the upper limit for Δt is about 1.7 ms.

However, the Nyquist sampling is $\frac{1}{60} \approx 17$ ms, 10 times of Δt. For very large applications, such as 3D RTM, the out-of-order access to forward computed fields and the upper limit for Δt and h cause the required storage for $p_F(\mathbf{x}; t)$ to be so large that the implementation has to use hard-disk input/output, which is the slowest level of memory hierarchy. Large amounts of required memory and faded performance by slow memory access is the reason why RTM was not appealing to industry in the past. However, in recent years, due to rapid and steady development of computer hardware, the memory requirement is no longer an unsurmountable obstacle. Advances in computational algorithms such as high-order finite differences (Wu et al., 1996), variable grids (Mufti et al., 1996), pseudo-spectral method (Kosloff and Baysal, 1982), optimal checkpointing (Symes, 2007), and one-step extrapolation (Zhang and Zhang, 2009) reduce computer (memory and disk) cost and computing time. All the above improvements allowed RTM to become an attractive choice for imaging complex structures including salt bodies (Yoon et al., 2003; Farmer et al., 2006).

TWO-WAY ACOUSTIC WAVE EXTRAPOLATION

The wavefield extrapolation problem refers to advancement of a wavefield through space or time. Wave extrapolation in time is crucial in seismic modeling, imaging (reverse-time migration), and time-domain full-wavefield inversion. The most popular and straightforward way to implement wave extrapolation in time is the method of explicit finite differences (FD), which is only conditionally stable and suffers from numerical dispersion problems (Wu et al., 1996; Finkelstein and Kastner, 2007). In practice, a second-order FD for temporal derivatives and a high-order FD for spatial derivatives are often employed to reduce dispersion and improve accuracy (Liu and

Sen, 2011). FD coefficients are conventionally determined through a Taylor-series expansion around zero wavenumber (Dablain, 1986; Kindelan et al., 1990). Therefore, traditional FD methods are accurate primarily for long-wavelength components.

More advanced methods have been applied previously to FD schemes in the case of one-way wave extrapolation (downward continuation). Holberg (1987, 1988) designed the derivative operator by matching the spectral response in the wavenumber domain. Soubaras (1996) adopted the Remez exchange algorithm (McClellan and Parks, 1972) to obtain L_∞-norm-optimized coefficients for second-derivative filters. Mousa et al. (2009) designed stable explicit depth extrapolators using projections onto convex sets (POCS). These approaches have advantages over conventional FD methods in their ability to propagate shorter-wavelength seismic waves correctly. Beyond those FD improvements for one-way wave extrapolation, many methods have been developed to improve the accuracy and stability of two-way FD operators. To satisfy the general criterion for optimal accuracy (Geller and Takeuchi, 1995), Geller and Takeuchi (1998) derived an optimally accurate time-domain finite difference method for computing synthetic seismograms for 1-D problems extended later to 2-D and 3-D (Takeuchi and Geller, 2000). Liu and Sen (2009) proposed FD schemes for two-way scalar waves on the basis of time-space dispersion relations and plane-wave theory. Later on, they suggested adaptive variable-length spatial operators in order to decrease computing costs significantly without reducing accuracy (Liu and Sen, 2011). The Liu-Sen scheme satifies the exact dispersion relation and has greater accuracy and better stability than a conventional one. However, it still uses a Taylor expansion around the zero wavenumber.

The following acoustic-wave equation is widely used in seismic modeling and reverse-time migration (Etgen et al., 2009):

$$\frac{\partial^2 p}{\partial t^2} = v(\mathbf{x})^2 \, \nabla^2 p \; , \tag{1.9}$$

where $p(\mathbf{x}, t)$ is the seismic pressure wavefield and $v(\mathbf{x})$ is the propagation velocity. Assuming a constant velocity, v, after Fourier transform in space, we could obtain the following explicit expression,

$$\frac{d^2 \hat{p}}{dt^2} = -v^2 |\mathbf{k}|^2 \hat{p} \; , \tag{1.10}$$

where

$$\hat{p}(\mathbf{k}, t) = \int_{-\infty}^{+\infty} p(\mathbf{x}, t) e^{i\mathbf{k}\cdot\mathbf{x}} d\mathbf{x} \; . \tag{1.11}$$

Equation 1.10 has an explicit solution:

$$\hat{p}(\mathbf{k}, t + \Delta t) = e^{\pm i |\mathbf{k}| v \Delta t} \hat{p}(\mathbf{k}, t) \; . \tag{1.12}$$

A second-order time-marching scheme and the inverse Fourier transform lead to the expression (Etgen, 1989; Soubaras and Zhang, 2008):

$$p(\mathbf{x}, t + \Delta t) \approx \int \hat{p}(\mathbf{k}, t) \, e^{i \, [\mathbf{k}\cdot\mathbf{x} + v \, |\mathbf{k}| \, \Delta t]} \, d\mathbf{k} \; , \tag{1.13}$$

or

$$p(\mathbf{x}, t + \Delta t) + p(\mathbf{x}, t - \Delta t) \; = \; 2 \int_{-\infty}^{+\infty} \hat{p}(\mathbf{k}, t) \cos(|\mathbf{k}| v \Delta t) e^{-i\mathbf{k}\cdot\mathbf{x}} d\mathbf{k} \; . \tag{1.14}$$

Equation (1.14) provides an exact and efficient solution in the case of a constant-velocity medium with the aid of Fast Fourier Transform (FFT). When seismic wave velocity varies in the medium, equation (1.14) turns into a reasonable approximation by replacing v_0 with $v(\mathbf{x})$ (Wards et al., 2008; Fomel et al., 2012). However, FFT

can no longer be applied directly to evaluate the inverse Fourier transform, because a space-wavenumber mixed-domain term appears in the integral operation:

$$W(\mathbf{x}, \mathbf{k}) = \cos(|\mathbf{k}| v(\mathbf{x}) \Delta t). \tag{1.15}$$

As a result, a straightforward numerical implementation of wave extrapolation in a variable velocity medium with mixed-domain matrix 1.15 would increase the cost from $O(N_x \log N_x)$ to $O(N_x^2)$, where N_x is the total size of the three-dimensional space grid. To overcome this problem, Etgen and Brandsberg-Dahl (2009) proposed a velocity interpolation method. They present an implementation for isotropic, VTI (vertical transversely isotropic) and TTI (tilted transversely isotropic) media. In the isotropic case, two FFTs turns out to be sufficient. For anisotropic media, more than one velocity parameter must be used. Therefore, it is necessary to perform velocity interpolation by combining different parameters and computing the corresponding forward and inverse FFTs for each of the velocity parameters, thus increasing the computational burden (Crawley et al., 2010). Other FFT-based solutions include variations of the optimized separable approximation or OSA (Song, 2001; Liu et al., 2009a; Zhang and Zhang, 2009; Du et al., 2010; Fowler et al., 2010b; Fowler and Lapilli, 2012).

Transversely Isotropic Media

Nowadays, a growing number of seismic modeling and imaging techniques are being developed to handle wave propagation in transversely isotropic media (TI). Such anisotropic phenomena are typical in sedimentary rocks, in which the process of lithification usually produces identifiable layering. Tectonic movement of the crust may rotate the rocks and tilt the plane containing the vertical cracks (VTI), causing

a tilted TI (TTI) anisotropy.

Wavefields in anisotropic media are well described by the anisotropic elastic-wave equation. However, in practice, seismologists often have little information about shear waves and prefer to deal with scalar wavefields. Conventional P-wave modeling may contain shear-wave numerical artifacts in the simulated wavefield (Grechka et al., 2004; Duveneck et al., 2008; Zhang et al., 2009). Those artifacts as well as sharp changes in symmetry axis tilting may introduce severe numerical dispersion and instability in modeling. Yoon et al. (2004) proposed to reduce the instability by making the medium elliptically anisotropic in regions with rapid tilt changes. Fletcher et al. (2009) suggested that including a finite shear-wave velocity enhance the stability when solving the coupled equations. These methods can alleviate the instability problem; however, they may also alter the wave propagation kinematics or leave some shear-wave components in the P-wave simulation. A number of spectral methods are proposed to provide solutions which can completely avoid the shear-wave artifacts (Etgen and Brandsberg-Dahl, 2009; Liu et al., 2009b; Chu and Stoffa, 2011; Fomel et al., 2012; Fowler and Lapilli, 2012; Cheng and Kang, 2012; Zhan et al., 2012) at the cost of several Fourier transforms per time step. These methods differ from conventional pseudo-spectral methods (Gazdag, 1981; Fornberg, 2002), because they approximate the space-wavenumber mixed-domain propagation matrix instead of the Laplacian operator.

In the case of transversally isotropic (TTI) media, the term $v(\mathbf{x})\,|\mathbf{k}|$ on the right-hand side of equation 1.15, can be replaced with the acoustic approximation (Alkhalifah, 1998, 2000; Fomel, 2004),

$$f(\mathbf{v},\hat{\mathbf{k}},\eta)=\sqrt{\frac{1}{2}(v_1^2\,\hat{k}_h^2+v_2^2\,\hat{k}_2^2)+\frac{1}{2}\sqrt{(v_1^2\,\hat{k}_h^2+v_2^2\,\hat{k}_2^2)^2-\frac{8\eta}{1+2\eta}v_1^2v_2^2\,\hat{k}_h^2\,\hat{k_2^2}}}\,, \quad (1.16)$$

where v_1 is the P-wave phase velocity in the direction normal to the symmetry axis, v_2 is the P-wave phase velocity along the symmetry axis, η is the anisotropic elastic parameter (Alkhalifah and Tsvankin, 1995) related to Thomsen's elastic parameters ϵ and δ (Thomsen, 1986) by

$$\frac{1+2\delta}{1+2\epsilon}=\frac{1}{1+2\eta}\,;$$

$\hat{k}_h^2=\hat{k}_1^2+\hat{k}_2^2$; and $\hat{k}_1$, $\hat{k}_2$, and $\hat{k}_3$ stand for the wavenumbers evaluated in a rotated coordinate system aligned with the symmetry axis:

$$\begin{aligned}\hat{k}_1&=k_1\cos\phi+k_2\sin\phi\\ \hat{k}_2&=-k_1\sin\phi\cos\theta+k_2\cos\phi\cos\theta+k_3\sin\theta\\ \hat{k}_3&=k_1\sin\phi\sin\theta-k_2\cos\phi\sin\theta+k_3\cos\theta\,,\end{aligned} \quad (1.17)$$

where θ is the tilt angle measured with respect to vertical and ϕ is the angle between the projection of the symmetry axis in the horizontal plane and the original X-coordinate. The symmetry axis has the direction of $\{-\sin\theta\sin\phi,-\sin\theta\cos\phi,\cos\theta\}$.

Orthorhombic Anisotropy

Tectonic stresses may also fracture rocks, inducing another TI with a symmetry axis parallel to the stress direction and usually orthogonal to the sedimentation-based TI. The combination of these effects can be readily represented by an orthorhombic model with three mutually orthogonal planes of mirror symmetry; the P-waves in each symmetry plane can be described kinematically as an independent TI model.

Realization of the importance of orthorhombic models mainly comes from observation of seismic velocity azimuthal variations in flat-layered rocks, which may indicate useful properties of fractured reservoirs (Tsvankin and Grechka, 2011).

Alkhalifah (2003) introduced an acoustic wave equation of the sixth order in axis-aligned orthorhombic media. Fowler and King (2011) presented coupled systems of partial differential equations for pseudo-acoustic wave propagation in orthorhombic media by extending their previous work in TI media (Fowler et al., 2010a). Zhang and Zhang (2011) extended self-adjoint differential operators in TTI media (Duveneck and Bakker, 2011; Zhang et al., 2011) to orthorhombic media.

LOWRANK APPROXIMATION

Fomel et al. (2010, 2012) presented a novel algorithm for wave extrapolation in heterogeneous and anisotropic media. The algorithm is based on a lowrank approximation of the extrapolation symbol. It reduces the cost of extrapolation to that of a small number of FFT operations per time step. The number corresponds to the approximation rank. The algorithm has a high, spectral accuracy. In that sense, it is comparable with a number of other recently proposed FFT-based methods (Etgen and Brandsberg-Dahl, 2009; Chu and Stoffa, 2011; Fomel et al., 2012; Fowler and Lapilli, 2012; Zhan et al., 2012) . Its advantage is a direct control on the accuracy-efficiency trade-off by controlling the rank of the approximation and the corresponding approximation error.

A lowrank approximation implies selecting a small set of representative spatial locations and a small set of representative wavenumbers. The optimized separable approximation or OSA (Song, 2001) was previously employed for wave extrapolation (Zhang and Zhang, 2009; Du et al., 2010) and can be considered as another form of lowrank decomposition. However, the decomposition algorithm in OSA is significantly more expensive, especially for anisotropic wave propagation, because it involves expensive SVD decomposition. The lowrank algorithm can also be regarded as an extension of the wavefield interpolation algorithm of Etgen and Brandsberg-Dahl (2009), with optimally selected reference velocities and weights.

The key idea of the lowrank decomposition (Fomel et al., 2012) is decomposing the wave extrapolation matrix $W(\mathbf{x},\mathbf{k})$ as in equation 1.15 for a fixed Δt into a separated representation

$$W(\mathbf{x},\mathbf{k}) \approx \sum_{m=1}^{M}\sum_{n=1}^{N} W(\mathbf{x},\mathbf{k}_m) a_{mn} W(\mathbf{x}_n,\mathbf{k}). \tag{1.18}$$

Representation (1.18) speeds up the computation of $P(\mathbf{x},t+\Delta t)$ since

$$\begin{aligned} P(\mathbf{x},t+\Delta t) &= \int e^{i\mathbf{x}\mathbf{k}} W(\mathbf{x},\mathbf{k}) \widehat{P}(\mathbf{k},t) d\mathbf{k} \\ &\approx \sum_{m=1}^{M} W(\mathbf{x},\mathbf{k}_m) \left(\sum_{n=1}^{N} a_{mn} \left(\int e^{i\mathbf{x}\mathbf{k}} W(\mathbf{x}_n,\mathbf{k}) \widehat{P}(\mathbf{k},t) d\mathbf{k} \right) \right) \end{aligned} \tag{1.19}$$

The evaluation of the last formula is effectively equivalent to applying N inverse Fast Fourier Transforms. Physically, a separable lowrank approximation amounts to selecting a set of N representative spatial locations and M representative wavenumbers.

The construction of approximation (1.18) can be viewed as a matrix decom-

position problem

$$\mathbf{W} \approx \mathbf{W}_1 \, \mathbf{A} \, \mathbf{W}_2 \tag{1.20}$$

where $\mathbf{W}$ is the $N_x \times N_x$ matrix with entries $W(\mathbf{x}, \mathbf{k})$, $\mathbf{W}_1$ is the submatrix of $\mathbf{W}$ that consists of the columns associated with $\{\mathbf{k}_m\}$, $\mathbf{W}_2$ is the submatrix that consists of the rows associated with $\{\mathbf{x}_n\}$, and $\mathbf{A} = \{a_{mn}\}$.

The matrix $\mathbf{W}$ has a low rank separated representation provided that Δt is sufficiently small. The construction of the separated representation in equation (1.20) follows the method of Engquist and Ying (2007, 2009).

PROBLEM STATEMENT AND OUTLINE

Fourier Finite Differences

Another form of equation (1.14) is

$$\begin{aligned} p(\mathbf{x}, t + \Delta t) + p(\mathbf{x}, t - \Delta t) - 2p(\mathbf{x}, t) = \\ 2 \int_{-\infty}^{+\infty} \hat{p}(\mathbf{k}, t)(\cos(|\mathbf{k}| v \Delta t) - 1) e^{-i\mathbf{k}\cdot\mathbf{x}} d\mathbf{k} \, . \end{aligned} \tag{1.21}$$

a well-known expression for two-way acoustic wave extrapolation (Etgen, 1989; Soubaras and Zhang, 2008). In the case of a variable-velocity medium, equation 1.21 can provide an approximation by replacing v with $v(\mathbf{x})$ (Wards et al., 2008; Fomel et al., 2012). However, FFT can no longer be applied directly for the inverse Fourier transform from the wavenumber domain back to the space domain. To overcome this problem, I propose to incorporate a novel Fourier Finite Difference method into the numerical solution 1.21 of the two-way wave equation. The technique involves

cascading a Fourier Transform operator and a finite difference operator to form a chain operator: Fourier Finite Differences (FFD). I derive the FFD operator from a pseudo-analytical solution of the acoustic wave equation. A chain operator by cascading a Fourier operator and a Finite Difference operator (FFD) will take the place of the conventional Finite Difference operator. It is called the Fourier Finite Difference method (Song and Fomel, 2011) because it is analogous to the FFD concept introduced previously for one-way wave extrapolation by Ristow and Ruhl (1994).

As a chain operator of Fast Fourier Transform and Finite Difference operators, the proposed extrapolator can achieve the accuracy of the parameter interpolation approach employed by Etgen and Brandsberg-Dahl (2009) but at a cost of only one Fast Fourier Transform (FFT) and inverse Fast Fourier Transform (IFFT) operation. Next I extend two-way FFD from the case of constant density to variable density. I construct the FFD operator for coupled first-order wave propagation equations using staggered spatial and temporal grids. The advantages of the FFD operator are even more apparent in the anisotropic case: no need for several interpolations for different parameters with the corresponding computational burden of several FFTs and IFFTs.

Lowrank Finite Differences and Lowrank FFD

I also propose lowrank Fourier FDs (LFFD), by replacing the original FD operator in the two-way FFD with the corresponding lowrank FD (LFD). The scheme is derived from the lowrank approximation of the mixed-domain operator and its representation by FDs with adapted coefficients. Using this approach, we only need to compute the FD coefficients once and save them for the whole process of wave

extrapolation or reverse-time migration. The method is flexible enough to control accuracy by the rank of approximation and by FD order selection. LFFD improves the accuracy of FFD, in particular in tilted transversely isotropic (TTI) media.

The derived LFD scheme can accurately propagate seismic-wave components with a wide range of wavelengths, which has advantages over conventional FDs that focus on small wavelengths. In comparison with the Fourier-domain approach, the method is free of FFTs and can further reduce the cost to $O(L\,N_x)$, where L is the order of the scheme. I also adopt the LFD technique to replace the FD operator based on Taylor's expansion in the FFD method. The generated LFFD operator can reduce dispersion in the TTI case by using an 8th-order LFD operator.

I devote a chapter to each method, including individual introduction, theory, numerical examples and discussion sections. I compare these methods with each other, as well as with conventional FDs. In the following chapter, I adopt a dispersion relation for orthorhombic anisotropic media and introduce a mixed-domain acoustic wave extrapolator for time marching in orthorhombic media. I use the lowrank approximation to overcome the complicated mixed-domain operator. I demonstrate by numerical examples that the method is kinematically accurate. In the last chapter, I include a gallery of several RTM images produced by FFD RTM on synthetic models. I also include an image by TTI FFD RTM on a real 2D line from the western Gulf of Mexico, provided by BP. Finally, I conclude with a summary of the proposed methods and key results, along with a comparison of the three methods.

Chapter 2

Fourier finite-difference wave propagation

In this chapter, I present a novel wave extrapolator motivated initially by the pseudo-analytical approach of Etgen and Brandsberg-Dahl (2009). The method combines FFT and finite differences. It is named the Fourier Finite Difference method because it is analogous to the concept introduced previously for one-way wave extrapolation by Ristow and Ruhl (1994).

As a chain operator of Fast Fourier Transform and Finite Difference operators, the proposed extrapolator can be practically as accurate as the parameter interpolation approach employed by Etgen and Brandsberg-Dahl (2009) but at a cost of only one Fast Fourier Transform (FFT) and inverse Fast Fourier Transform (IFFT) operation.

I also extend the two-way FFD method from constant-density to variable-density media. I derive a version of the FFD operator for coupled first-order wave-propagation equations using staggered spatial and temporal grids. This novel FFD operator may prove useful in seismic wave modeling applications that require high accuracy.

Parts of this chapter were published in Song and Fomel (2011) and Song et al. (2012b).

The advantages of the FFD operator are even more apparent in the anisotropic case: no need for several interpolations for different parameters with the corresponding computational burden of several FFTs and IFFTs. In addition, the operator can overcome the coupling of qP-waves and qSV-waves (Zhang et al., 2009). I demonstrate the method on synthetic examples and propose to incorporate FFD into reverse-time migration in order to enhance migration accuracy and stability.

THEORY

Isotropic FFD

A second-order time-marching scheme and the inverse Fourier transform lead to the well-known expression 1.14. Equation 1.14 provides an elegant and efficient solution in the case of a constant-velocity medium with the aid of FFT. In the case of a variable-velocity medium, equation 1.14 can provide an approximation by replacing v with $v(\mathbf{x})$. However, FFT can no longer be applied directly for the inverse Fourier transform from the wavenumber domain back to the space domain. To overcome this problem, Etgen and Brandsberg-Dahl (2009) propose a velocity interpolation method. They present an implementation for isotropic, VTI (vertical transversely isotropic) and TTI (tilted transversely isotropic) media. In the isotropic case, two FFTs can be sufficient. For anisotropic media, more than one velocity parameter must be used. Therefore, it is necessary to perform velocity interpolation by combining different parameters and computing the corresponding forward and inverse FFTs for each of the velocity parameters, thus increasing the computational burden. Other FFT-based solutions include the optimized separable approximation or OSA (Song, 2001; Liu et al., 2009a; Zhang and Zhang, 2009; Du et al., 2010; Fowler et al., 2010b) and the lowrank approximation (Fomel et al., 2010, 2012).

I propose an alternative approach. First, I adopt the following form of the right-hand side of equation 1.14 in the variable velocity case:

$$\begin{aligned} &2\left[\cos(v(\mathbf{x})|\mathbf{k}|\Delta t)-1\right]= \\ &\qquad 2\left[\cos(v_0|\mathbf{k}|\Delta t)-1\right]\left[\frac{\cos(v(\mathbf{x})|\mathbf{k}|\Delta t)-1}{\cos(v_0|\mathbf{k}|\Delta t)-1}\right] , \end{aligned} \tag{2.1}$$

where v_0 is the reference velocity, such as the RMS (root-mean-square) velocity of the medium. After that, I apply the following approximation:

$$\frac{\cos(v(\mathbf{x})|\mathbf{k}|\Delta t)-1}{\cos(v_0|\mathbf{k}|\Delta t)-1} \approx a + 2\sum_{n=1}^{3} b_n \cos(k_n \Delta x_n) , \tag{2.2}$$

where coefficients a and b_n are defined using the Taylor expansion around $k=0$,

$$\begin{aligned} a &= \frac{v^2(\mathbf{x})}{v_0^2}\left[1+\frac{(\Delta t)^2(v_0^2-v^2(\mathbf{x}))(\Delta x_1^2\Delta x_2^2+\Delta x_2^2\Delta x_3^2+\Delta x_3^2\Delta x_1^2)}{6\Delta x_1^2\Delta x_2^2\Delta x_3^2}\right] \\ b_n &= \frac{(\Delta t)^2 v^2(\mathbf{x})(v^2(\mathbf{x})-v_0^2)}{12(\Delta x_n^2)v_0^2} \end{aligned} , \tag{2.3}$$

and Δx_n is the sampling in the n-th direction. One only needs to calculate these coefficients once. After completing the calculation, they can be used at each time step during the wave extrapolation process.

Equation 2.1 consists of two terms: the first term is independent of $\mathbf{x}$ and only depends on $\mathbf{k}$. For this part, I use inverse FFT to return to the space domain from the wavenumber domain. For the remaining part, however, we can avoid phase shift in the wavenumber domain by implementing space shifts through finite differences with coefficients provided by equation 2.3. This approach is analogous to the FFD method proposed by Ristow and Ruhl (1994) for one-way extrapolation in depth.

Figure 2.1 (a) shows approximations for $[\cos(v(\mathbf{x})|\mathbf{k}|\Delta t) - 1]$ by the 4th-order FD method (dash line) and pseudo-spectral method (dotted line). Figure 2.1 (b) shows approximations by the FFD method (2nd-order: dash line, 4th-order: dotted line). The solid lines stand for the exact values for function $[\cos(v(\mathbf{x})|\mathbf{k}|\Delta t) - 1]$ with true velocity: $v = 4.0km/s$ (bottom solid line) and $v_0 = 2.0km/s$ (top solid line), which indicates a significant velocity contrast (100% difference). In this situation, all the approximations deviate from the exact solution as the wavenumber $|k|$ becomes large. However, the 4th-order FFD method approximates the exact solution with the most accuracy, as shown in the error plot (Figure 2.2). In order to enhance stability, one can suppress the wavefield at high wavenumbers for both pseudo-spectral and the FFD method.

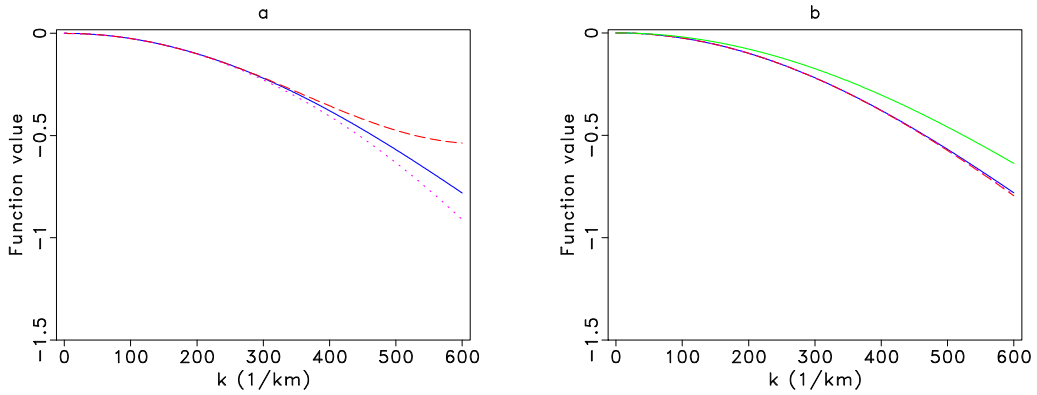

Figure 2.1: Different approximations for $\cos(v(\mathbf{x})|\mathbf{k}|\Delta t) - 1$. Solid lines: exact solution $(\cos(v(\mathbf{x})|\mathbf{k}|\Delta t) - 1)$ for $v = 4.0$ km/s and $v_0 = 2.0$ km/s. (a) Dash line: the 4th-order FD. Dotted line: pseudo-spectral method. (b) Dash line: the 2nd-order FFD method. Dotted line: the 4th-order FFD with v_0 as reference velocity. $\Delta t = 0.001$ s. $\Delta x = 0.005$ km. geophysics2010/cos cosside1

Assuming that $p(\mathbf{x}, t - \Delta t)$ and $p(\mathbf{x}, t)$ are already known, the time-marching algorithm can be specified as follows:

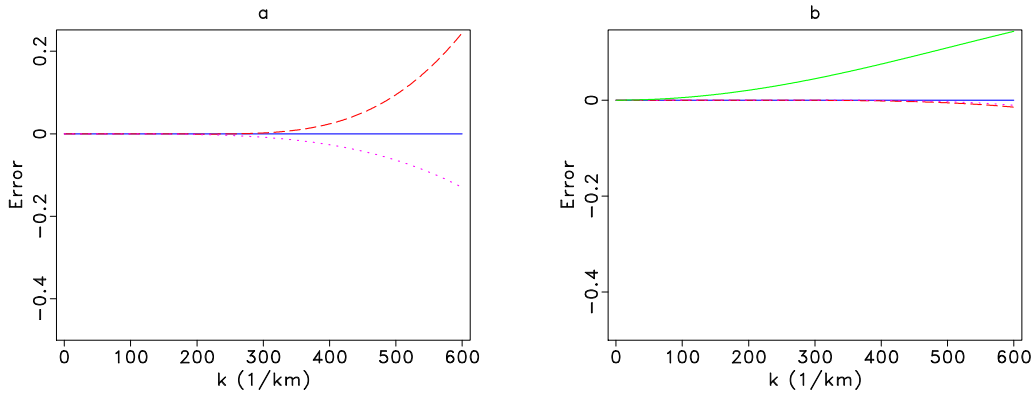

Figure 2.2: Errors for different approximations for $\cos(v(\mathbf{x})|\mathbf{k}|\Delta t) - 1$. Solid lines: exact solution $(\cos(v(\mathbf{x})|\mathbf{k}|\Delta t) - 1)$ for $v = 4.0$ km/s and $v_0 = 2.0$ km/s. (a) Dash line: the 4th-order FD. Dotted line: pseudo-spectral method. (b) Dash line: the 2nd-order FFD method. Dotted line: the 4th-order FFD with v_0 as reference velocity. $\Delta t = 0.001$ s. $\Delta x = 0.005\, km$. geophysics2010/cos diff1

1. Transform $p(\mathbf{x}, t)$ to $\hat{p}(\mathbf{k}, t)$ by 3-D FFT;

2. Multiply $\hat{p}(\mathbf{k}, t)$ by $2\left[\cos(v_0|\mathbf{k}|\Delta t) - 1\right]$ to get $\hat{q}(\mathbf{k}, t)$;

3. Transform $\hat{q}(\mathbf{k}, t)$ to $q(\mathbf{x}, t)$ by inverse FFT;

4. Apply finite differences to $q(\mathbf{x}, t)$ with coefficients in equation 2.3 to get $q(\mathbf{x}, t + \Delta t)$. Namely,

$$\begin{aligned} q^{i,j,k}(t + \Delta t) = & a^{i,j,k} q^{i,j,k}(t) \\ & + b_1^{i,j,k}(q^{i-1,j,k}(t) + q^{i+1,j,k}(t)) \\ & + b_2^{i,j,k}(q^{i,j-1,k}(t) + q^{i,j+1,k}(t)) \\ & + b_3^{i,j,k}(q^{i,j,k-1}(t) + q^{i,j,k+1}(t)) \ , \end{aligned} \tag{2.4}$$

   where i is the grid index of x_i direction;

5. $p(\mathbf{x}, t + \Delta t) \leftarrow q(\mathbf{x}, t + \Delta t) + 2p(\mathbf{x}, t) - p(\mathbf{x}, t - \Delta t)$.

Here $q(\mathbf{x}, t)$ and $\hat{q}(\mathbf{k}, t)$ are temporary functions.

Variable-density FFD

The coupled first-order linear acoustic propagation equations for a medium of variable sound speed and density are

$$\begin{aligned} \rho(\mathbf{r})\frac{\partial \mathbf{u}(\mathbf{r},t)}{\partial t} &= -\nabla p(\mathbf{r},t) \\ \frac{1}{\rho(\mathbf{r})c(\mathbf{r})^2}\frac{\partial p(\mathbf{r},t)}{\partial t} &= -\nabla \cdot \mathbf{u}(\mathbf{r},t), \end{aligned} \tag{2.5}$$

where $\mathbf{u}$ is the vector acoustic particle velocity fluctuation with components u_x and u_z, p is pressure, $\rho(\mathbf{r})$ is density of the medium, $c(\mathbf{r})$ is seismic wave velocity of the medium, and $\mathbf{r}$ represents the vector coordinate (x, z).

In the case of media with homogeneous velocity c_0 and density ρ_0, temporal iteration can be performed exactly using equation 1.14. Equation 1.14 can be rewritten as

$$p(\mathbf{r}, t+\Delta t) - 2p(\mathbf{r},t) + p(\mathbf{r}, t-\Delta t) = -c_0^2 \Delta t^2 \mathbf{F}^{-1}[|\mathbf{k}|^2 \mathrm{sinc}(c_0 \Delta t |\mathbf{k}|/2)^2 \mathbf{F}[p(\mathbf{r},t)]], \tag{2.6}$$

where $\mathrm{sinc}(x) = \sin(x)/x$ and $\mathbf{F}$ denotes a spatial Fourier transform.

The operation on the right-hand side of equation 2.6 is a second-order k-space operator, which is defined as

$$[\nabla^{(c_0 \Delta t)} p(\mathbf{r},t) = -\mathbf{F}^{-1}[|\mathbf{k}|^2 \mathrm{sinc}(c_0 \Delta t |\mathbf{k}|/2)^2 \mathbf{F}[p(\mathbf{r},t)]]. \tag{2.7}$$

Tabei et al. (2002) provided an effective factorization for operator 2.7. They factored the second-order k-space operator into first-order parts associated with each spatial direction:

$$\begin{aligned}
\frac{\partial p(\mathbf{r},t)}{\partial^{(c_0\Delta t)^+}x} &= \mathbf{F}^{-1}[ik_x e^{ik_x\Delta_x/2}\mathrm{sinc}(c_0\Delta t|\mathbf{k}|/2)\mathbf{F}[p(\mathbf{r},t)]],\\
\frac{\partial p(\mathbf{r},t)}{\partial^{(c_0\Delta t)^+}z} &= \mathbf{F}^{-1}[ik_z e^{ik_z\Delta_z/2}\mathrm{sinc}(c_0\Delta t|\mathbf{k}|/2)\mathbf{F}[p(\mathbf{r},t)]],\\
\frac{\partial p(\mathbf{r},t)}{\partial^{(c_0\Delta t)^-}x} &= \mathbf{F}^{-1}[ik_x e^{-ik_x\Delta_x/2}\mathrm{sinc}(c_0\Delta t|\mathbf{k}|/2)\mathbf{F}[p(\mathbf{r},t)]],\\
\frac{\partial p(\mathbf{r},t)}{\partial^{(c_0\Delta t)^-}z} &= \mathbf{F}^{-1}[ik_z e^{-ik_z\Delta_z/2}\mathrm{sinc}(c_0\Delta t|\mathbf{k}|/2)\mathbf{F}[p(\mathbf{r},t)]].
\end{aligned} \tag{2.8}$$

In general, velocity and density vary in space. In this case, I switch to first-order coupled equations 2.5. However, the first-order operators defined in equation 2.8 turn into space-wavenumber, mixed-domain operators after c_0 is replaced with $c(\mathbf{r})$, which means that FFTs can no longer be applied.

In order to overcome the mixed-domain problem, I propose applying the FFD approach. I use operator $\frac{\partial p(\mathbf{r},t)}{\partial^{(c(\mathbf{r})\Delta t)^+}x}$ in equation 2.9 in the two-dimensional case as an example to explain the FFD approach:

$$\frac{\partial p(\mathbf{r},t)}{\partial^{(c(\mathbf{r})\Delta t)^+}x} = \mathbf{F}^{-1}[ik_x e^{ik_x\Delta_x/2}\mathrm{sinc}(c(\mathbf{r})\Delta t|\mathbf{k}|/2)\mathbf{F}[p(\mathbf{r},t)]]. \tag{2.9}$$

The right-hand side of equation 2.9 can be transformed into the following

expression:

$$\begin{aligned}&\mathbf{F}^{-1}[ik_x e^{ik_x\Delta_x/2}\mathrm{sinc}(c(\mathbf{r})\Delta t|\mathbf{k}|/2)\mathbf{F}[p(\mathbf{r},t)]]\\ =\ &\mathbf{F}^{-1}[\frac{\mathrm{sinc}(c(\mathbf{r})\Delta t|\mathbf{k}|/2)}{\mathrm{sinc}(c_0\Delta t|\mathbf{k}|/2)}ik_x e^{ik_x\Delta_x/2}\mathrm{sinc}(c_0\Delta t|\mathbf{k}|/2)\mathbf{F}[p(\mathbf{r},t)]],\end{aligned} \tag{2.10}$$

where c_0 is the reference velocity, such as the RMS (root-mean-square) velocity of the medium.

Next I apply the following approximation to the mixed-domain term:

$$\frac{\mathrm{sinc}(c(\mathbf{r})\Delta t|\mathbf{k}|/2)}{\mathrm{sinc}(c_0\Delta t|\mathbf{k}|/2)} \approx a + 2b_1\cos(k_x\Delta x) + 2b_2\cos(k_z\Delta z)\ , \tag{2.11}$$

where a, b_1, and b_2 are coefficients derived from a Taylor series expansion around $k = 0$ to both sides of equation 2.11:

$$\begin{aligned}b_1 &= \frac{\Delta t^2}{24\Delta x^2}(c(\mathbf{r})^2 - c_0^2),\\ b_2 &= \frac{\Delta t^2}{24\Delta z^2}(c(\mathbf{r})^2 - c_0^2),\\ a &= 1 - 2b_1 - 2b_2.\end{aligned} \tag{2.12}$$

The coefficients shown in equation 2.12 achieve a second-order accuracy in wavenumber. These coefficients need to be calculated only once and saved at the beginning of wave extrapolation. After the calculation is complete, the coefficients for the finite-difference stencil can be used at each time step during the wave-extrapolation process.

Equation 2.10 consists of two parts: the first term is free of space variables ($\mathbf{r}$) and depends only on $\mathbf{k}$. For this part, I use an inverse FFT to return to the space

domain from the wavenumber domain. For the remaining part, however, according to properties of the FFT, we are able to avoid phase shift in the wavenumber domain by implementing space shifts through finite differences (approximation 2.11), with coefficients provided by equation 2.12.

If $p(\mathbf{r},t)$ is already known, its first-order derivative (related to the $+x$ direction) $\frac{\partial p(\mathbf{r},t)}{\partial^{(c(\mathbf{r})\Delta t)^+}x}$ can be calculated as follows:

1. Transform $p(\mathbf{r},t)$ to $\hat{p}(\mathbf{k},t)$ by 2-D FFT,
2. Multiply $\hat{p}(\mathbf{k},t)$ by $ik_x e^{ik_x\Delta_x/2}\text{sinc}(c_0\Delta t|\mathbf{k}|/2)$ to get $\hat{q}(\mathbf{k},t)$,
3. Transform $\hat{q}(\mathbf{k},t)$ to $q(\mathbf{r},t)$ by inverse FFT,
4. Apply finite differences to $q(\mathbf{r},t)$ with coefficients in equation 2.12 to get the derivative $\frac{\partial p(\mathbf{r},t)}{\partial^{(c(\mathbf{r})\Delta t)^+}x}$.

The same approach can be applied to the remaining three operators in equation 2.8. Note that the FD coefficients are the same for those operators and the only difference exists at the second step, resulting from different phase-shift operators.

With the above-defined operators, I am able to extend the two-way FFD algorithm to first-order coupled equations for acoustic-wave extrapolation in variable-density media with staggered spatial and temporal schemes:

$$\frac{u_x(\mathbf{r}_1,t^+)-u_x(\mathbf{r}_1,t^-)}{\Delta t}=-\frac{1}{\rho(\mathbf{r}_1)}\frac{\partial p(\mathbf{r},t)}{\partial^{(c(\mathbf{r})\Delta t)^+}x},$$

$$\frac{u_z(\mathbf{r}_2,t^+)-u_z(\mathbf{r}_2,t^-)}{\Delta t}=-\frac{1}{\rho(\mathbf{r}_2)}\frac{\partial p(\mathbf{r},t)}{\partial^{(c(\mathbf{r})\Delta t)^+}z}, \tag{2.13}$$

$$\frac{p(\mathbf{r},t+\Delta t)-p(\mathbf{r},t)}{\Delta t}=-\rho(\mathbf{r})c(\mathbf{r})^2\left(\frac{\partial u_x(\mathbf{r}_1,t^+)}{\partial^{(c(\mathbf{r})\Delta t)^-}x}+\frac{\partial u_z(\mathbf{r}_2,t^+)}{\partial^{(c(\mathbf{r})\Delta t)^-}z}\right),$$

where

$\mathbf{r}_1=(x+\Delta x/2,z)$, $\mathbf{r}_2=(x,z+\Delta z/2)$, $t^+=t+\Delta t/2$, and $t^-=t-\Delta t/2$.

TTI FFD

The FFD approach is not limited to the isotropic case. In the case of transversally isotropic (TTI) media, the term $v(\mathbf{x})\,|\mathbf{k}|$ on the left-hand side of equation 2.2, can be replaced with the acoustic approximation 1.16.

Using these definitions, I develop a finite-difference approximation analogous to equation 2.2 for FFD in TTI media. For the 2D TTI case, the corresponding FFD algorithm can be described as follows:

1. Transform $p(\mathbf{x},t)$ to $\hat{p}(\mathbf{k},t)$ by FFT;
2. Multiply $\hat{p}(\mathbf{k},t)$ by $\dfrac{2[\cos(f(\mathbf{v_0},\hat{\mathbf{k}},\eta_0)\Delta t)-1]}{|\hat{\mathbf{k}}|^2}$ to get $\hat{q}(\mathbf{k},t)$;
3. Transform $\hat{q}(\mathbf{k},t)$ to $q(\mathbf{x},t)$ by inverse FFT;
4. Apply finite differences to $q(\mathbf{x},t)$ with coefficients in Table 2.1 to get $q(\mathbf{x},t+\Delta t)$.

Namely,

$$
\begin{aligned}
q^{i,j,t+\Delta t} = a^{i,j} q^{i,j,t} & \\
+b_1^{i,j}(q^{i-1,j,t} + q^{i+1,j,t}) & \\
+b_2^{i,j}(q^{i,j-1,t} + q^{i,j+1,t}) & \\
+d_1^{i,j}(q^{i-2,j,t} + q^{i+2,j,t}) & \\
+d_2^{i,j}(q^{i,j-2,t} + q^{i,j+2,t}) & \\
+c^{i,j}(q^{i-1,j-1,t} + q^{i-1,j+1,t} + q^{i+1,j-1,t} + q^{i+1,j+1,t}) \ . &
\end{aligned}
\tag{2.14}
$$

where i is the grid index of x_i direction;

5. $p(\mathbf{x}, t + \Delta t) \leftarrow q(\mathbf{x}, t + \Delta t) + 2p(\mathbf{x}, t) - p(\mathbf{x}, t - \Delta t)$.

Here, $q(\mathbf{x}, t)$ and $\hat{q}(\mathbf{k}, t)$ are temporary functions.

To develop a 25-point finite-difference scheme analogous to equation 2.2 for FFD in 3D TTI media, I first apply the following approximation:

$$
\begin{aligned}
\frac{\cos(f(\mathbf{v}, \hat{\mathbf{k}}, \eta)\Delta t) - 1}{\cos(f(\mathbf{v_0}, \hat{\mathbf{k_0}}, \eta_0)\Delta t) - 1} |\hat{\mathbf{k}}|^2 \approx & \\
a + 2\sum_{n=1}^{3} \left(b_n \cos(k_n \Delta x_n) + d_n \cos(2k_n \Delta x_n)\right) & \\
+2\sum_{n=1}^{3} c_n [\cos(k_i \Delta x_i + k_j \Delta x_j) + \cos(k_i \Delta x_i - k_j \Delta x_j)] \ , &
\end{aligned}
\tag{2.15}
$$

where $i, j = 1, 2, 3$; $i \neq j$; $i, j \neq n$.

In approximation 2.15, $f(\mathbf{v}, \hat{\mathbf{k}}, \eta)$ is a function as in expression 1.16 and a, b_n, c_n and d_n are coefficients determined from the Taylor expansion around $k = 0$. Notice that when multiplying the left-hand side by $|\hat{\mathbf{k}}|^2$, one needs to multiply $\hat{p}(\hat{\mathbf{k}}, \mathbf{t})$ with

$$\frac{2[\cos(f(\mathbf{v_0},\mathbf{k},\eta_0)\Delta t)-1]}{|\hat{\mathbf{k}}|^2}.$$

The coefficients for Equation 2.15 are derived in Table 2.1 and Table 2.2. w_{n0}, h_{n0}, p_{n0} and q_{n0} have similar expressions as above in Table 2.2 with $\mathbf{v}$, η and θ substited by the corresponding reference values: RMS velocity $\mathbf{v}_0$, average anisotropic parameter η_0 and average tilt angles θ_0 and ϕ_0.

a	$a=-2b_1-2b_2-2b_3-4c_1-4c_2-4c_3-2d_1-2d_2-2d_3$
b	$b_1=-2c_2-2c_3-4d_1-\dfrac{w_1+h_1}{\Delta x_1^2(w_{10}+h_{10})}$
c	$b_2=-2c_1-2c_3-4d_2-\dfrac{w_2+h_2}{\Delta x_2^2(w_{20}+h_{20})}$
d	$b_3=-2c_1-2c_2-4d_3-\dfrac{w_3+h_3}{\Delta x_3^2(w_{30}+h_{30})}$
e	$d_1=\dfrac{(w_1+h_1)(2x_1^2+\Delta t^2(w_{10}+h_{10}-w_1-h_1))}{24\Delta x_1^4(w_{10}+h_{10})}$
f	$d_2=\dfrac{(w_2+h_2)(2x_2^2+\Delta t^2(w_{20}+h_{20}-w_2-h_2))}{24\Delta x_2^4(w_{20}+h_{20})}$
g	$d_3=\dfrac{(w_3+h_3)(2x_3^2+\Delta t^2(w_{30}+h_{30}-w_3-h_3))}{24\Delta x_3^4(w_{30}+h_{30})}$
h	$c_1=\dfrac{1}{12\Delta x_2^2\Delta x_3^2}\left[\dfrac{\Delta x_2^2(w_2+h_2)}{w_{20}+h_{20}}+\dfrac{\Delta x_3^2(w_3+h_3)}{w_{30}+h_{30}}\right]-d_2\dfrac{\Delta x_2^2}{\Delta x_3^2}-d_3\dfrac{\Delta x_3^2}{\Delta x_2^2}$ $+\dfrac{\Delta t^2(p_1+q_1)(p_10+q_10-p1-q1)}{12\Delta x_2^2\Delta x_3^2(p_10+q_10)}$
i	$c_2=\dfrac{1}{12\Delta x_1^2\Delta x_3^2}\left[\dfrac{\Delta x_1^2(w_1+h_1)}{w_{10}+h_{10}}+\dfrac{\Delta x_3^2(w_3+h_3)}{w_{30}+h_{30}}\right]-d_1\dfrac{\Delta x_1^2}{\Delta x_3^2}-d_3\dfrac{\Delta x_3^2}{\Delta x_1^2}$ $+\dfrac{\Delta t^2(p_2+q_2)(p_20+q_20-p2-q2)}{12\Delta x_1^2\Delta x_3^2(p_20+q_20)}$
j	$c_3=\dfrac{1}{12\Delta x_1^2\Delta x_2^2}\left[\dfrac{\Delta x_1^2(w_1+h_1)}{w_{10}+h_{10}}+\dfrac{\Delta x_2^2(w_2+h_2)}{w_{20}+h_{20}}\right]-d_1\dfrac{\Delta x_1^2}{\Delta x_2^2}-d_2\dfrac{\Delta x_2^2}{\Delta x_1^2}$ $+\dfrac{\Delta t^2(p_3+q_3)(p_30+q_30-p3-q3)}{12\Delta x_1^2\Delta x_2^2(p_30+q_30)}$

Table 2.1: Coefficients for equation 2.15.

a	$w_1 = v_1^2 \cos^2\phi + \sin^2\phi(v_1^2\cos^2\theta + v_2^2\sin^2\theta)$
b	$w_2 = (v_1^2 + v_2^2)\cos^2\phi\cos^2\theta + v_1^2\sin^2\theta$
c	$w_3 = v_1^2\sin^2\theta + v_2^2\cos^2\theta$
d	$h_1 = \sqrt{w1^2 - \dfrac{8\eta v_1^2 v_2^2 \sin^2\phi(\cos^2\phi + \sin^2\phi\cos^2\theta)\sin^2\theta}{1+2\eta}}$
e	$h_2 = \sqrt{w2^2 - \dfrac{8\eta v_1^2 v_2^2 \cos^2\phi\cos^2\theta(\cos^2\phi\cos^2\theta + \sin^2\phi)}{1+2\eta}}$
f	$h_3 = \sqrt{w3^2 - \dfrac{8\eta v_1^2 v_2^2 \cos^2\theta\sin^2\theta}{1+2\eta}}$
g	$p_1 = w_2 + w_3 + v_1^2\cos\phi\sin 2\theta - 2v_2^2\cos\phi\cos^2\theta$
h	$q_1 = \sqrt{p_1^2 - \dfrac{32\eta v_1^2 v_2^2 \cos^2\theta\sin^4\frac{\phi}{2}(\cos^2\phi\cos^2\theta + \sin^2\theta + \sin^2\phi + \cos\phi\sin 2\theta)}{1+2\eta}}$
i	$p_2 = w_1 + w_3 + (v_2^2 - v_1^2)\sin\phi\sin 2\theta$
j	$q_2 = \sqrt{p_2^2 - \dfrac{8\eta v_1^2 v_2^2(\cos\theta + \sin\phi\sin\theta)^2(\cos^2\phi + (\cos\theta\sin\phi - \sin\theta)^2)}{1+2\eta}}$
k	$p_3 = w_1 + w_2 + v_1^2\sin^2\theta\sin 2\phi + \frac{1}{2}v_2^2\sin 2\phi\sin 2\theta$
l	$q_3 = \sqrt{p_3^2 - \dfrac{4\eta v_1^2 v_2^2\cos^2(\phi+\theta)(\sin 2\phi\cos 2\theta - 3 - \cos 2\theta - \sin 2\phi)}{1+2\eta}}$

Table 2.2: Coefficients for Table 2.1.

Stability Analysis

The time stepping size of the proposed FFD algorithm is restricted by the required stability conditions. I analyze the stability conditions in this section.

Let us assume equation 1.9 has a plane wave solution with the following form

$$P \;=\; e^{i(\omega t - \mathbf{k}\cdot\mathbf{x})} \;, \tag{2.16}$$

where ω is the angular frequency, $\omega = |\mathbf{k}|v(\mathbf{x})$.

With the above assumption, we can derive

$$P^{n+1} + P^{n-1} - 2P^n \;=\; 2P^n \left[\cos(|\mathbf{k}|v(\mathbf{x})\Delta t) - 1\right] \;, \tag{2.17}$$

Equation 2.17 is accurate for arbitrarily large time step. By applying equation 2.2, FFD provides an approximation to equation 2.17

$$P^{n+1} + P^{n-1} - 2P^n \;=\; 2P^n \left[\cos(|\mathbf{k}|v_0\Delta t) - 1\right] \left[a + 2\sum_{j=1}^{3} b_j \cos(k_j \Delta x_j)\right] \;, \tag{2.18}$$

The coefficients a and b_j have the following relation

$$a + 2\sum_{j=1}^{3} b_j = \frac{v^2(\mathbf{x})}{v_0^2} \;. \tag{2.19}$$

As a result, equation 2.18 can be transformed to

$$P^{n+1} + P^{n-1} - 2P^n \;=\; 2P^n \left[\cos(|\mathbf{k}|v_0\Delta t) - 1\right] f(v_0) \;, \tag{2.20}$$

where

$$f(v_0) = \frac{v^2(\mathbf{x})}{v_0^2} + 2\sum_{j=1}^{3} b_j \left[\cos(k_j \Delta x_j) - 1\right] \;. \tag{2.21}$$

The stability of FFD method requires that $[\cos(|\mathbf{k}|v_0\Delta t) - 1]\, f(v_0)$ must be bounded within $[-2, 0]$. That is

$$-2 \;\leq\; [\cos(|\mathbf{k}|v_0\Delta t) - 1]\, f(v_0) \;\leq\; 0\;. \tag{2.22}$$

Next I will discuss the stability condition under two situations: $v_0 > v(\mathbf{x})$ and $v_0 < v(\mathbf{x})$. In the case of $v_0 > v(\mathbf{x})$, one can find $b_j \;<\; 0, j = 1, 2, 3$.
As a result,

$$\begin{aligned} 0 \;\leq\; f(v_0) \;&\leq \frac{v^2(\mathbf{x})}{v_0^2} - 4b_1 - 4b_2 - 4b_3 \\ &= \frac{v^2(\mathbf{x})}{v_0^2}\left[1 + \frac{(\Delta t)^2(\Delta v)^2}{(\Delta x)^2}\right]\;, \end{aligned} \tag{2.23}$$

where

$$(\Delta v)^2 \;= v_0^2 - v^2(\mathbf{x})\;, \tag{2.24}$$

and

$$(\Delta x)^2 \;= \frac{3}{\frac{1}{(\Delta x_1)^2} + \frac{1}{(\Delta x_2)^2} + \frac{1}{(\Delta x_3)^2}}\;. \tag{2.25}$$

In order to satisfy condition 2.22, let

$$\frac{v^2(\mathbf{x})}{v_0^2}\left[1 + \frac{(\Delta t)^2(\Delta v)^2}{(\Delta x)^2}\right] \;\leq\; 1\;. \tag{2.26}$$

The stability condition for $v_0 \;>\; v(\mathbf{x})$ is,

$$\Delta t \;\leq\; \frac{\Delta x}{v_0}\;. \tag{2.27}$$

In the other case, when $v_0 < v(\mathbf{x})$ and $b_j > 0, j = 1, 2, 3$, one can observe that

$$0 < f(v_0) \leq \frac{v^2(\mathbf{x})}{v_0^2}. \tag{2.28}$$

The stability of FFD requires

$$-2 \leq [\cos(|\mathbf{k}|v_0\Delta t) - 1] \frac{v^2(\mathbf{x})}{v_0^2} \leq 0. \tag{2.29}$$

After solving the above expression,

$$|\mathbf{k}|v_0\Delta t \leq \arccos\left[1 - \frac{2v_0^2}{v^2(\mathbf{x})}\right] = 2\arcsin\left[\frac{v_0}{v(\mathbf{x})}\right]. \tag{2.30}$$

Considering the sampling theorem,

$$\begin{aligned} |k_j| &\leq \frac{\pi}{\Delta x_j}, j = 1, 2, 3, \\ |\mathbf{k}| &\leq \frac{\sqrt{3}\pi}{\Delta x}, \end{aligned} \tag{2.31}$$

the stability condition corresponding to $v_0 < v(\mathbf{x})$ is

$$\Delta t \leq \frac{2\arcsin(\frac{v_0}{v(\mathbf{x})})}{\sqrt{3}\pi} \frac{\Delta x}{v_0}. \tag{2.32}$$

For heterogeneous media, one may select some average velocity as the reference velocity v_0 for the purpose of accuracy. So in summary, the stability condition for FFD method in heterogeneous media is

$$\Delta t \leq a_f \frac{\Delta x}{v_{\max}}, \tag{2.33}$$

where a_f is a factor,

$$a_f = \frac{2\arcsin(\frac{v_0}{v(\mathbf{x})})}{\sqrt{3}\pi} \frac{v_{\max}}{v_0}. \tag{2.34}$$

Table 2.3 displays values of 3D FFD stability condition number a_f with different ratios between v_0 and $v_{\max}$. Comparing the derived stability condition with that of 3D pseudo-spectral method which is shown as

$$\Delta t \leq \frac{2}{\sqrt{3}\pi} \frac{\Delta x}{v_{\max}} \approx 0.368 \frac{\Delta x}{v_{\max}};, \tag{2.35}$$

one can find that the FFD method allows larger time-stepping sizes than that of pseudo-spectral method.

$\frac{v_0}{v_{\max}}$	0.2	0.3	0.4	0.5	0.6	0.7	0.8	0.9	1.0
a_f	0.370	0.373	0.378	0.385	0.394	0.407	0.426	0.457	1.0

Table 2.3: Stability condition number a_f for 3D FFD method.

I also give the stability condition in the 2D case. According to the sampling theorem,

$$|\mathbf{k}| \leq \frac{\sqrt{2}\pi}{\Delta x'} , \tag{2.36}$$

where

$$(\Delta x')^2 = \frac{2}{\frac{1}{(\Delta x_1)^2} + \frac{1}{(\Delta x_2)^2}} . \tag{2.37}$$

The stability condition for 2D FFD method in heterogeneous media is

$$\Delta t \leq a_f \frac{\Delta x}{v_{\max}} , \tag{2.38}$$

where

$$a_f = \frac{\sqrt{2}\arcsin(\frac{v_0}{v(\mathbf{x})})}{\pi} \frac{v_{\max}}{v_0} . \tag{2.39}$$

Table 2.4 displays values of 2D FFD stability condition number a_f with different ratios between v_0 and $v_{\max}$.

In practice, the reference v_0 may be selected as about 0.7 of the maximum velocity, so $a_f \approx 0.4$ in 3-D case and $a_f \approx 0.5$ in 2-D, which is similar to that of the

$\frac{v_0}{v_{\max}}$	0.2	0.3	0.4	0.5	0.6	0.7	0.8	0.9	1.0
a_f	0.453	0.457	0.463	0.472	0.483	0.498	0.521	0.560	1.0

Table 2.4: Stability condition number a_f for 2D FFD method.

FD methods.

Although I derive the stability condition in the isotropic constant-density case, the above condition appears to remain valid in the variable density and TTI cases according to numerical experiments.

NUMERICAL EXAMPLES

My first example is a comparison of four methods: 4th-order finite differences, pseudo-spectral method, velocity interpolation, and the FFD method in a velocity model with smooth variation, formulated as

$$v(x,z) \;=\; 550 + 1.5 \times 10^{-4}(x-800)^2 + 10^{-4}(z-500)^2;$$

$$0 \le x \le 2560,\; 0 \le z \le 2560.$$

The velocity is between 550 m/s and 1439 m/s. A Ricker-wavelet source with maximum frequency 70 Hz is located at the center of the model. For all the numerical simulations based on this model, I use the same grid size: $\Delta x \;=\; 5$ m and $\Delta t \;=\; 2$ ms.

Figure 2.3(a) shows that a snapshot of the acoustic wavefield computed by the 4th-order finite difference method contains an obvious numerical dispersion. Figure 2.3(b) shows a slight dispersion from the snapshot computed by pseudo-spectral

method (Reshef et al., 1988). Figure 2.3(c) shows the corresponding snapshot of the velocity-interpolation method (Etgen and Brandsberg-Dahl, 2009; Crawley et al., 2010), calculated using two reference velocities. It is practically free of dispersion thanks to spectral compensation. Figure 2.3(d) shows a snapshot of the proposed FFD method. It is almost exactly the same as Figure 2.3(c); however, only one reference velocity is used instead of two. As comparison between Figure 2.3(d) and Figure 2.3(c) implies, the FFD method has practically the same accuracy as the velocity interpolation method while having only one reference velocity and therefore replacing the cost of one additional FFT with the cost of a low-order finite-difference operator.

The next example is a snapshot of the acoustic wavefield calculated by FFD in the BP model (Billette and Brandsberg-Dahl, 2004). I use a Ricker-wavelet at a point source. The maximum frequency is 50 Hz. The horizontal grid size Δx is 37.5 m, the vertical grid size Δz is 12.5 m and the time step is 1 ms. Figure 2.4 shows a part of the model with a salt body. Figure 2.5 shows a wavefield snapshot confirming that the FFD method can work in a complex-velocity medium as well.

Next, I test a simple 2D four-layer model (grids: 400×400, $\Delta x = \Delta z = 10$ m). Figure 2.6(a) and 2.6(b) display corresponding velocity (1500-5000 m/s) and density (1000-2500 kg/m^3) parameters. A Ricker-wavelet source with a center frequency of 20 Hz is located in the center of the model at a depth of 10 m in the first layer of the model. The time step is 1 ms. Figure 2.7 displays two horizontal slices at a depth of 800 m selected from simulated wavefield snapshots at 1.5 s. The top trace was calculated using the fourth-order FD method. Note that it displays apparent

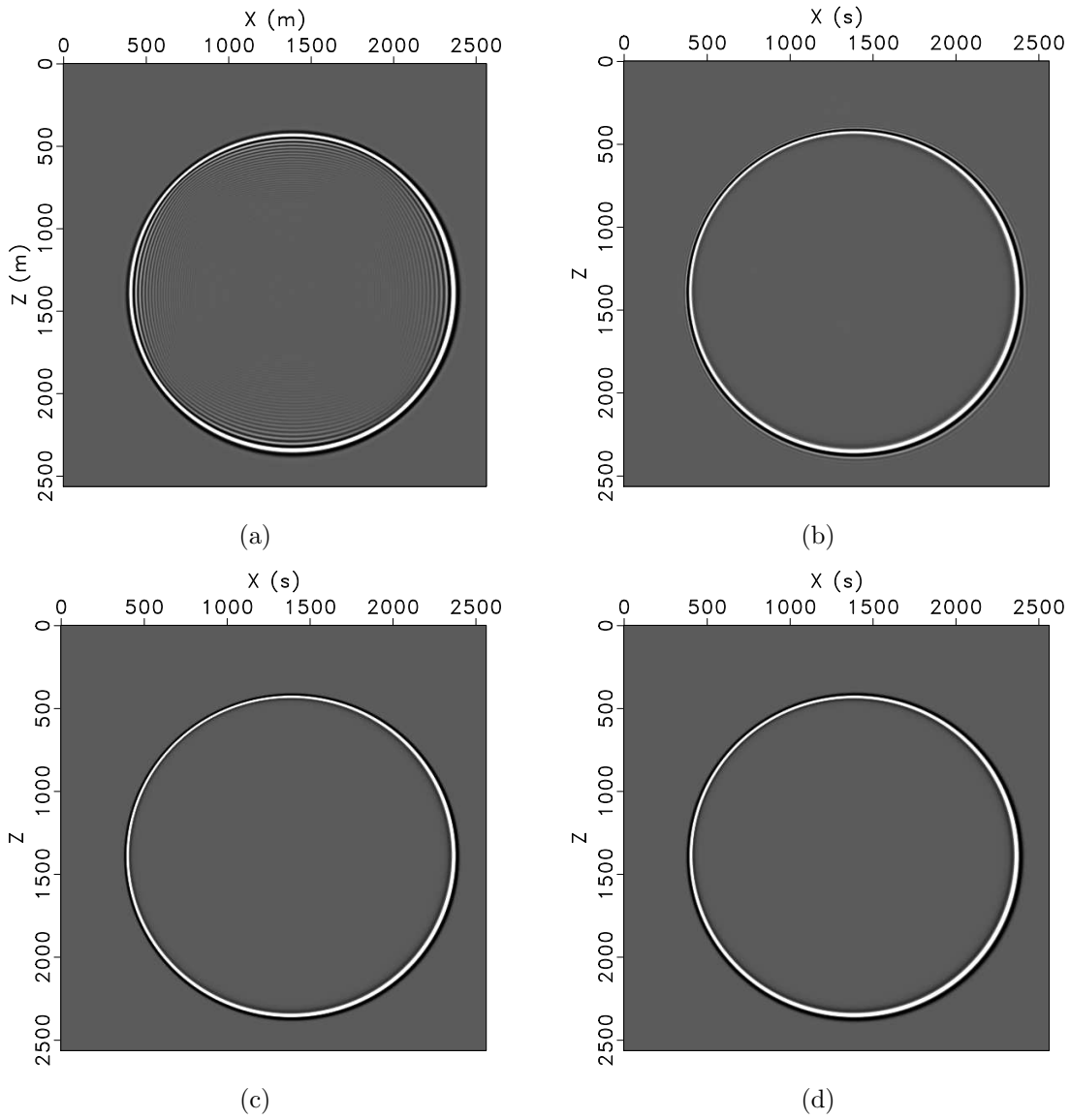

Figure 2.3: Acoustic wavefield snapshot by: (a) 4th-order Finite Difference method; (b) pseudo-spectral method; (c) velocity interpolation method with 2 reference velocities; (d) FFD method with RMS velocity. geophysics2010/ffd wavfd,wavsp,wavpspi,wavffd

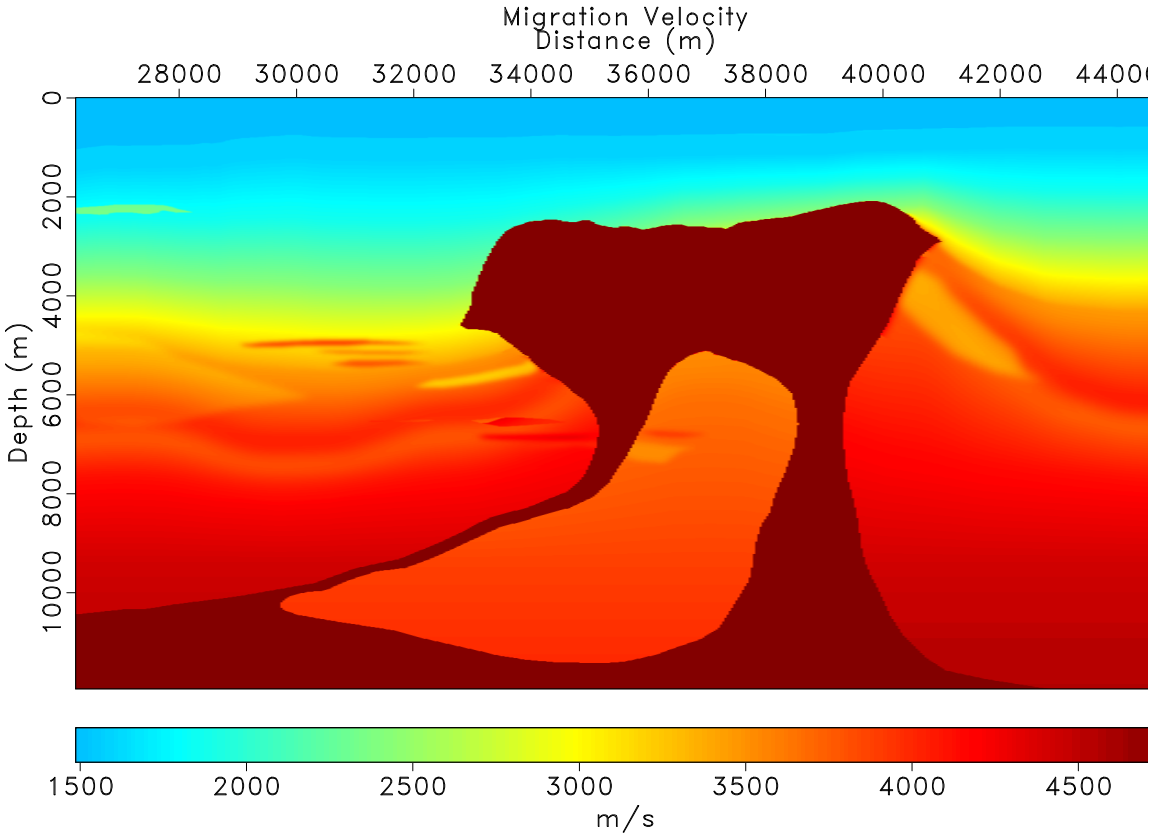

Figure 2.4: Portion of BP 2004 synthetic velocity model. geophysics2010/bpmodel velp

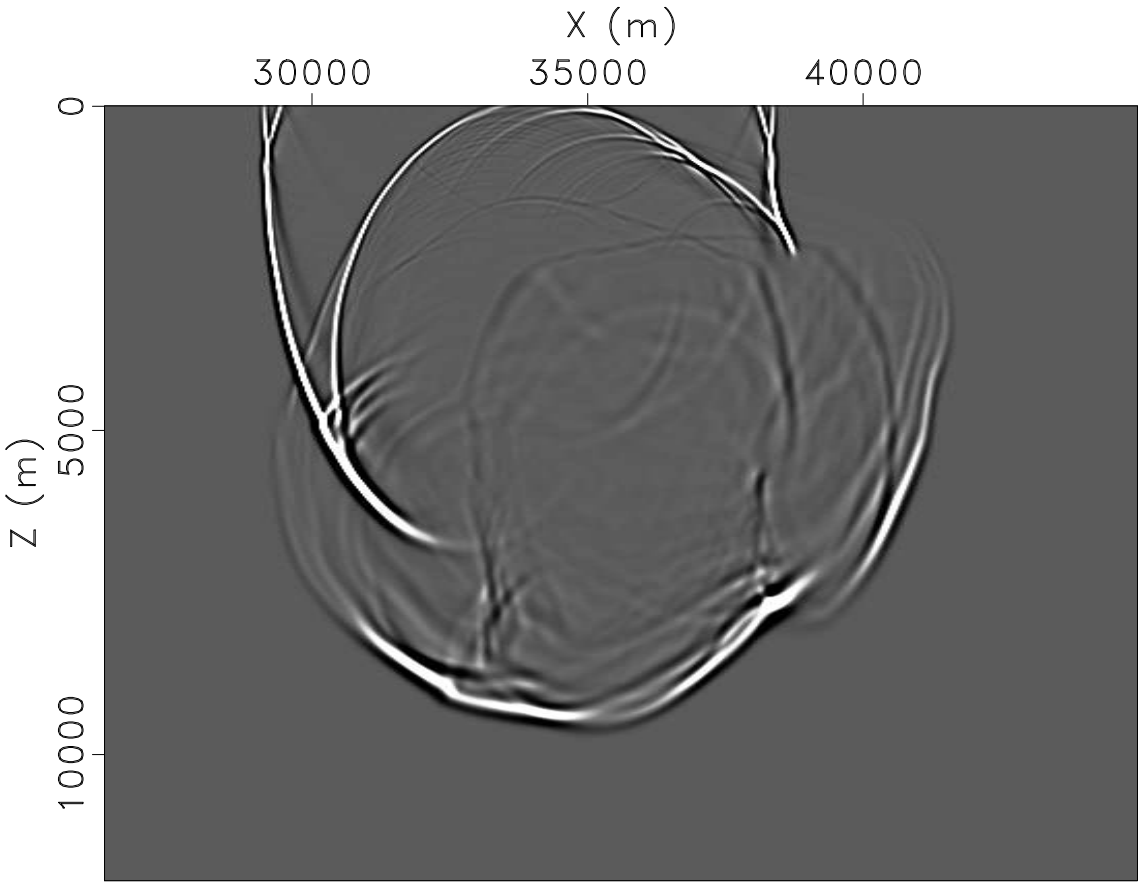

Figure 2.5: Wavefield snapshot in the BP Model shown in Figure 2.4. geophysics2010/bpmodel wavsnap

dispersions. And the bottom one is from the FFD method, which is free of dispersions. Figure 2.8 shows the corresponding wavefield snapshot calculated using the FFD method at 1.5 s. Note that the FFD method provides a dispersion-free wavefield.

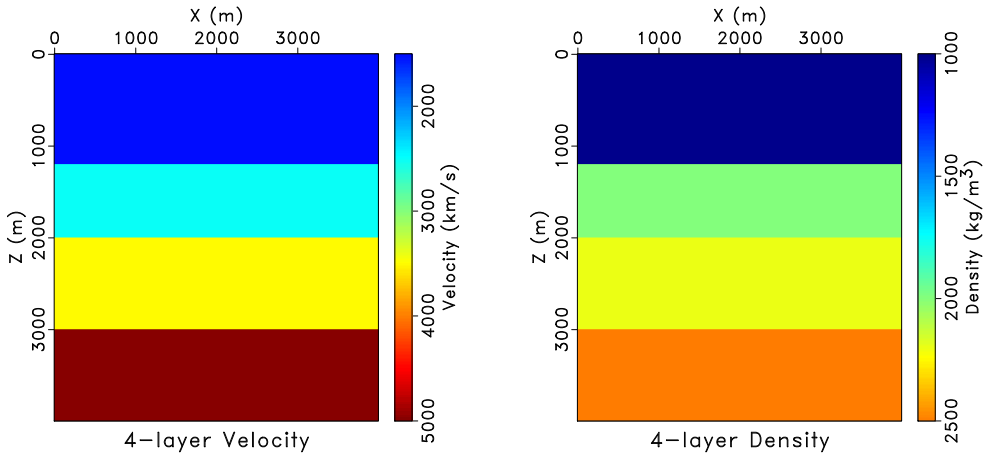

(a) (b)

Figure 2.6: 4-layer model: (a) Velocity:1500-5000 m/s, (b) Density: 1000-2500 kg/m^3. geophysics2010/fourlayer vel4l,den4l

My next example is a snapshot of the acoustic wavefield calculated by the proposed FFD method in the BP model (Billette and Brandsberg-Dahl, 2004). I use a Ricker-wavelet at a point source. The center frequency is 15 Hz. Both the horizontal grid size Δx and the vertical grid size Δz are 12.5 m, and the time step is 1 ms. Figures 2.9 and 2.10 show the velocity and density of a part of the model containing a salt body. Figure 2.11 shows a wavefield snapshot confirming that the FFD method can work in a complicated velocity and density medium as well. The snapshot is clean and free of dispersions. Figure 2.12 displays a shotgather generated by the FFD method. The source is located at a depth of 12.5 m. Note that the FFD method provides clear reflections.

The cost advantage of FFD is more appealing in anisotropic (TTI) media,

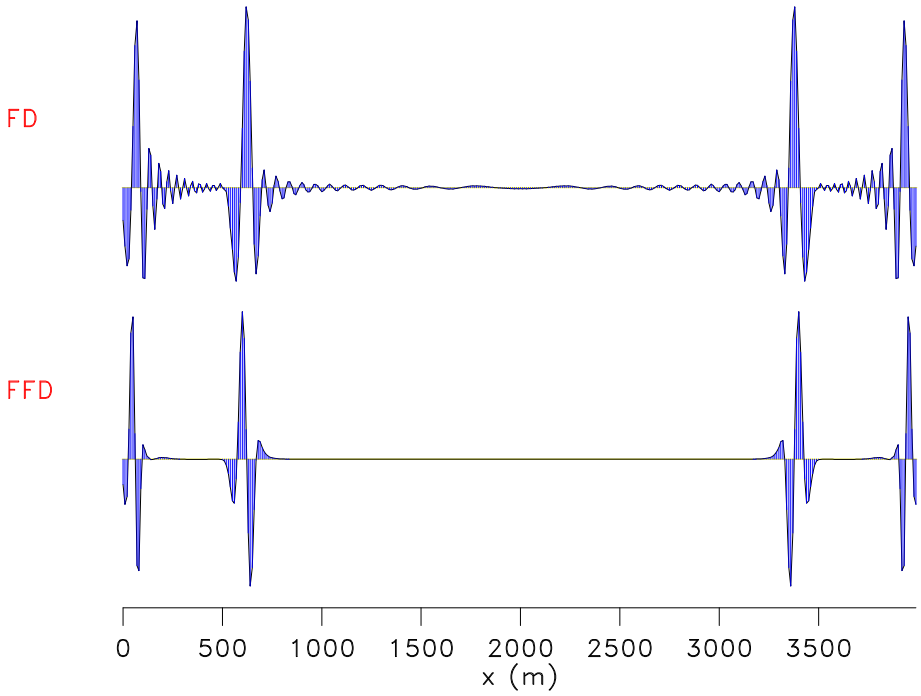

Figure 2.7: Horizontal slices at the depth of 800 m selected from the snapshots at 1.5 s for the comparision between the FFD method (bottom) and the fourth-order FD (top). geophysics2010/fourlayer trace

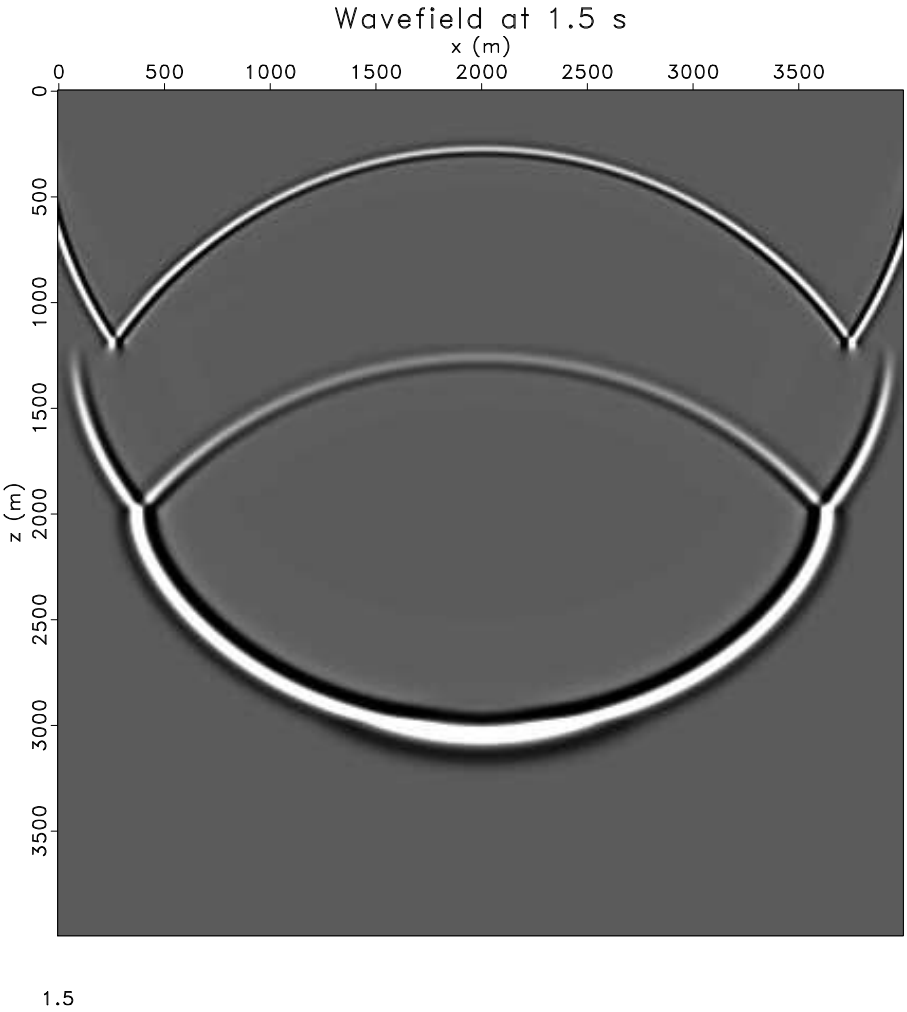

Figure 2.8: Wavefield snapshot by the FFD method at 1.5 s. geophysics2010/fourlayer ffdtime15

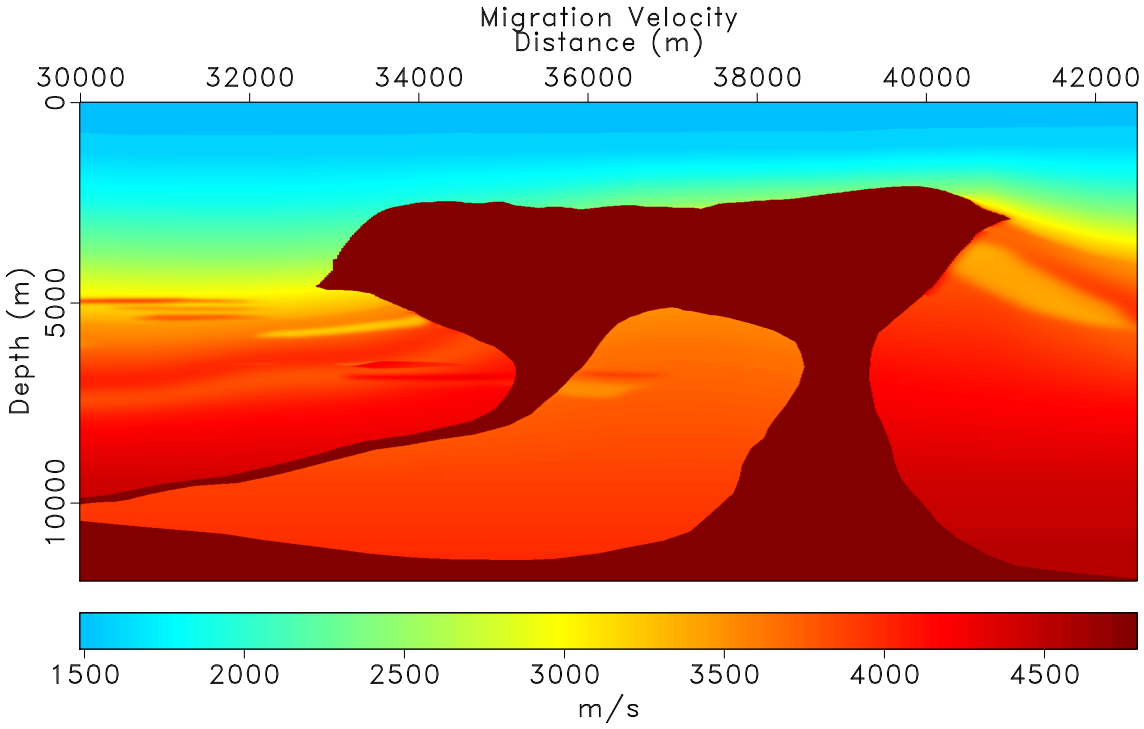

Figure 2.9: Portion of BP 2004 synthetic velocity model. geophysics2010/bpden vel

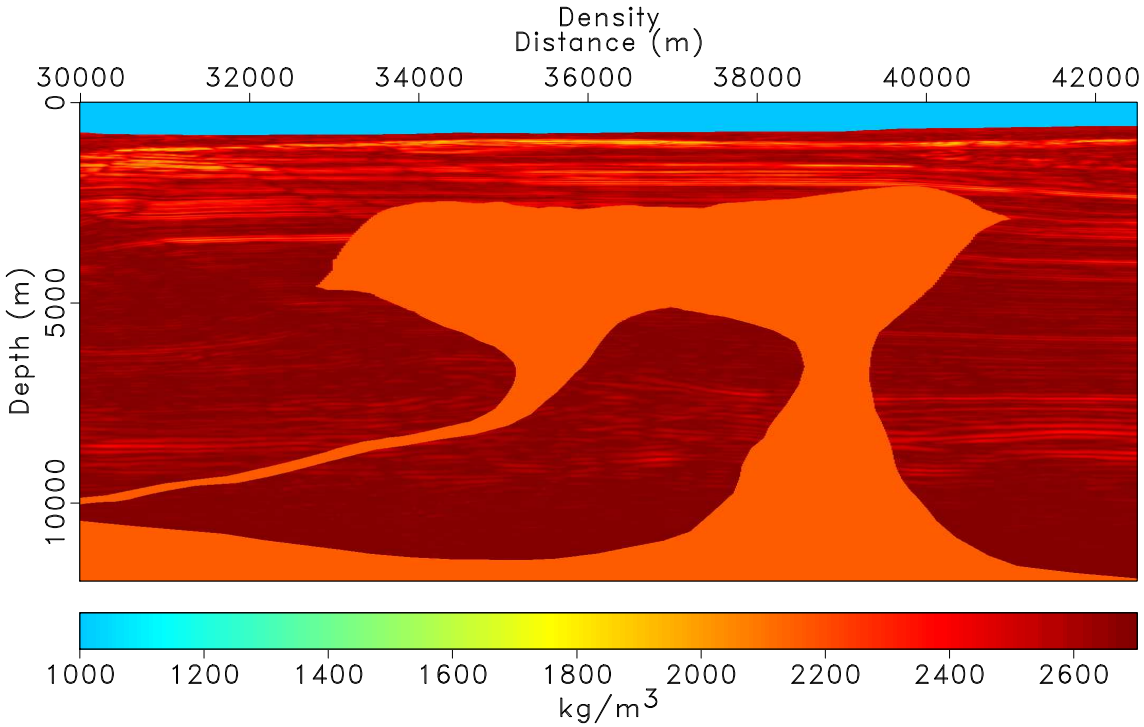

Figure 2.10: Portion of BP 2004 synthetic density model. geophysics2010/bpden den

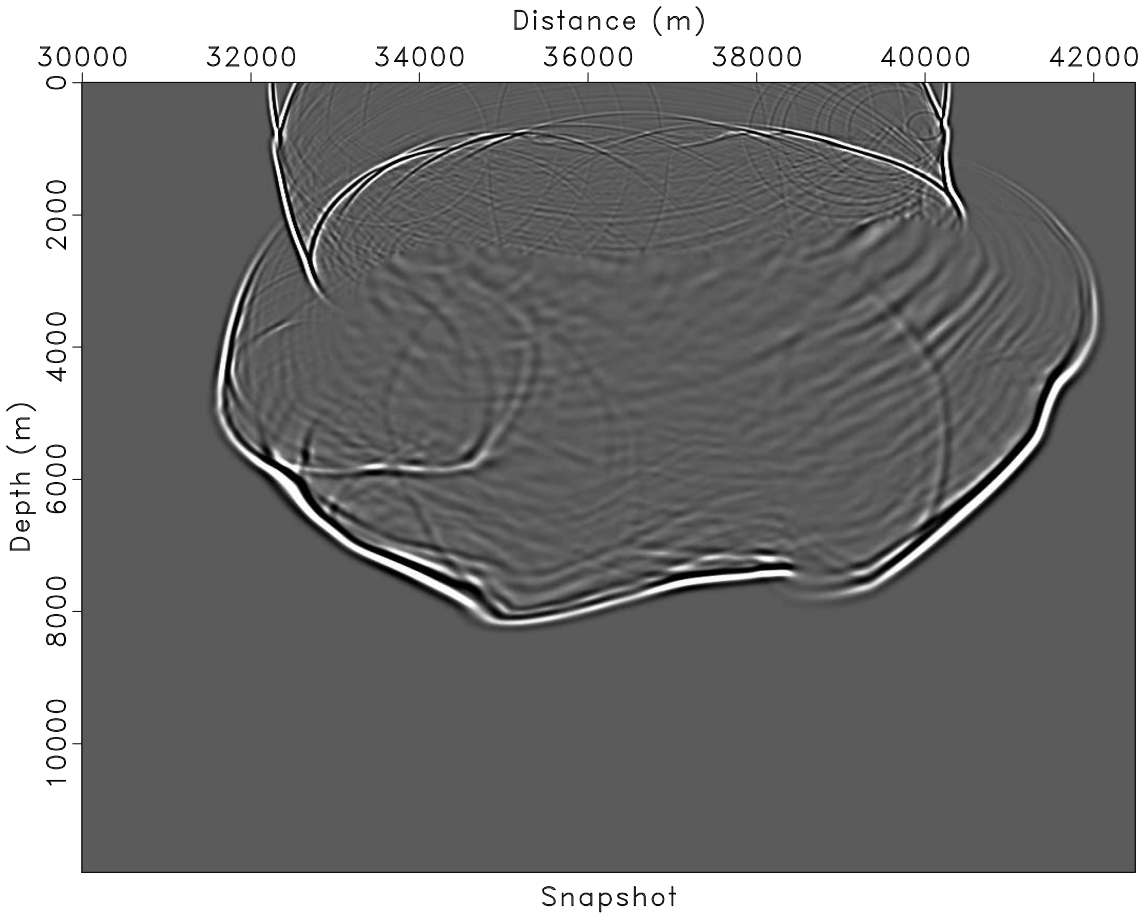

Figure 2.11: Wavefield snapshot in the BP Model shown in Figure 2.9 and 2.10. geophysics2010/bpden snap500

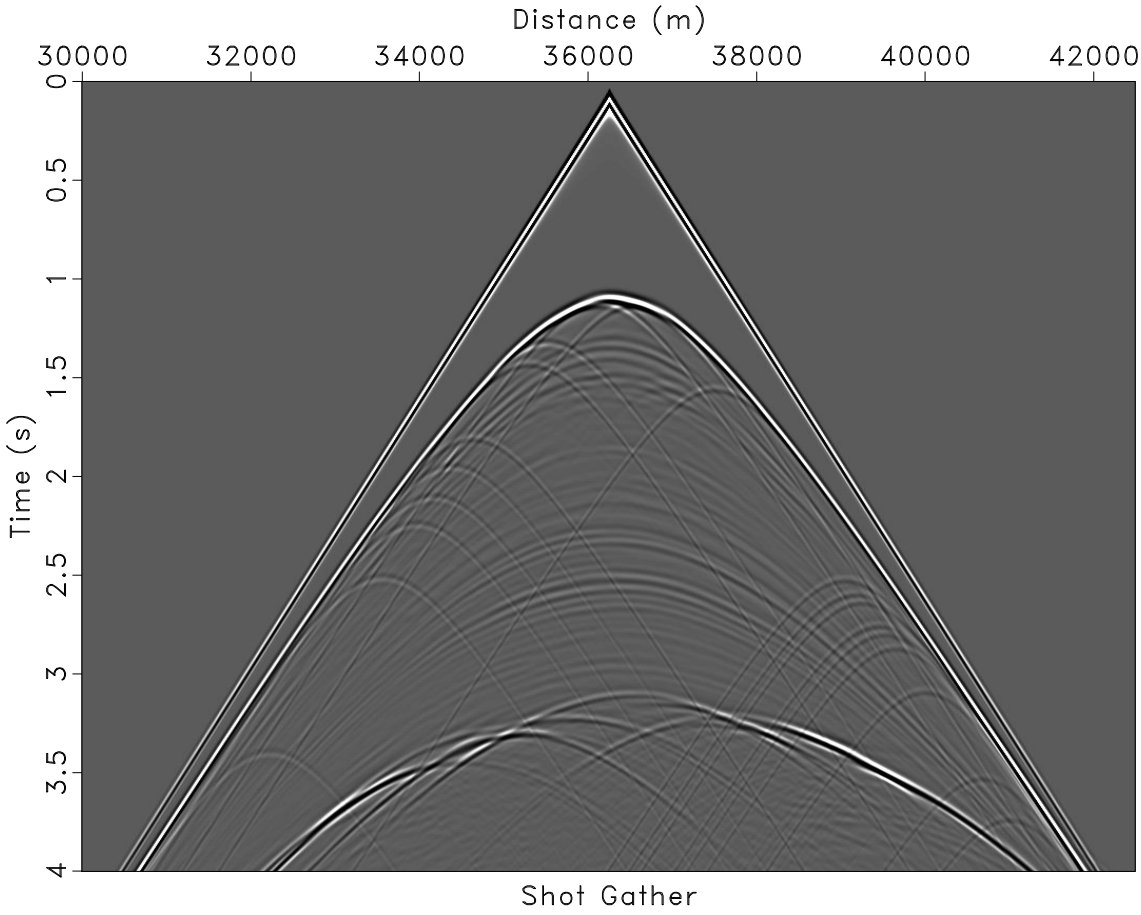

Figure 2.12: One shot gather generated by the FFD method in the BP Model shown in Figure 2.9 and 2.10. geophysics2010/bpden wave500

which require multiple velocity parameters and increase the cost of velocity interpolation. Figure 2.13 shows the impulse response of a 4th-order FFD operator in a TTI model with the tilt of 45 $^\circ$ and a smooth velocity variation (v_x: 800-1225.41 m/s, v_z: 700-883.6 m/s). The space grid size is 5 m and the time step is 1 ms. The maximum frequency is 35 Hz. Note the absence of coupling of qP-waves and qSV-waves (Zhang et al., 2009), thanks to the Fourier construction of the operator.

I implemented a 2nd-order 5-point FD scheme for 2D isotropic case. One can observe little dispersion in isotropic examples. For TTI media, I use a 13-point scheme which minimizes the error along the symmetry axis and in the direction normal to the symmetry axis. In order to suppress the dispersion, TTI FFD requires denser sampling (around 4 points) per wavelength, which indicates that a more accurate FD scheme might be required to further improve the method.

My last example is qP-wave simulation in the BP 2D TTI model (Shah, 2007). Figure 2.14(a)-2.14(d) shows parameters for part of the model. The maximum frequency is 50 Hz. The space grid size is 6.25 m and the time step is 1 ms. The snapshot of the acoustic wavefield in Figure 2.15 demonstrates the stability of the approach in a complicated anisotropic model. The sampling rate is around 4.7 points per wavelength, pointing to a possible need to extend the FD part of the FFD scheme from second order to higher orders. This possibility is investigated in the next chapter.

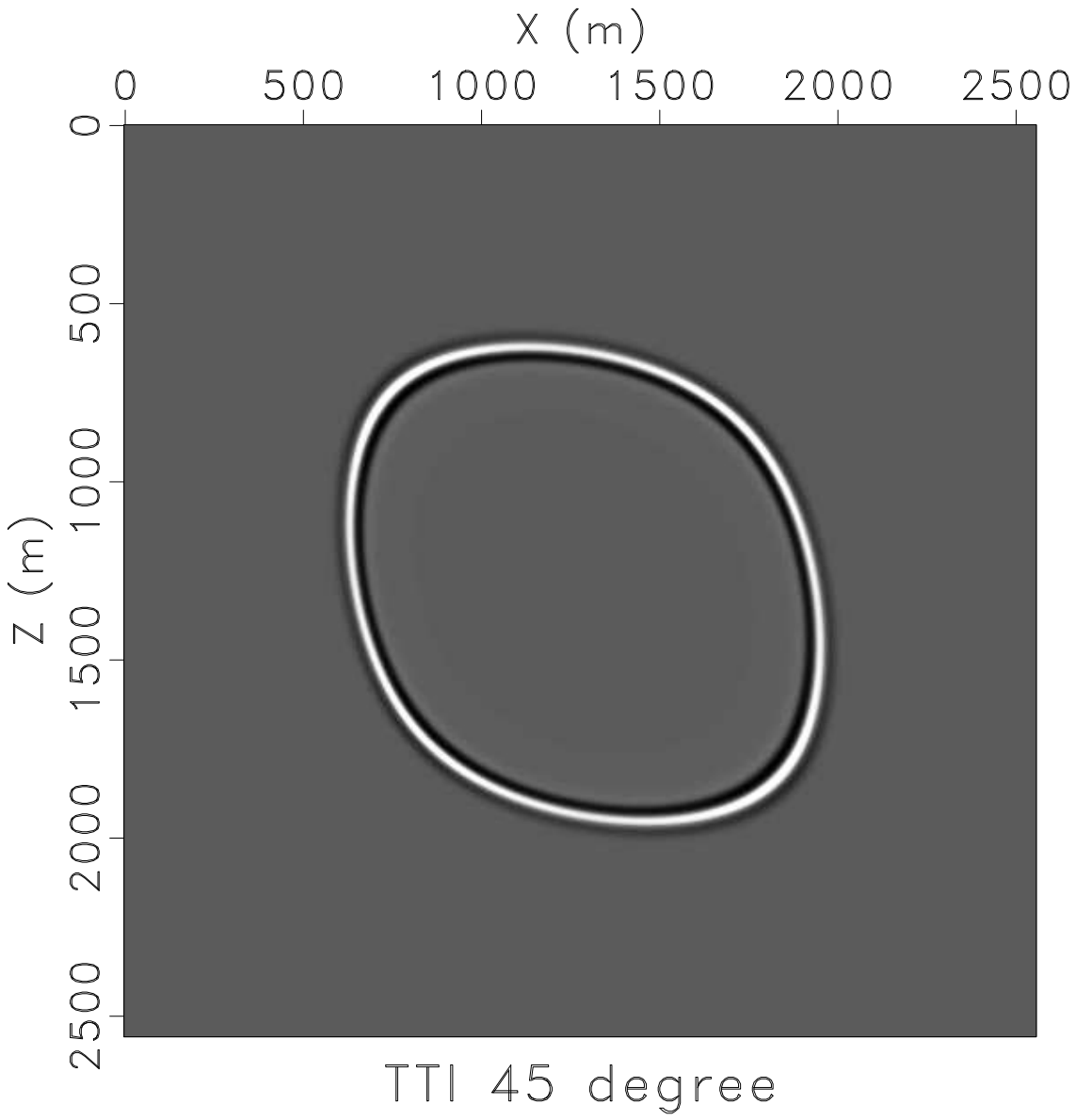

Figure 2.13: Wavefield snapshot in a TTI medium with tilt of 45 degrees. $v_x(x,z) = 800 + 10^{-4}(x-1000)^2 + 10^{-4}(z-1200)^2$; $v_z(x,z) = 700 + 10^{-4}(z-1200)^2$; $\eta = 0.3$; $\theta = 45^\circ$. geophysics2010/anisotropic TTI-snapshotl

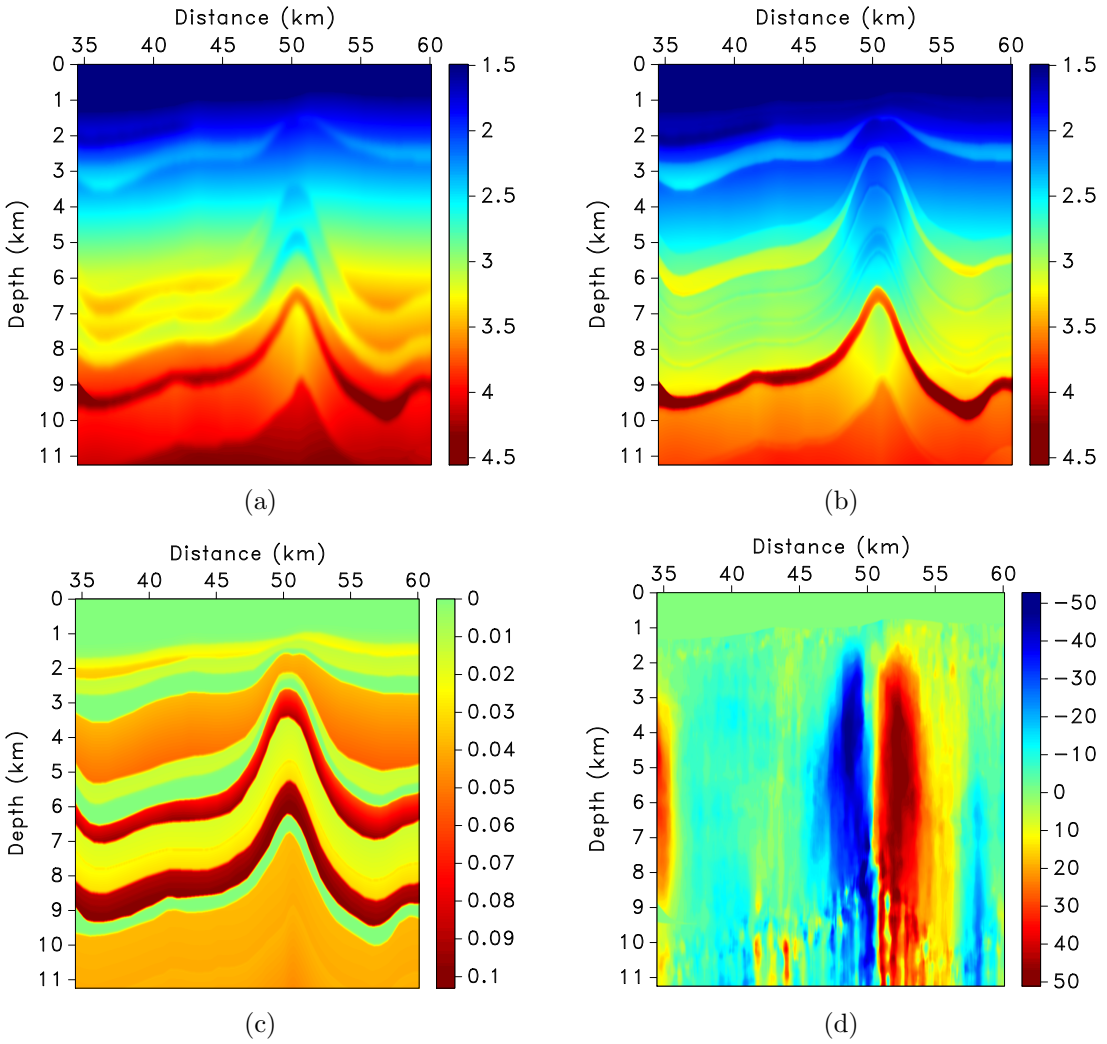

Figure 2.14: Partial region of the 2D BP TTI model. a: v_z. b: v_x. c: η. d:θ. geophysics2010/bptti vp2,vx2,yita2,theta2

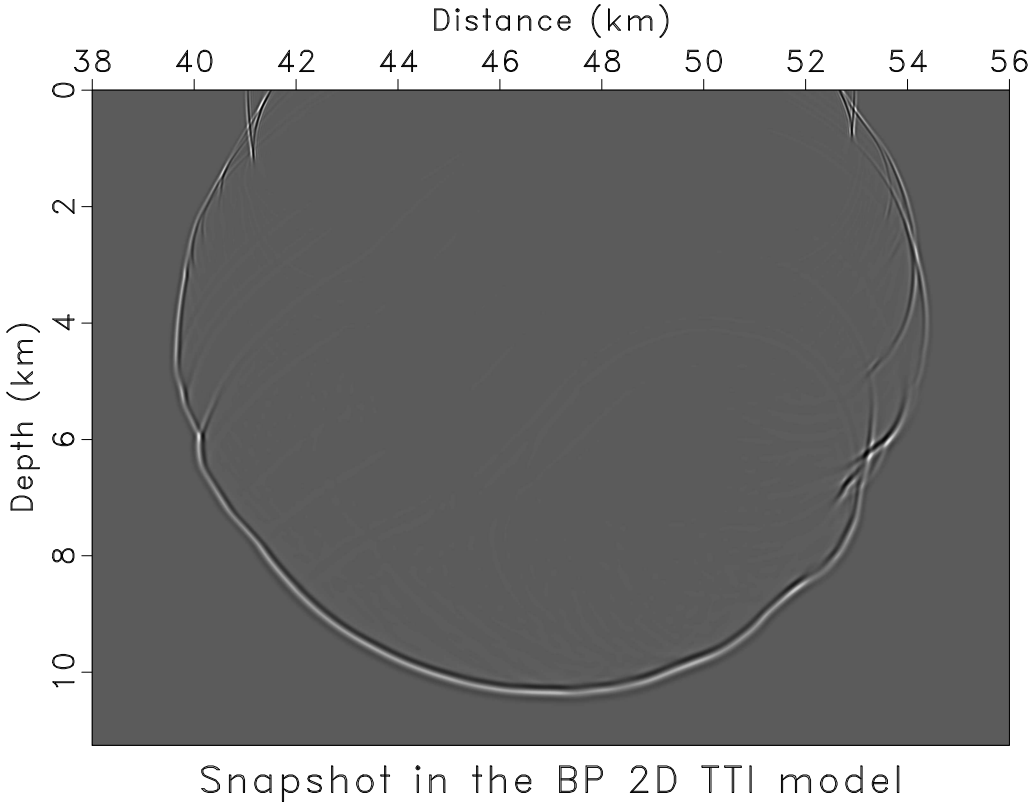

Figure 2.15: Scalar wavefield snapshot in the 2D BP TTI model, shown in Figure 2.14.
geophysics2010/bptti ttie

CONCLUSIONS

Accurate and efficient numerical wave propagation in variable velocity media is crucial for seismic modeling and seismic imaging, particularly for reverse-time migration. Several alternative algorithms have been developed for seismic wave extrapolation in variable velocity media. In recent years, thanks to advances in supercomputer technology, spectral methods have become feasible for large-scale problems and are attracting more and more attention.

The FFD technique proposed in this dissertation promises higher accuracy than that of the conventional, explicit finite-difference method, and comparable with that of more expensive spectral methods at the cost of only one forward and inverse Fast Fourier Transform.

I have extended the two-way FFD method from constant-density to variable-density media. I have derived a version of the FFD operator for coupled first-order wave-propagation equations using staggered spatial and temporal grids.

The advantages of the FFD operator are even more apparent in the anisotropic case: no need for several interpolations for different parameters with the corresponding computational burden of several FFTs and IFFTs.

Results in synthetic isotropic and anisotropic models illustrate FFD's stability in complicated velocity models. The novel FFD operators may prove useful in appli-

cations that require high accuracy. In chapter 5, I provide several RTM examples to demonstrate applications of the FFD method to RTM.

Chapter 3

Lowrank finite-differences and lowrank Fourier finite-differences for seismic wave extrapolation in the acoustic approximation

The goal of this chapter is to introduce a FD scheme that is designed to match the spectral response in the mixed space-wavenumber domain for a wide range of spatial wavenumbers. The scheme is derived from the lowrank approximation of the mixed-domain operator (Fomel et al., 2010, 2012), represented by FD with adapted coefficients. I derive this kind of FD schemes for both isotropic and TTI media. Using this approach, one only needs to compute the FD coefficients once and save them for the whole process of wave extrapolation or reverse-time migration.

The method is flexible enough to control accuracy by two parameters: the rank ofthe approximation and the FD order selection. In the previous chapter, I have presented the two-way FFD method for seismic wave extrapolation in variable velocity media. In this chapter, I propose lowrank Fourier FDs (LFFD), by replacing the original FD operator in the two-way Fourier FDs (FFD) with the corresponding lowrank FD (LFD). LFFD improves the accuracy of FFD, in particular in tilted transversely isotropic (TTI) media. I propose incorporating wave extrapolation with LFD and LFFD into seismic imaging by reverse-time migration.

Parts of this chapter appear in Song et al. (2011) and Song et al. (2012a).

Lowrank Finite Differences

In a matrix notation, the lowrank decomposition problem takes the form of equation 1.20:

$$\mathbf{W} \approx \mathbf{W}_1 \cdot \mathbf{A} \cdot \mathbf{W}_2, \tag{3.1}$$

where $\mathbf{W}$ is a space-wavenumber mixed-domain $N_x \times N_x$ matrix with entries $W(\mathbf{x}, \mathbf{k}) = \cos(\phi(\mathbf{x}, \mathbf{k}), \Delta t)$, which appears in wavefield extrapolation. $\mathbf{W}_1$ is the submatrix of $\mathbf{W}$ that consists of the columns associated with $\{\mathbf{k}_m\}$, $\mathbf{W}_2$ is the submatrix that consists of the rows associated with $\{\mathbf{x}_n\}$, and $\mathbf{A} = \{a_{mn}\}$.

As a kind of spectral method, the lowrank approxmation is highly accurate. However, its cost is several FFTs per time step. The goal of this chapter is to reduce the cost further by deriving an FD scheme that matches the spectral response of the output from the lowrank decomposition.

Note that $\mathbf{W}_2$ is a matrix related only to wavenumber $\mathbf{k}$. I propose to further decompose it as follows:

$$\mathbf{W_2} \approx \mathbf{C} \cdot \mathbf{B}, \tag{3.2}$$

where we determine $\mathbf{B}$ to be an $L \times N_x$ matrix, and the entry, $\mathbf{B}(\xi, \mathbf{k})$, has the form of $\cos(\sum_{j=1}^{3} \xi^j k_j \Delta x_j)$, in which ξ is a 3-D integer vector, $\xi = (\xi^1, \xi^2, \xi^3)$, k_j is the jth component of wavenumber $\mathbf{k}$, Δx_j is the space grid size in the jth direction, $j = 1, 2, 3$, and $\mathbf{C}$ is the matrix product of $\mathbf{W}_2$ and the pseudo-inverse of $\mathbf{B}$.

Now we have a new decompostion for the mixed-domain matrix:

$$\mathbf{W} \approx \mathbf{G} \cdot \mathbf{B}, \tag{3.3}$$

where $\mathbf{G}$ is an $N_x \times L$ matrix,

$$\mathbf{G} = \mathbf{W}_1 \cdot \mathbf{A} \cdot \mathbf{C}, \tag{3.4}$$

and

$$\begin{aligned} p(\mathbf{x}, t+\Delta t) + p(\mathbf{x}, t-\Delta t) &= 2 \int e^{-i\mathbf{x}\mathbf{k}} W(\mathbf{x}, \mathbf{k}) \hat{p}(\mathbf{k}, t) d\mathbf{k} \\ &\approx 2 \sum_{m=1}^{L} G(\mathbf{x}, m) \left(\int e^{-i\mathbf{x}\mathbf{k}} B(\xi_m, \mathbf{k}) \hat{p}(\mathbf{k}, t) d\mathbf{k} \right) \\ &\approx \sum_{m=1}^{L} G(\mathbf{x}, m) \left(\int e^{-i\mathbf{x}\mathbf{k}} 2 \cos(\sum_{j=1}^{3} \xi_m^j k_j \Delta x_j) \hat{p}(\mathbf{k}, t) d\mathbf{k} \right) \\ &\approx \sum_{m=1}^{L} G(\mathbf{x}, m) \left[\int e^{-i\mathbf{x}\cdot\mathbf{k}} (e^{i \sum_{j=1}^{3} \xi_m^j k_j \Delta x_j} + e^{-i \sum_{j=1}^{3} \xi_m^j k_j \Delta x_j}) \hat{p}(\mathbf{k}, t) d\mathbf{k} \right]. \end{aligned} \tag{3.5}$$

According to the shift property of FFTs, we finally obtain an expression in the space-domain

$$p(\mathbf{x}, t+\Delta t) + p(\mathbf{x}, t-\Delta t) = \sum_{m=1}^{L} G(\mathbf{x}, m) [p(\mathbf{x}_L, t) + p(\mathbf{x}_R, t)], \tag{3.6}$$

where $\mathbf{x}_L = (x_1 - \xi_m^1 \Delta x_1, x_2 - \xi_m^2 \Delta x_2, x_3 - \xi_m^3 \Delta x_3)$, and $\mathbf{x}_R = (x_1 + \xi_m^1 \Delta x_1, x_2 + \xi_m^2 \Delta x_2, x_3 + \xi_m^3 \Delta x_3)$.

Equation 3.6 indicates a procedure of finite differences for wave extrapolation: the integer vector, $\xi_{\mathbf{m}} = (\xi_m^1, \xi_m^2, \xi_m^3)$ provides the stencil information, and $G(\mathbf{x}, m)$ stores the corresponding coefficients. I call this method *lowrank finite differences* (LFD) because the coefficients are derived from a lowrank approximation of the mixed-domain propagator matrix. The derived LFD scheme is expected to

accurately propagate seismic-wave components within a wide range of wavenumbers, which has advantages over conventional finite differences that focus mainly on small wavenumbers. In comparison with the Fourier-domain approach, the cost is reduced to $O(L\,N_x)$, where L is the order of the scheme.

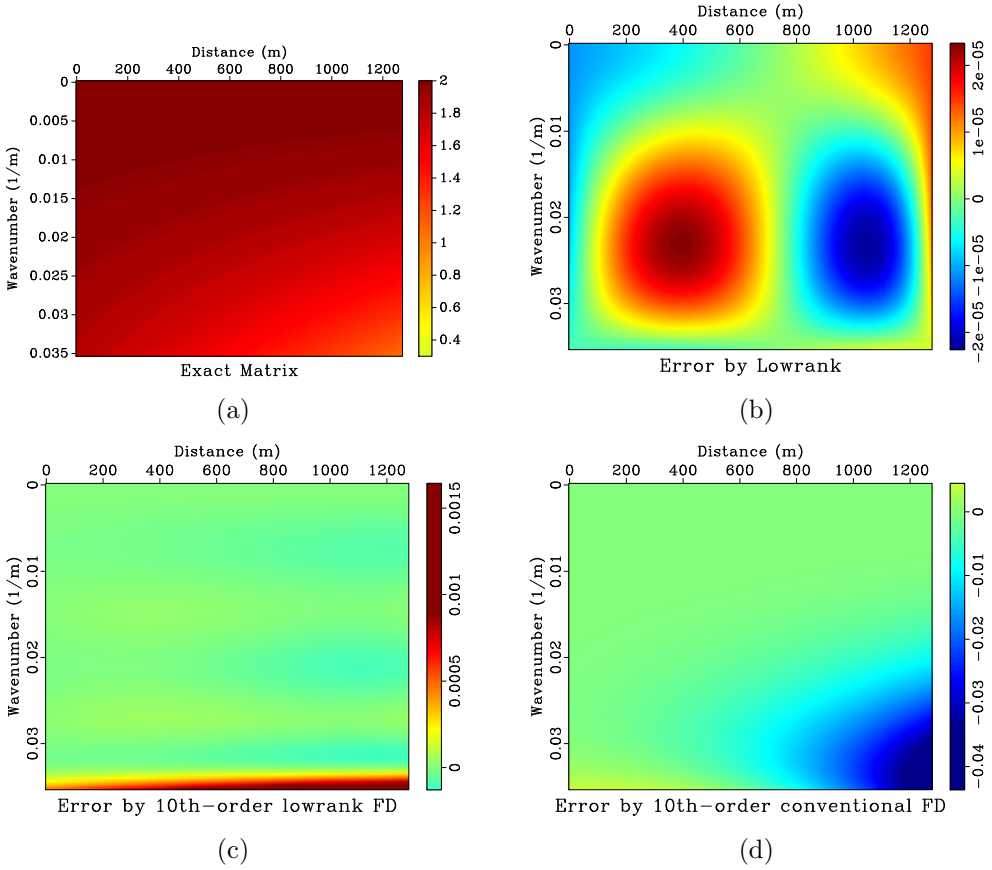

Figure 3.1: (a) Wavefield extrapolation matrix for 1-D linearly increasing velocity model. Error of wavefield extrapolation matrix by:(b) lowrank approximation, (c) the 10th-order lowrank FD (d) the 10th-order FD. opfd/oned Mexact,Mlrerr,Mapperr,Mfd10err

I first use a one-dimensional example to demonstrate the accuracy of the proposed LFD method. The velocity linearly increases from 1000 to 2275 m/s. The

time step is 1 ms. The propagator matrix is shown in Figure 3.1(a). Figure 3.1(b)-Figure 3.1(d) display the errors corresponding to different approximations. The error by the 10th-order lowrank finite differences (Figure 3.1(c)) appears significantly smaller than that of the 10th-order finite difference (Figure 3.1(d)). Figure 3.2 displays one selected column of the error matrix. Note that the error of the LFD is significantly closer to zero than that of the FD method.

To analyze the accuracy, we can let

$$p(\mathbf{x}, t) = e^{i(\mathbf{k}\cdot\mathbf{x}-\omega t)} \tag{3.7}$$

by using the plane wave theory. Inserting 3.7 into equation 3.6 and also adopting the dispersion relation $\omega = |k|\, v$, defines the phase velocity of LFD (v_{LFD}) as follows:

$$v_{LFD} = \frac{1}{|k|\Delta t} \arccos\Big(\sum_{m=1}^{L} G(\mathbf{x}, m)(\cos(\xi_m^1\, k_1 \Delta x_1) + \cos(\xi_m^2\, k_2 \Delta x_2) + \cos(\xi_m^3\, k_3 \Delta x_3))\Big), \tag{3.8}$$

For 1-D 10th order LFD, $L = 6$, $\xi_m = (\xi_m^1, 0, 0)$ and $\xi_m^1 = 0, 1, 2, 3, 4, 5$. With equation 3.8, we can calculate phase-velocities (v_{LFD}) by 1-D 10th order LFD with different velocities ($v = 2500, 3000, 3500, 4000$), and use the ratio $\delta = v_{LFD}/v$ to describe the dispersion of FD methods. Figure 3.3(a) displays 1D dispersion curves by 1-D 10th order LFD, and Figure 3.3(b) shows those by conventional FD method. Note that compared with the conventional FD method, LFD is accurate in a wide range of wavenumbers (70% of the Nyquist frequency).

The LFD approach is not limited to the isotropic case. In the case of transversely isotropic (TTI) media, the term $v(\mathbf{x})\,|\mathbf{k}|$ on the right-hand side of equa-

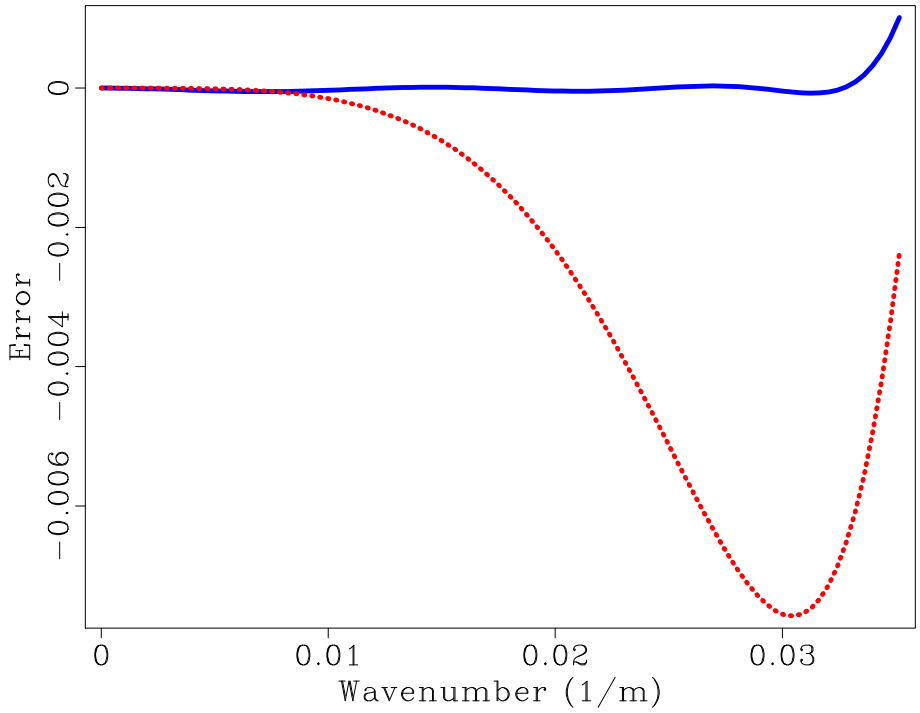

Figure 3.2: One selected column of the error matrix. Solid line: the 10th-order LFD. Dash line: the 10th-order FD. opfd/oned slicel

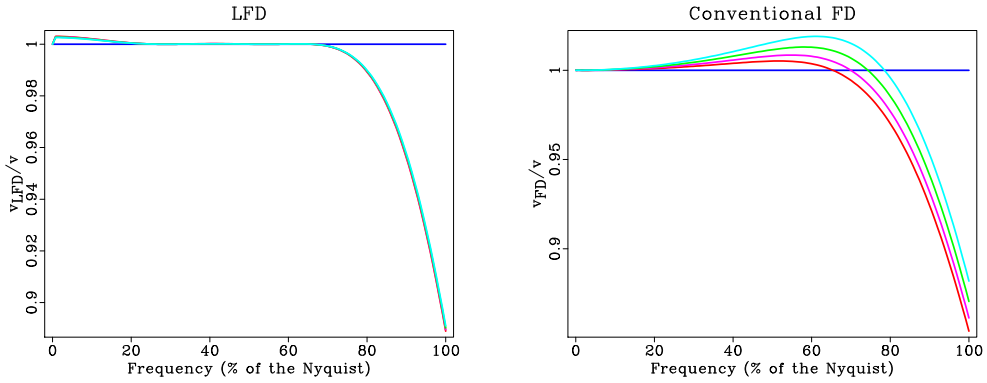

(a) (b)

Figure 3.3: Plot of 1-D dispersion curves for different velocities, $v = 2500$ (red), 3000 (pink), 3500 (green), 4000 (blue) m/s, $\Delta t = 1$ ms, $\Delta x = 10$ m by: (a) the 10th-order LFD (b) the 10th-order conventional FD. opfd/dispersion1 app,fd10

tion 1.15, can be replaced with the acoustic approximation 2.2. Using these definitions, I develop a version of the lowrank finite-difference scheme for TTI media.

Lowrank Fourier Finite Differences

In the previous chapter, I have introduced the FFD approach to solve the two-way wave equation. The FFD operator is a chain operator that combines FFT and FD (Ristow and Ruhl, 1994). In the TTI case, the FD scheme is a 4th-order operator, derived from Taylor's expansion around $k = 0$. However, it may exhibit some dispersion coming from the inaccuracy of the FD part: it requires around 4.5 sampling points per wavelength. I propose to replace the original FD operator with lowrank FD in order to increase the accuracy of FFD in isotropic and anisotropic media. The new operator is named lowrank Fourier Finite Differences (LFFD).

Numerical Examples

My first example is wave extrapolation in a 2-D, smoothly variable velocity model. The velocity ranges between 500 and 1300 m/s, and is formulated as

$$v(x,z) \;=\; 500 + 1.2 \times 10^{-4}(x-800)^2 + 10^{-4}(z-500)^2; \tag{3.9}$$

$$0 \le x \le 2560,\; 0 \le z \le 2560.$$

A Ricker-wavelet source with a 20 Hz dominant frequency (f_d) is located at the center of the model. The maximum frequency is around 60 Hz (f_{max}). The amplitude corresponding to f_{max} is about 10^{-5} of that of f_d.

For numerical simulations based on this model, I use the same grid size: $\Delta x = 5$ m and $\Delta t = 2$ ms.

I use $\alpha = v_{max}\,\Delta t/\Delta x$ to specify the stability condition and $\beta = v_{min}/(f_{max}\Delta x)$ as the dispersion factor, where v_{max} and v_{min} are the maximum and minimum velocities of the model. The dispersion factor β indicates the number of sampling points for the minimum wavelength. For simulations with above parameters, $\alpha \approx 0.52$ and $\beta \approx 1.67$.

It is easy to observe numerical dispersion on the snapshot computed by the 4th-order FD method (Figure 3.4(a)). The lowrank FD method with the same order exhibits higher accuracy and fewer dispersion artifacts (Figure 3.5(a)). Figure 3.5(b) displays the snapshot by the 10th-order LFD method with a larger time step: $\Delta t = 2.5$ ms, $\alpha \approx 0.65$. Note that the result is still accurate. However, the regular FD method is unstable in this case. For comparison, figure 3.4(b) displays the snapshot by the lowrank method with the same time step. Thanks to the spectral nature of the algorithm, the result appears accurate and free of disperion artifacts.

Next, I test the lowrank FD method in a complex velocity model. Figure 2.4 shows a part of the BP velocity model (Billette and Brandsberg-Dahl, 2004), which is a complicated model containing a salt body and sharp velocity contrasts on the flanks of the salt body. I use a Ricker-wavelet at a point source. The dominant frequency is 17 Hz ($f_{max} \approx 54Hz$). The horizontal grid size Δx is 12.5 m, the vertical grid size Δz is 12.5 m, and the time step is 1.5 ms. Thus $\alpha \approx 0.57$ and $\beta \approx 2.2$. In this case, I adopt a disk-shaped compact scheme (8th-order) for LFD with a 4-point radius ($|\xi| \leq 4$, $L = 25$). Figure 3.6 displays a wavefield snapshot in the above velocity model. The snapshot is almost free of dispersion. This experiment confirms that the lowrank FD method is able to handle sharp velocity variations.

The next example is wave propagation in a TTI model with a tilt of 45 ° and smooth velocity variation (v_x: 800-1225.41 m/s, v_z: 700-883.6 m/s). Figure 3.7(a) shows wavefield snapshots at different time steps by a 16th-order LFD operator in the TTI model. The space grid size is 5 m and the time step size is 2 ms. So $\alpha \approx 0.49$ and $\beta \approx 2.3$. For TTI model, I adopt a high-order (16th order) LFD operator in order to reduce dispersion. The scheme is compact and shaped as a disk with a radius of 8 points ($L = 99$).

In the previous chapter, I have shown an application of FFD method for TTI media. However, the wavefield snapshot by FFD method still has some dispersion because the FD scheme in the FFD operator is derived from Taylor's expansion around zero wavenumber. It is apparent that 4th-order FD scheme is not accurate enough for TTI case and requires denser sampling per wavelength ($\beta \approx 4.6$). Here I propose to replace that 4th-order FD operator with an 8th-order compact scheme. The proposed scheme has the shape of a disk with a radius of 4 points ($L = 25$), the same as the one for LFD in the above BP model. Figure 3.7(b) shows wavefield snapshots by the proposed LFFD operator. The time step size is 1.5 ms ($\alpha \approx 0.37$). Note that the wavefront is clean and almost free of dispersion with $\beta \approx 2.3$. Because I use the exact dispersion relation, Equation 1.16, for TTI computation, there is no coupling of q-SV wave and q-P wave (Grechka et al., 2004; Zhang et al., 2009; Duveneck et al., 2008) in these snapshots by either LFD or LFFD methods.

Next I test the LFD and LFFD methods in a complex TTI model. Fig-

ure 2.14(a)-2.14(d) shows parameters for part of the BP 2D TTI model. The dominant frequency is 15 Hz ($f_{max} \approx 50$). The space grid size is 12.5 m and the time step is 1 ms. So $\alpha \approx 0.42$ and $\beta \approx 2.4$. Both methods are able to simulate an accurate qP-wave field in this model as shown in Figure 3.8 and 3.9.

It is difficult to provide analytical stability analysis for the LFD and LFFD operators. In my experience, LFD appears to allow for a larger time step size than does the LFFD method. In TTI case, the conventional FD method for acoustic TTI has known issues of instability caused by shear-wave numerical artifacts or sharp changes in the symmetry axis tilting (Grechka et al., 2004; Zhang et al., 2009; Duveneck et al., 2008). Conventional methods may place limits on anisotropic parameters, smooth parameter models or include a finite shear-wave velocity to alleviate the instability problem(Yoon et al., 2004; Zhang and Zhang, 2008; Fletcher et al., 2009). Both LFD and LFFD methods are free of shear-wave artifacts. They have no particular bounds for anisotropic parameters and are capable of handling sharp tilt changes.

Conclusions

Explicit finite difference (FD) methods are the most popular and straightforward methods for seismic modeling and seismic imaging, particularly for reverse-time migration (RTM). Traditionally the coefficients of the FD schemes are derived from a Taylor series expansion around the zero wavenumber. In this chapter, I present a novel FD scheme: Lowrank Finite Differences (LFD), which is based on the lowrank approximation of the mixed-domain space-wavenumber propagator. LFD uses compact FD schemes, which are more suitable for parallelization on multi-core computers

than spectral methods that require FFT operations. This technique promises higher accuracy than that of the conventional, explicit FD method: it requires only about 2.2 sampling points per wavelength. This technique promises higher accuracy and better stability than those of the conventional, explicit FD method. I also propose to replace the 4th-order FD operator based on Taylor's expansion in Fourier Finite Differences (FFD) with an 8th-order LFD operator to reduce dispersion, particularly in the TTI case. Results from synthetic experiments illustrate the stability of the proposed methods in complicated velocity models. In TTI media, there is no coupling of qP-waves and qSv-waves by either method. Both methods can be incorporated in seismic imaging by reverse-time migration to enhance its accuracy and stability.

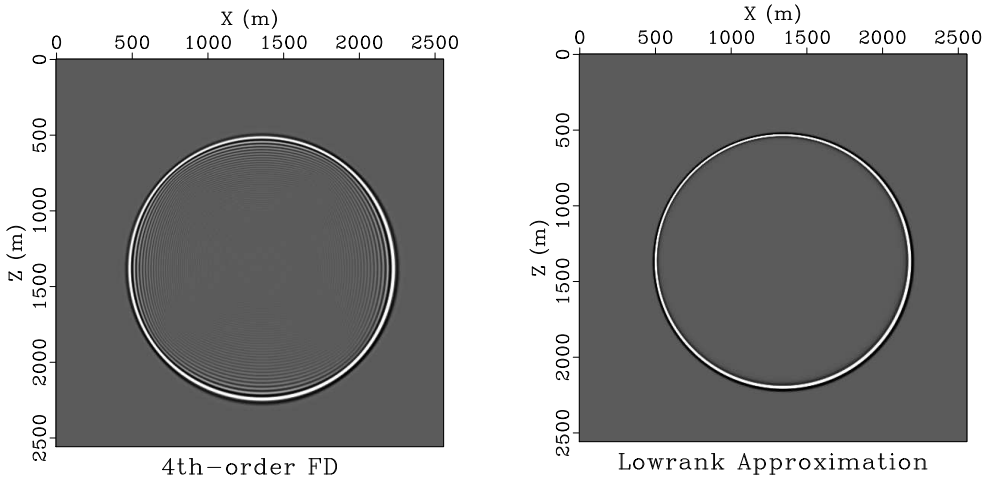

Figure 3.4: Wavefield snapshot in a varable velocity field by: (a) conventional 4th-order FD method (b) Lowrank method. opfd/twod wavfd7sn,wavel

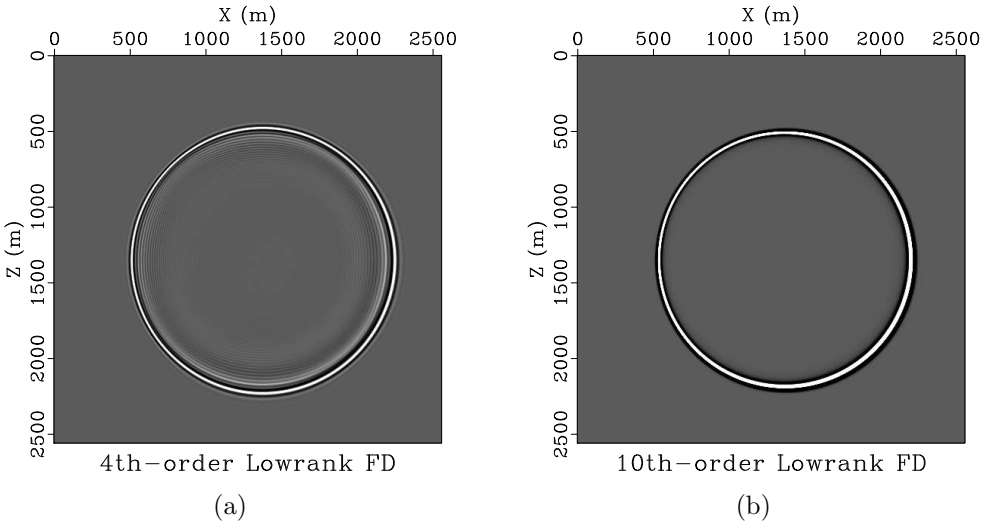

Figure 3.5: Wavefield snapshot in a varable velocity field by: (a) the 4th-order lowrank FD method (b) the 10th-order lowrank FD method. Note that the time step is 2.5 ms and the LFD result is still accurate. However, the FD method becomes unstable in this case. opfd/twod wavapp7sn,wavapp10sn

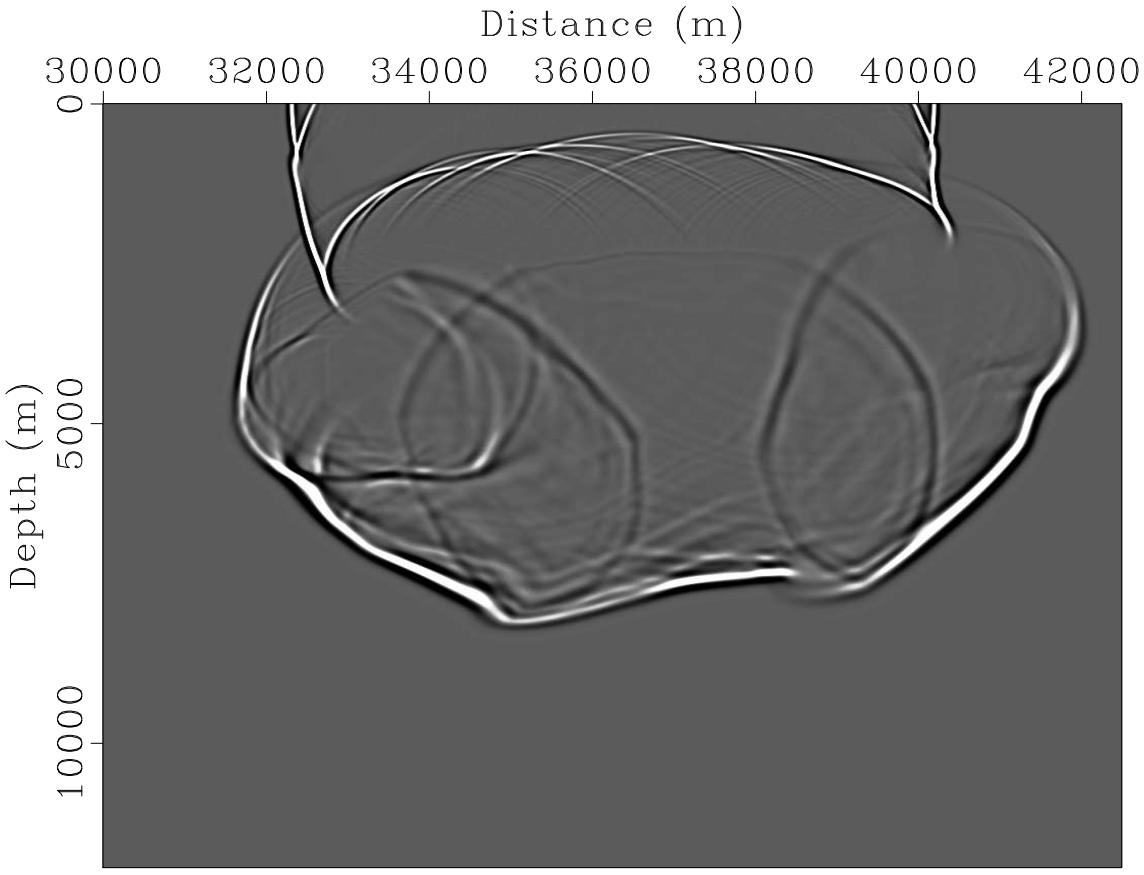

Figure 3.6: Wavefield snapshot by the 8th-order lowrank FD (compact scheme) in the BP Model shown in Figure 2.4. opfd/bp wavsnapabc

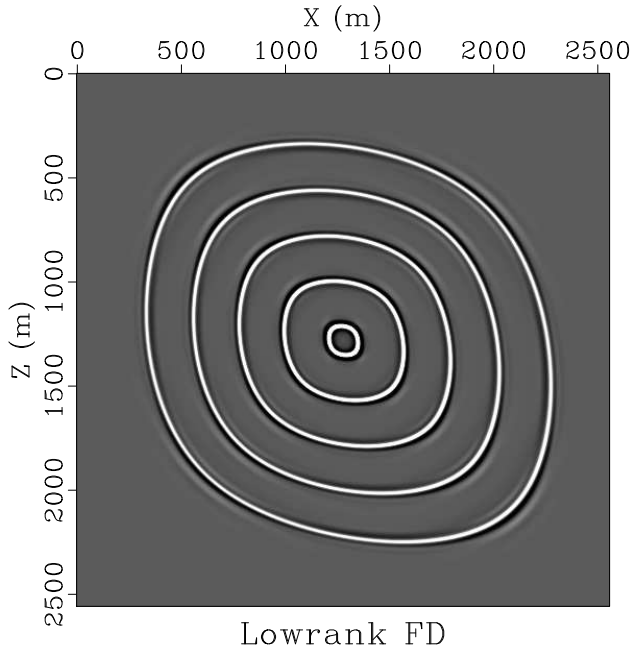

(a)

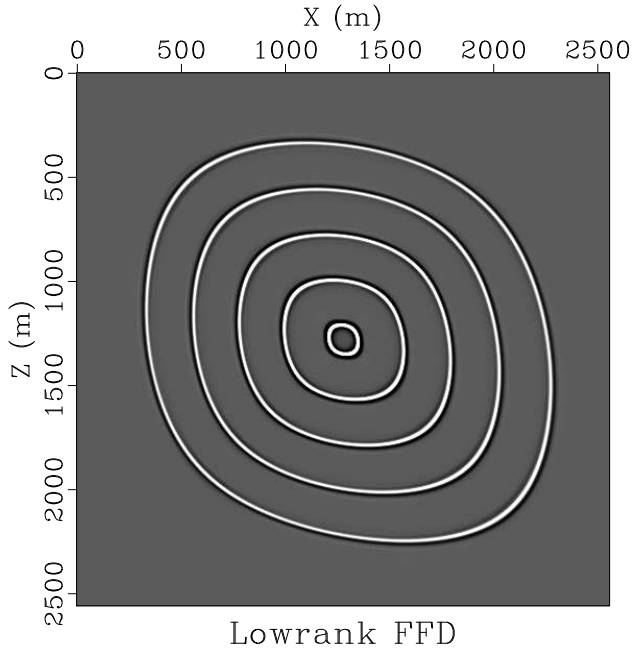

(b)

Figure 3.7: Wavefield snapshots in a TTI medium with a tilt of 45° by: (a) Lowrank FD method; (b) Lowrank FFD method.$v_x(x,z) = 800 + 10^{-4}(x - 1000)^2 + 10^{-4}(z - 1200)^2$; $v_z(x,z) = 700 + 10^{-4}(z - 1200)^2$; $\eta = 0.3$; $\theta = 45°$. opfd/aniso snapshotlfd,snapshotlffd

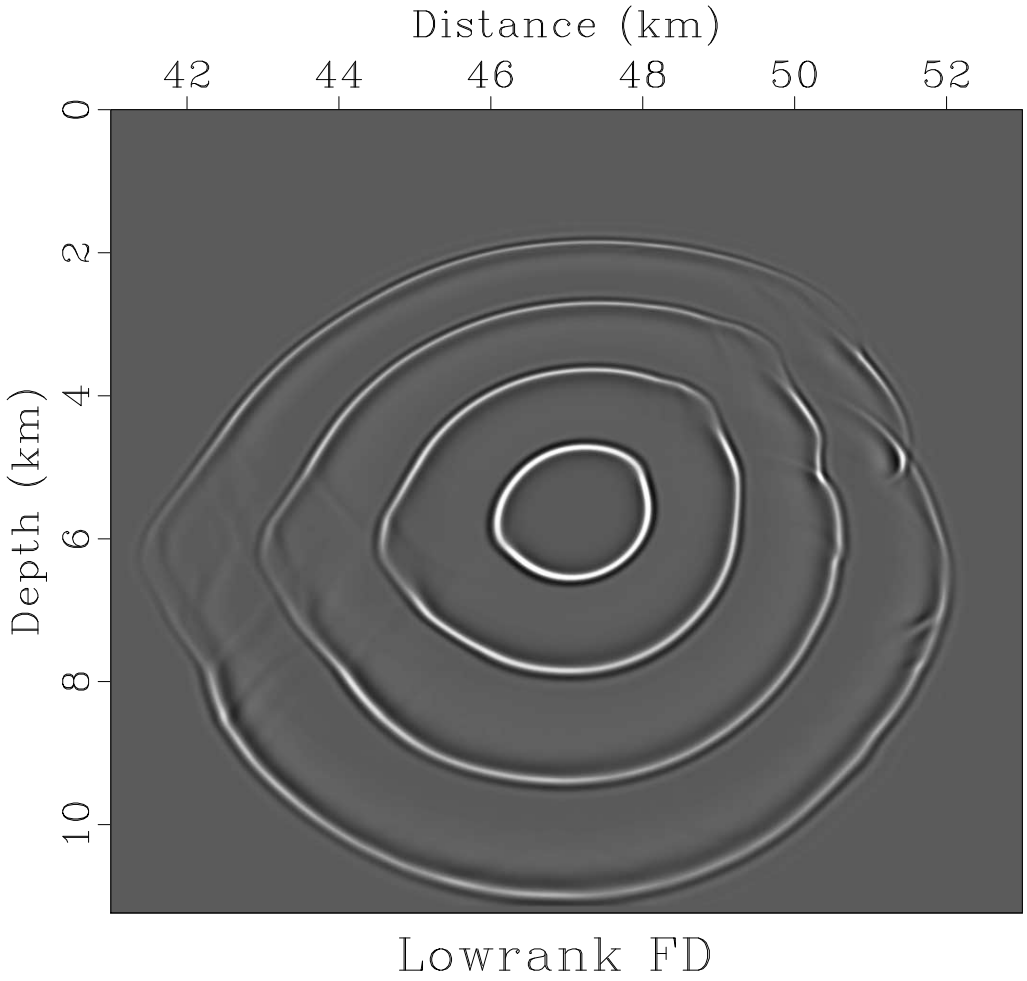

Figure 3.8: Scalar wavefield snapshots by LFD method in the 2D BP TTI model. opfd/bptti snapshotslfd

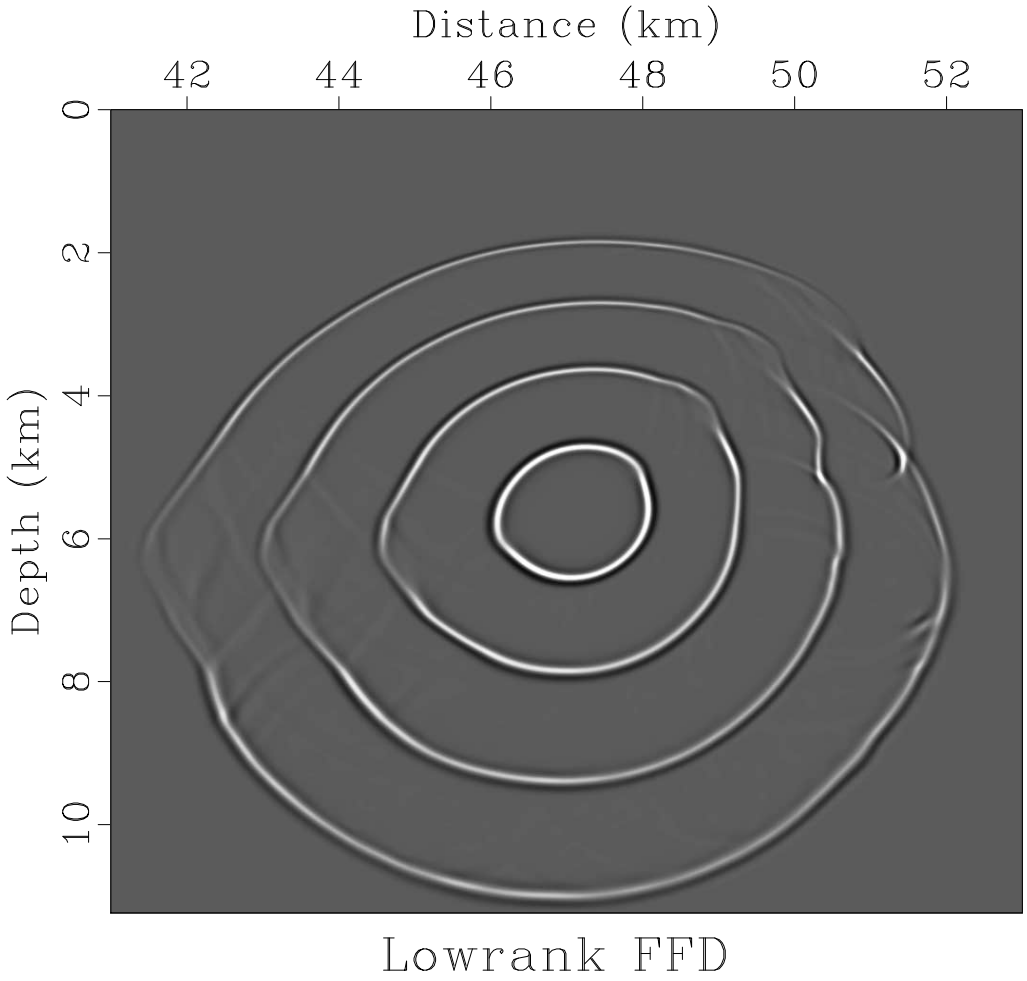

Figure 3.9: Scalar wavefield snapshots by LFFD method in the 2D BP TTI model. opfd/bptti snapshotslffd

Chapter 4

Modeling of pseudo-acoustic P-waves in orthorhombic media with lowrank approximation

In this chapter, I adopt a dispersion relation for orthorhombic anisotropic media (Alkhalifah, 2003) and introduce a mixed-domain pseudo-acoustic P-wave extrapolator for time marching in orthorhombic media. I use lowrank approximation (Fomel et al., 2010, 2012) to handle this mixed-domain operator. I demonstrate by numerical examples that the proposed operator is kinematically accurate. Furthermore, there is no coupling of quasi-P and quasi-SV waves in the wavefield and no such particular constraints on Thomsen's parameters required for stability as in conventional FD methods (Yoon et al., 2004).

Dispersion Relation for Orthorhombic Anisotropic Media

Theoretically, the problem of wave extrapolation in time can be reduced to analyzing numerical approximations to the mixed-domain space-wavenumber operator (Wards et al., 2008). In the case of orthorhombic pseudo-acoustic modeling, a new phase operator $\phi(\mathbf{x}, \mathbf{k})$ is derived to replace $|\mathbf{k}|v(\mathbf{x})$ of the isotropic model as shown in equation 1.13 and 1.14.

Parts of this chapter appear in Song and Alkhalifah (2012).

In transversely isotropic (TI) media, the model is fully characterized by five elastic parameters and density. In orthorhombic media, nine elastic parameters and density are needed to describe the elastic model. The stiffness tensor c_{ijkl} for an orthorhombic model can be represented, using the compressed two-index Voigt notation, as follows:

$$\mathbf{C} = \begin{bmatrix} c_{11} & c_{12} & c_{13} & 0 & 0 & 0 \\ c_{12} & c_{22} & c_{23} & 0 & 0 & 0 \\ c_{13} & c_{23} & c_{33} & 0 & 0 & 0 \\ 0 & 0 & 0 & c_{44} & 0 & 0 \\ 0 & 0 & 0 & 0 & c_{55} & 0 \\ 0 & 0 & 0 & 0 & 0 & c_{66} \end{bmatrix}. \tag{4.1}$$

Instead of strictly adhering to the orthorhombic media used by Tsvankin (1997, 2005), Alkhalifah (2003) slightly changed the notations and used the following nine parameters determined from the above stiffness tensor:

$$\begin{aligned} v_v &= \sqrt{\tfrac{c_{33}}{\rho}} \\ v_{s1} &= \sqrt{\tfrac{c_{55}}{\rho}} \\ v_{s2} &= \sqrt{\tfrac{c_{44}}{\rho}} \\ v_{s3} &= \sqrt{\tfrac{c_{66}}{\rho}} \\ v_1 &= \sqrt{\frac{c_{13}(c_{13}+2c_{55})+c_{33}c_{55}}{\rho(c_{33}-c_{55})}} \\ v_2 &= \sqrt{\frac{c_{23}(c_{23}+2c_{44})+c_{33}c_{44}}{\rho(c_{33}-c_{44})}} \\ \eta_1 &= \frac{c_{11}(c_{33}-c_{55})}{2c_{13}(c_{13}+2c_{55})+2c_{33}c_{55}} - \frac{1}{2} \\ \eta_2 &= \frac{c_{22}(c_{33}-c_{44})}{2c_{23}(c_{23}+2c_{44})+2c_{33}c_{44}} - \frac{1}{2} \\ \delta &= \frac{(c_{12}+c_{66})^2-(c_{11}-c_{66})^2}{2c_{11}(c_{11}-c_{66})}, \end{aligned} \tag{4.2}$$

where v_v is P-wave vertical phase velocity, v_{s1} and v_{s2} are S-wave vertical phase velocity polarized in the $[x_2, x_3]$ and $[x_1, x_3]$ planes, v_{s3} is S-wave horizontal phase velocity

polarized in the $[x_1, x_3]$ but propagating in the x_1 direction, v_1 and v_2 are NMO P-wave velocities for horizontal reflectors in the $[x_1, x_3]$ and $[x_2, x_3]$ planes, and η_1, η_2, and δ are anisotropic parameters in the $[x_1, x_3]$, $[x_2, x_3]$, and $[x_1, x_2]$ planes.

The Christoffel equation in 3D anisotropic media takes the following general form (Chapman, 2004):

$$\Gamma_{ik}(x_s, \mathbf{p}) = a_{ijkl}(x_s) p_j p_l - \delta_{ik}, \tag{4.3}$$

with $p_j = \frac{\partial \tau}{\partial x_j}$ and $a_{ijkl} = \frac{c_{ijkl}}{\rho}$, where p_j are components of the phase vector $\mathbf{p}$, τ is travel-time along the ray, ρ is density, $x_s, s = 1, 2, 3$ are Cartesian coordinates for position along the ray, and δ_{ik} is the Kronecker delta function.

Alkhalifah (1998) pointed out that careful reparametrization followed by setting the shear velocity along the symmetry axis to zero does not compromise accuracy in traveltime computations for TI media. This conclusion can be applied to orthorhombic media as well (Tsvankin, 1997). Alkhalifah (2003) showed that the kinematics of wave propagation are well described by the acoustic approximation.

In orthorhombic media, the Christoffel equation (4.3) reduces to the following form if v_{s1}, v_{s2}, and v_{s3} are set to zero:

$$\begin{bmatrix} p_1^2 v_1^2 \xi_1 - 1 & \gamma p_1 p_2 v_1^2 \xi_1 & p_1 p_3 v_1 v_v \\ \gamma p_1 p_2 v_1^2 \xi_1 & p_2^2 v_2^2 \xi_2 - 1 & p_2 p_3 v_2 v_v \\ p_1 p_3 v_1 v_v & p_2 p_3 v_2 v_v & p_3^2 v_v^2 - 1 \end{bmatrix}, \tag{4.4}$$

where $\xi_1 = 1 + 2\eta_1$ and $\xi_2 = 1 + 2\eta_2$.

After taking the determinant of matrix (4.4), setting the determinant to zero and replacing p_1 with $\frac{k_x}{\phi}$, p_2 with $\frac{k_y}{\phi}$, and p_3 with $\frac{k_z}{\phi}$, one can obtain a cubic polynomial in ϕ^2 as follows:

$$\begin{array}{l} -\phi^6 + \phi^4 \left(2v_1^2\eta_1 k_x^2 + v_1^2 k_x^2 + 2v_2^2\eta_2 k_y^2 + v_2^2 k_y^2 + v_v^2 k_z^2\right) \\ +\phi^2(v_1^4\gamma^2\xi_1^2 k_x^2 k_y^2 - v_2^2 v_1^2 \xi_1\xi_2 k_x^2 k_y^2 - 2v_v^2 v_1^2\eta_1 k_x^2 k_z^2 \\ -2v_2^2 v_v^2\eta_2 k_y^2 k_z^2) - v_1^4 v_v^2\gamma^2\xi_1^2 k_x^2 k_y^2 k_z^2 + 2v_1^3 v_2 v_v^2\gamma\xi_1 k_x^2 k_y^2 k_z^2 \\ -v_1^2 v_2^2 v_v^2 \left(1 - 4\eta_1\eta_2\right) k_x^2 k_y^2 k_z^2 = 0 \ , \end{array} \tag{4.5}$$

in which $\gamma = \sqrt{1 + 2\delta}$.

One of the roots of the cubic polynomial corresponds to P-waves in acoustic media and is given by the following expression:

$$\phi^2 = \frac{1}{6}\left|-2^{2/3}d - \frac{2\sqrt[3]{2}\left(a^2 + 3b\right)}{d} + 2a\right| \ , \tag{4.6}$$

where

$$a = 2v_1^2\eta_1 k_x^2 + v_1^2 k_x^2 + 2v_2^2\eta_2 k_y^2 + v_2^2 k_y^2 + v_v^2 k_z^2,$$

$$b = v_1^4 k_x^2 k_y^2 \left(2\gamma\eta_1 + \gamma\right)^2 - v_2^2 v_1^2 \left(2\eta_1 + 1\right)\left(2\eta_2 + 1\right) k_x^2 k_y^2$$

$$-2v_v^2 v_1^2\eta_1 k_x^2 k_z^2 - 2v_2^2 v_v^2\eta_2 k_y^2 k_z^2,$$

$$c = v_v^2 v_1^4 \left(-k_x^2\right) k_y^2 k_z^2 \left(2\gamma\eta_1 + \gamma\right)^2 + 2v_2 v_v^2 v_1^3\gamma\left(2\eta_1 + 1\right) k_x^2 k_y^2 k_z^2$$

$$-v_2^2 v_v^2 v_1^2 \left(1 - 4\eta_1\eta_2\right) k_x^2 k_y^2 k_z^2,$$

$$d = \sqrt[3]{-2a^3 + 3\left(e - 9c\right) - 9ab},$$

$$e = \sqrt{|-3b^2\left(a^2 + 4b\right) + 6ac\left(2a^2 + 9b\right) + 81c^2|}.$$

This root reduces to the isotropic P-wave solution when we set $v_1 = v_2 = v_3 = v$, $\eta_1 = \eta_2 = 0$, and $\gamma = 1$, in which ϕ in expression (4.6) is then given by $|\mathbf{k}|v$, which is the same dispersion relation in isotropic media as that shown in equation (1.15).

And in TTI media: $v_1 = v_2 = v$, $\eta_1 = \eta_2 = \eta$, and $\gamma = 1$, ϕ in expression (4.6) reduces to

$$\phi(\mathbf{x},\mathbf{k}) = \sqrt{\frac{1}{2}(v_h^2\,k_h^2 + v_v^2\,k_z^2) + \frac{1}{2}\sqrt{(v_h^2\,k_h^2 + v_v^2\,k_z^2)^2 - \frac{8\eta}{1+2\eta}v_h^2 v_v^2\,k_h^2\,k_z^2}}\,, \tag{4.7}$$

where $v_h = \sqrt{1+2\eta}v$ is the P-wave phase velocity in the direction normal to the symmetry axis, and $k_h = \sqrt{k_x^2 + k_y^2}$. Expression 4.7 is the same as the dispersion relation for TTI media (Alkhalifah, 1998, 2000; Fomel, 2004).

Tilted Orthorhombic Anisotropy

Tectonic movement of the crust may rotate the rocks and tilt the plane containing the vertical cracks, causing a tilted anisotropy. In the case of tilted orthorhombic media, k_x, k_y, and k_z need to be replaced by $\hat{k}_x$, $\hat{k}_y$, and $\hat{k}_z$, which are wavenumbers evaluated in a rotated coordinate system aligned with the vectors normal to the orthorhombic symmetry planes:

$$\begin{aligned}
\hat{k}_x &= k_x\cos\phi + k_y\sin\phi \\
\hat{k}_y &= -k_x\sin\phi\cos\theta + k_y\cos\phi\cos\theta + k_z\sin\theta \\
\hat{k}_z &= k_x\sin\phi\sin\theta - k_y\cos\phi\sin\theta + k_z\cos\theta\,,
\end{aligned} \tag{4.8}$$

where θ is the dip angle measured with respect to vertical and ϕ is the azimuth angle, which is the angle between the projection of the original Y-coordinate and the original X-coordinate. The original vertical axis has the direction of $\{\sin\theta\sin\phi, -\sin\theta\cos\phi, \cos\theta\}$. For a more general rotation, one needs three angles to describe the transformation (Zhang and Zhang, 2011).

Lowrank Approximation

I use the mixed-domain operator of ϕ in equation (4.6) as the dispersion relation for orthorhombic media. Considering inhomogeneous media, I choose lowrank approximation (Fomel et al., 2010, 2012) described in the first chapter to implement the mixed-domain operator.

I propose using the above lowrank approximation algorithm to handle mixed-domain operator ϕ in equation 4.6 for wave extrapolation in orthorhombic media.

Numerical Examples

Figure 4.1(a)–4.1(c) shows wavefield snapshots (depth, inline, and crossline) in a vertical orthorhombic medium with constant parameters: $v_v = 2km/s$, $v_1 = 2.1km/s$, $v_2 = 2.05km/s$, $\eta_1 = 0.3$, $\eta_2 = 0.1$, and $\gamma = 1$. The time-step size is 1 ms and the space grid sizes in three directions are all 25 m. As the model is homogeneous, the rank is 1 for the lowrank decomposition. The depth slice is anelliptical, whereas the inline and crossline display different diamond shapes, indicating different VTI properties. In Figures 4.1(a)–4.1(c), red dashed lines are calculated using ray tracing. Note that the red dashed lines match the wavefront from the lowrank method very well.

To show that the lowrank approximation method can handle rough velocity models, we use a two-layer velocity model with high velocity contrast. The first layer has lower velocity parameters: $v_v = 1.5km/s$, $v_1 = 1.6km/s$, $v_2 = 1.7km/s$,

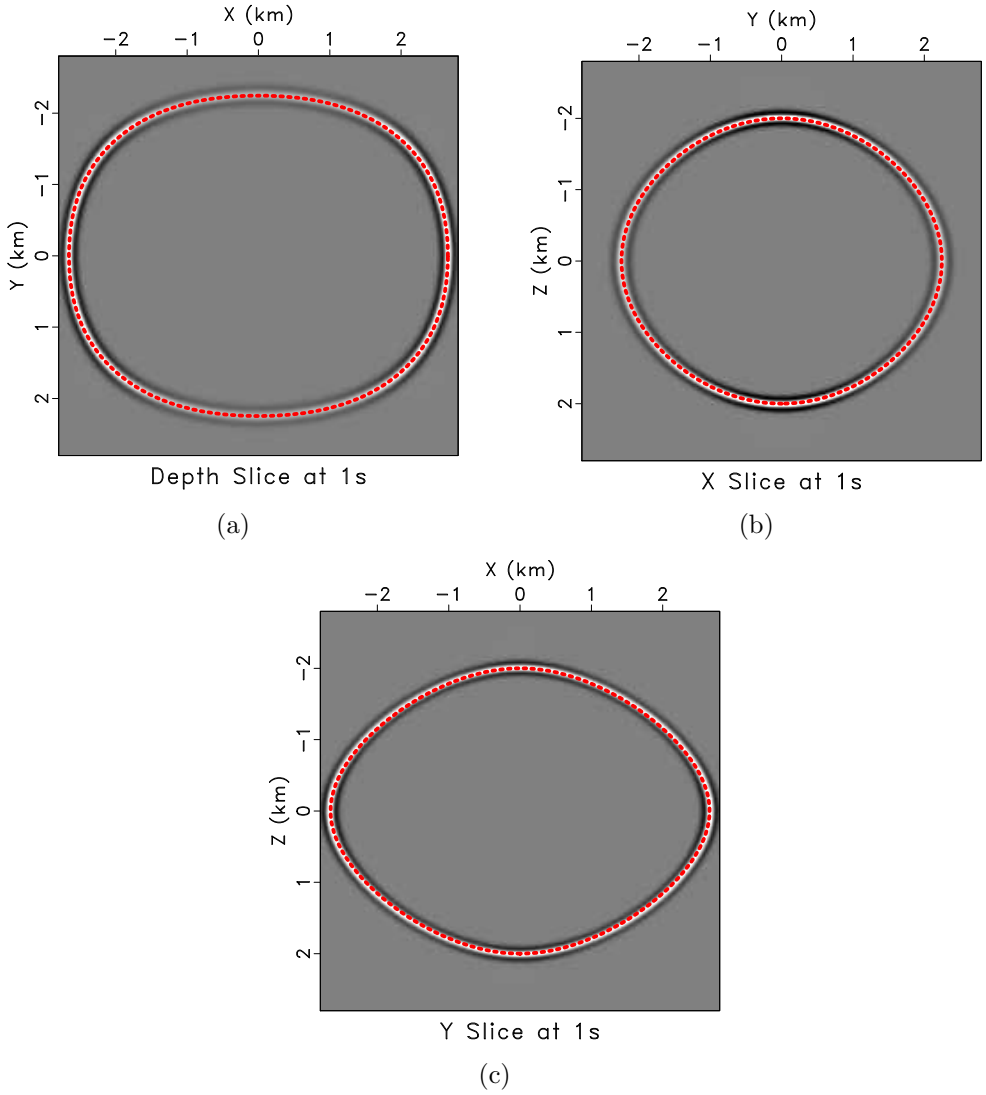

Figure 4.1: Three slices of the wavefield snapshot by the dispersion relation 4.6 at 1 second in a vertical orthorhombic medium: (a) Depth Slice; (b) Inline Slice; (c) Crossline Slice. Also plotted are red curves representing the wavefront at that time calculated using raytracing. orthorhombic/orth wavexy,waveyz,wavexz

while the values in the other layer are much higher: $v_v = 3.5km/s$, $v_1 = 4.1km/s$, $v_2 = 4.2km/s$. And we use the same anisotropic parameters for both layers: $\eta_1 = 0.3$, $\eta_2 = 0.1$, and $\gamma = 1$. For this test, we use a time step size of 1 ms and a space grid size of 25 m. The rank is 2 calculated by the lowrank decomposition within an error level of 10^{-5}. Figure 4.2(a) displays the depth slice above the reflector at 0.6 second. Note the snapshot shows the reflection from the velocity contrast. Figure 4.2(b) and 4.2(c) show the inline and crossline slices, which indicate strong anisotropy in the medium.

The next example is wavefield snapshots in a rotated and tilted orthorhombic model ($\theta = \phi = 45^\circ$) with smoothly varying velocity– v_1: 1500–3088 m/s, v_2: 1500–3686 m/s, v_v: 1500–3474 m/s, $\eta_1 = 0.3$, $\eta_2 = 0.1$, and $\gamma = 1.03$. The time-step size is 4 ms. Figure 4.3(a)–4.3(c) shows corresponding wavefield snapshots by the dispersion relation 4.6 in depth, inline, and crossline slices through the central source location. The inline section (Figure 4.3(b)) displays the strongest anisotropic property, because η_1 is as large as 0.3. Note that the snapshots are free of dispersion and that there is no coupling of qSV and qP waves in the middle. Lowrank parameters were $M = 7$ and $N = 7$. Therefore, the cost is 7 FFTs at each time step.

Table 4.1 displays rank N required for maintaining an error level of 10^{-5} with different time step size Δt. From table 4.1, one could find for this smooth model, $\Delta t = 4$ ms and $N = 7$ is the optimal choice for cost consideration.

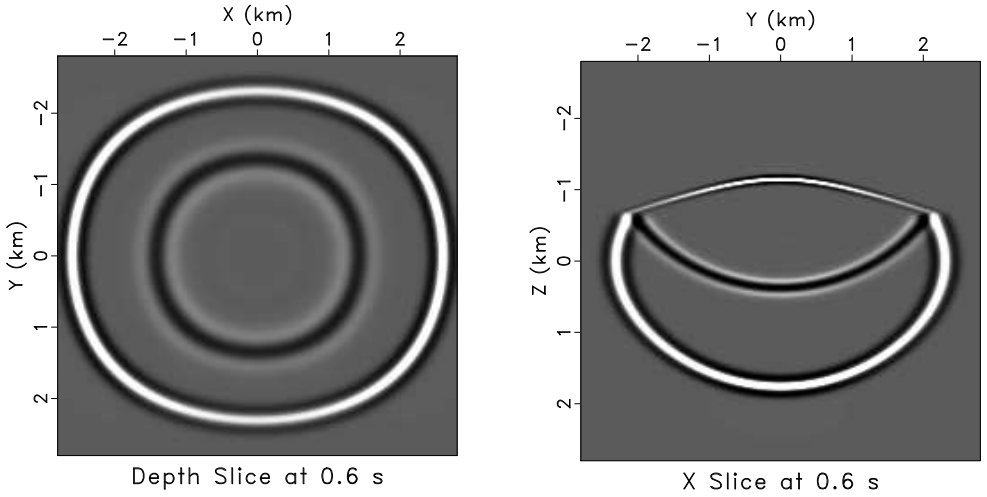

(a)

(b)

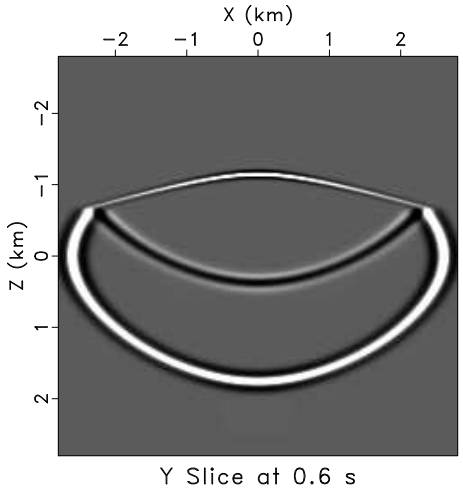

(c)

Figure 4.2: Three slices of the wavefield snapshot by the dispersion relation 4.6 at 0.6 second in a 2-layer vertical orthorhombic model (high velocity contrast): (a) Depth Slice; (b) Inline Slice; (c) Crossline Slice. orthorhombic/test wavexyt,waveyzt,wavexzt

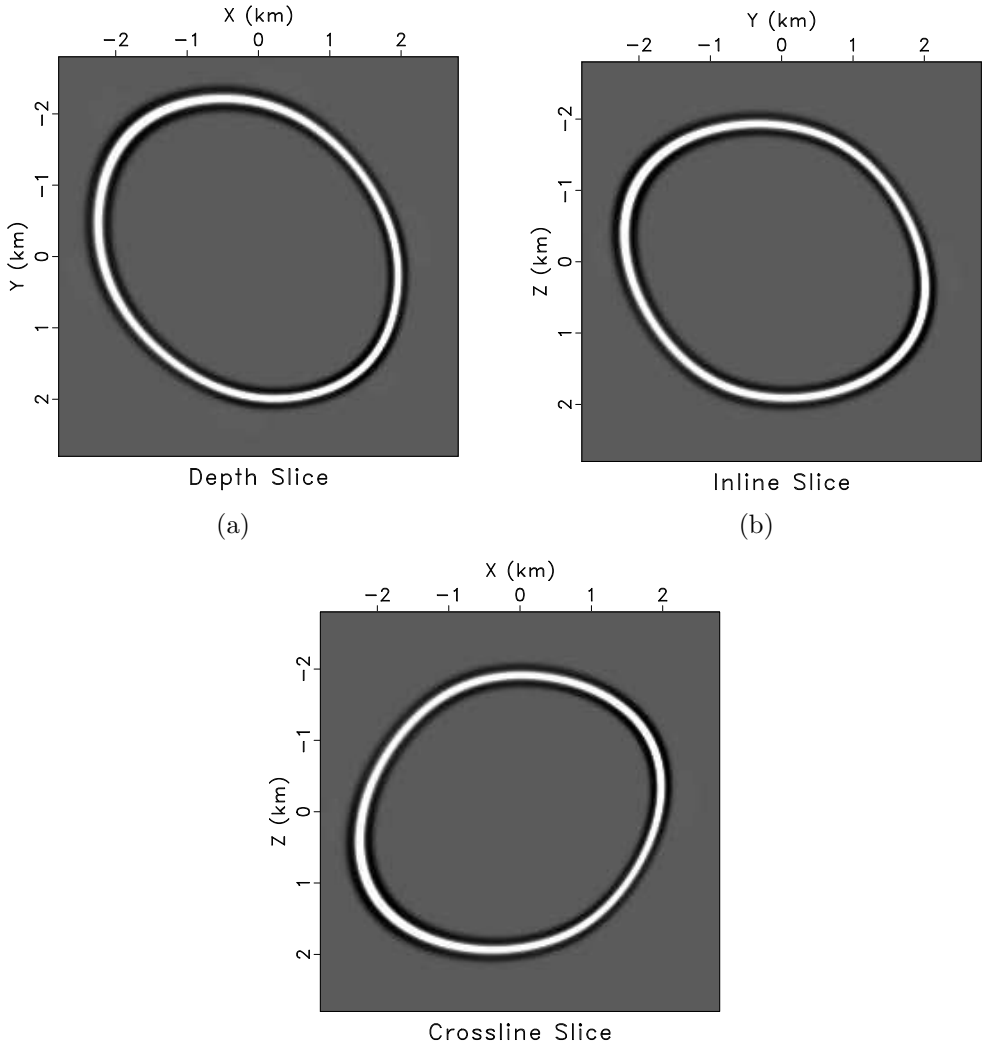

Figure 4.3: Wavefield snapshots by the dispersion relation 4.6 in an rotated and tilted orthorhombic medium ($\theta = \phi = 45\,^\circ$) with variable velocity: (a) Depth Slice; (b) Inline Slice; (c) Crossline Slice orthorhombic/tiltn snapxy4,snapyz4,snapxz4

Δt (ms)	0.5	1	2	3	4	5
$RankN$	5	5	7	7	7	12

Table 4.1: Rank N calculated from the lowrank approximation of the propagation matrix for a 2D smooth orthorhombic model with different time step size Δt at a given error level 10^{-5}.

Conclusions

I derive and adopt an approximate dispersion relation for orthorhombic media so as to model seismic wavefields in such media. To handle the space-wavenumber mixed-domain operator, I apply lowrank approximation to reduce computational cost. Numerical experiments show that the proposed wavefield extrapolator is accurate. There is no coupling of qSV and qP in the wavefield snapshots because the exact dispersion relation is used. In addition, the proposed approach yields practically dispersion-free wavefields, and is also free of stability limitations on media parameters.

Chapter 5

RTM examples with Fourier finite-differences

In this chapter, I apply the FFD algorithm to RTM with a simple exponential decaying boundary condition (Cerjan et al., 1985). The FFD RTM code is designed to distribute shot gathers to different computing nodes by MPI and within the node, OpenMP is used to thread the corresponding FFT and FD operations. I use the same design for both isotropic (`sfffdrtms`) and TTI (`sfttirtmsa`) RTM. Then I apply FFD RTM to isotropic, VTI and TTI cases, including a test to real dataset provided by BP.

sfffdrtms: 2-D FFD isotropic RTM: MPI + OMP

```
sfffdrtms geo=geo.rsf vel=vel.rsf source=source.rsf opt=y dt= nt= isz=
irz=isz jr=1 jm=20 nr= nbt=44 nbb=44 nbl=44 nbr=44 ct=0.01 cb=0.01
cl=0.01 cr=0.01 sht=0 tskip=0 left=2400 right=800
```

float	**cb=0.01**		decaying parameter
float	**cl=0.01**		decaying parameter
float	**cr=0.01**		decaying parameter
float	**ct=0.01**		decaying parameter
float	**dt=**		time step size
file	**geo=**		auxiliary input file name
int	**irz=isz**		receiver depth
int	**isz=**		source depth
int	**jm=20**		snap sampling
int	**jr=1**		receiver sampling
int	**left=2400**		left
int	**nbb=44**		boundary nodes
int	**nbl=44**		boundary nodes
int	**nbr=44**		boundary nodes
int	**nbt=44**		boundary nodes
int	**nr=**		streamer total length
int	**nt=**		total time length
bool	**opt=y**	[y/n]	optimal padding
int	**right=800**		right
int	**sht=0**		Time shift parameter
file	**source=**		auxiliary input file name
int	**tskip=0**		Time shift parameter
file	**vel=**		auxiliary input file name

sfttirtmsa: 2-D TTI FFD RTM: MPI + OMP

```
sfttirtmsa geo=geo.rsf velx=velx.rsf velz=velz.rsf yita=yita.rsf
source=source.rsf seta=seta.rsf opt=y de=y dt= nt= isz= irz=isz jr=1
jm=20 tskip=1000 sht=0 nr= err=0.00001 nbt=102 nbb=102 nbl=128 nbr=127
ct=0.02 cb=0.02 cl=0.02 cr=0.02 ratio=2.0 left=nr*3/2*jr right=nr/2*jr
```

float	**cb=0.02**		decaying parameter
float	**cl=0.02**		decaying parameter
float	**cr=0.02**		decaying parameter
float	**ct=0.02**		decaying parameter
bool	**de=y**	[y/n]	in angle
float	**dt=**		time step size
float	**err=0.00001**		error control
file	**geo=**		auxiliary input file name
int	**irz=isz**		receiver depth
int	**isz=**		source depth
int	**jm=20**		snap sampling
int	**jr=1**		receiver sampling
int	**left=nr*3/2*jr**		left
int	**nbb=102**		boundary nodes
int	**nbl=128**		boundary nodes
int	**nbr=127**		boundary nodes
int	**nbt=102**		boundary nodes
int	**nr=**		streamer total length
int	**nt=**		total time length
bool	**opt=y**	[y/n]	optimal padding
float	**ratio=2.0**		v0/vmax
int	**right=nr/2*jr**		right
file	**seta=**		auxiliary input file name
int	**sht=0**		time shift
file	**source=**		auxiliary input file name
int	**tskip=1000**		time skipped
file	**velx=**		auxiliary input file name
file	**velz=**		auxiliary input file name
file	**yita=**		auxiliary input file name

The first model shown in figure 5.1 was created for the 1998 SEG talk (Etgen and Regone, 1998) and is also mentioned by Dellinger et al. (2000). It is provided at `http://software.seg.org` courtesy of BP. John Etgen describes this model as

"The Carpathians thrusting over the North Sea". The maximum frequency is 60

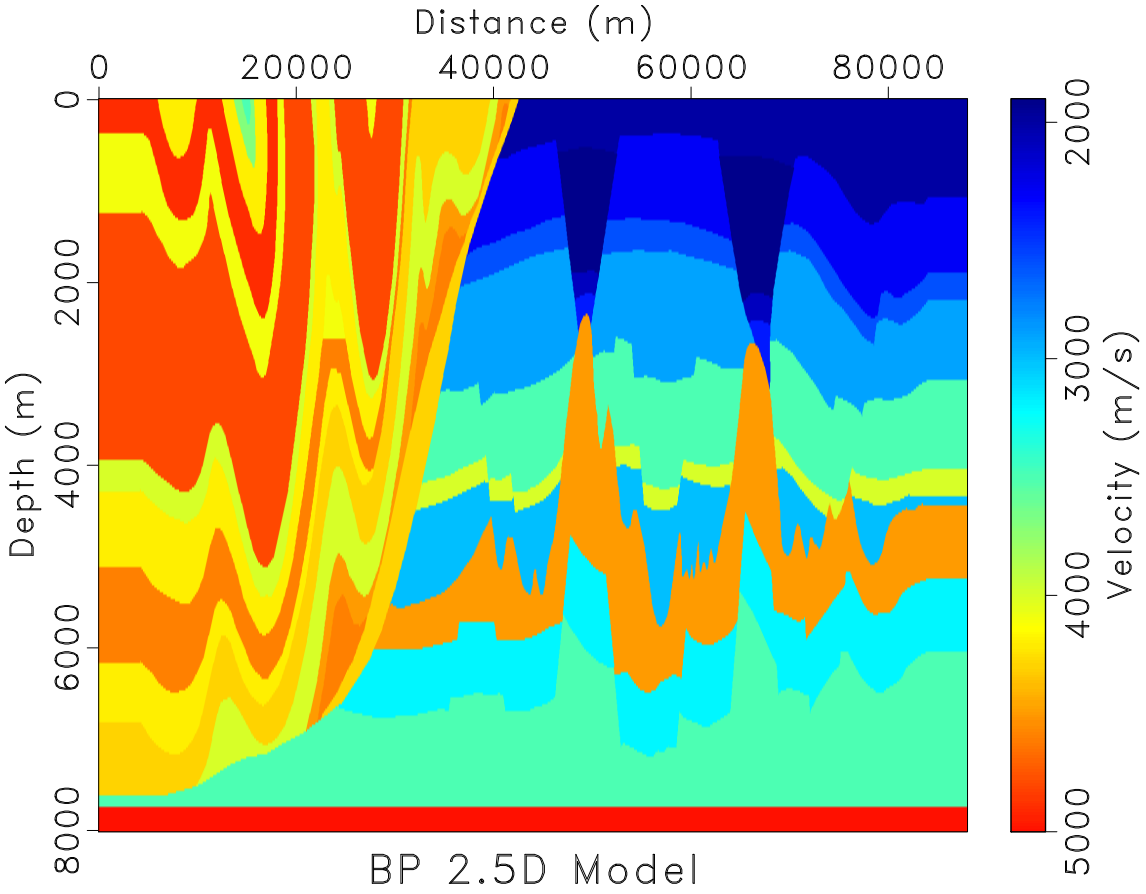

Figure 5.1: Velocity model (section from 2.5-D). chapter-rtm/twohalf modelth

Hz. The horizontal and vertical space grid sizes are 12.5 m and the time step is 1.2 ms. The shot interval is 50 m and the receiver interval is 25 m. Figure 5.2 shows the output image by 385 shots. Note that complicated structures are well imaged.

The second model shown in figure 5.3 is the Marmousi model created in 1988 by the Institut Français du Pétrole (IFP) in 1988. The geometry of this model is based on a profile through the North Quenguela trough in the Cuanza basin. The

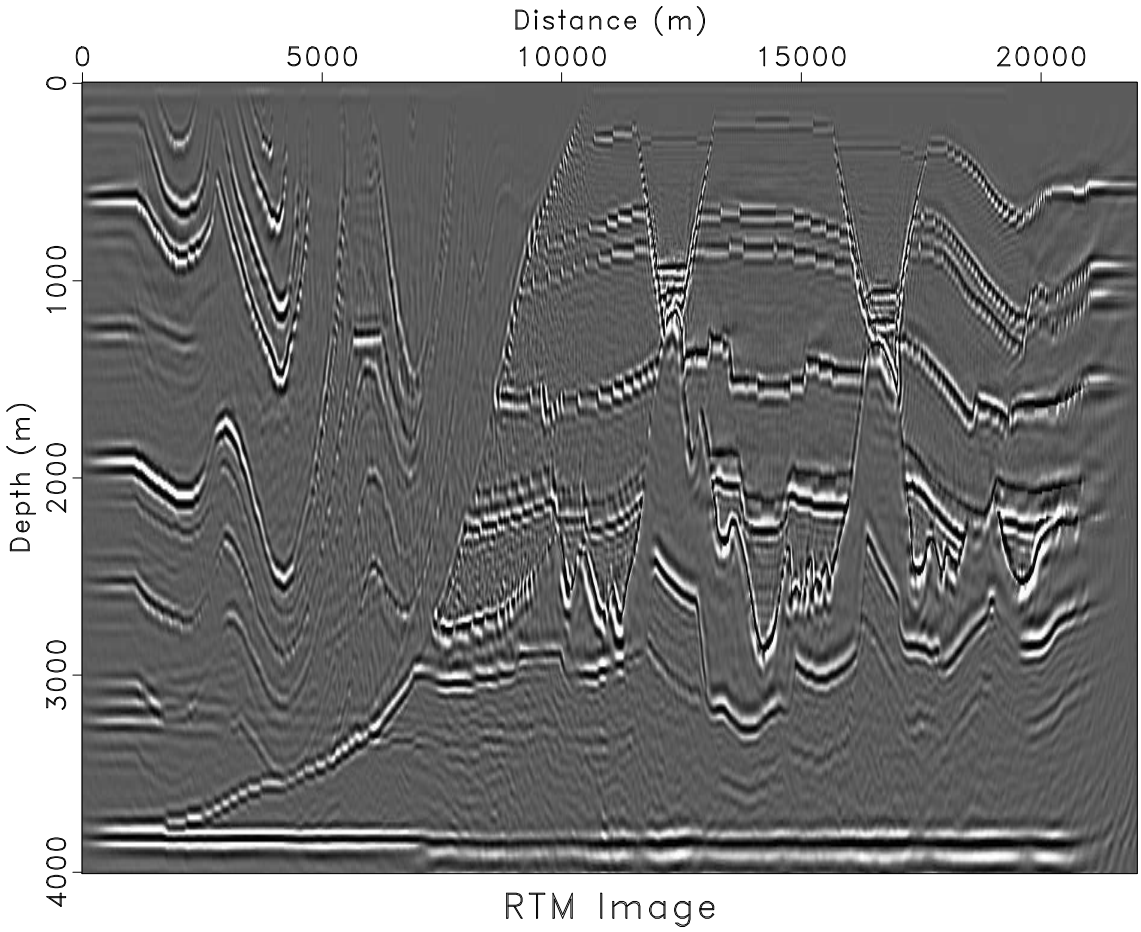

Figure 5.2: RTM image by Fourier finite-differences. chapter-rtm/twohalf rtmth

geometry and velocity model were created to produce complex seismic data which require advanced processing techniques to obtain a correct earth image (Versteeg, 1994). The Marmousi dataset was used for the workshop on practical aspects of seismic data inversion at the 52nd EAEG meeting in 1990. The maximum frequency is 60 Hz. The horizontal space grid size is 12.5 m and the vertical is 4 m and the time step is 0.4 ms. There are 240 shots, with an interval of 25 m and the receiver interval is also 25 m. Figure 5.4 displays the RTM image by FFD method, which provides detailed subsurface structure within the illumination range of shots.

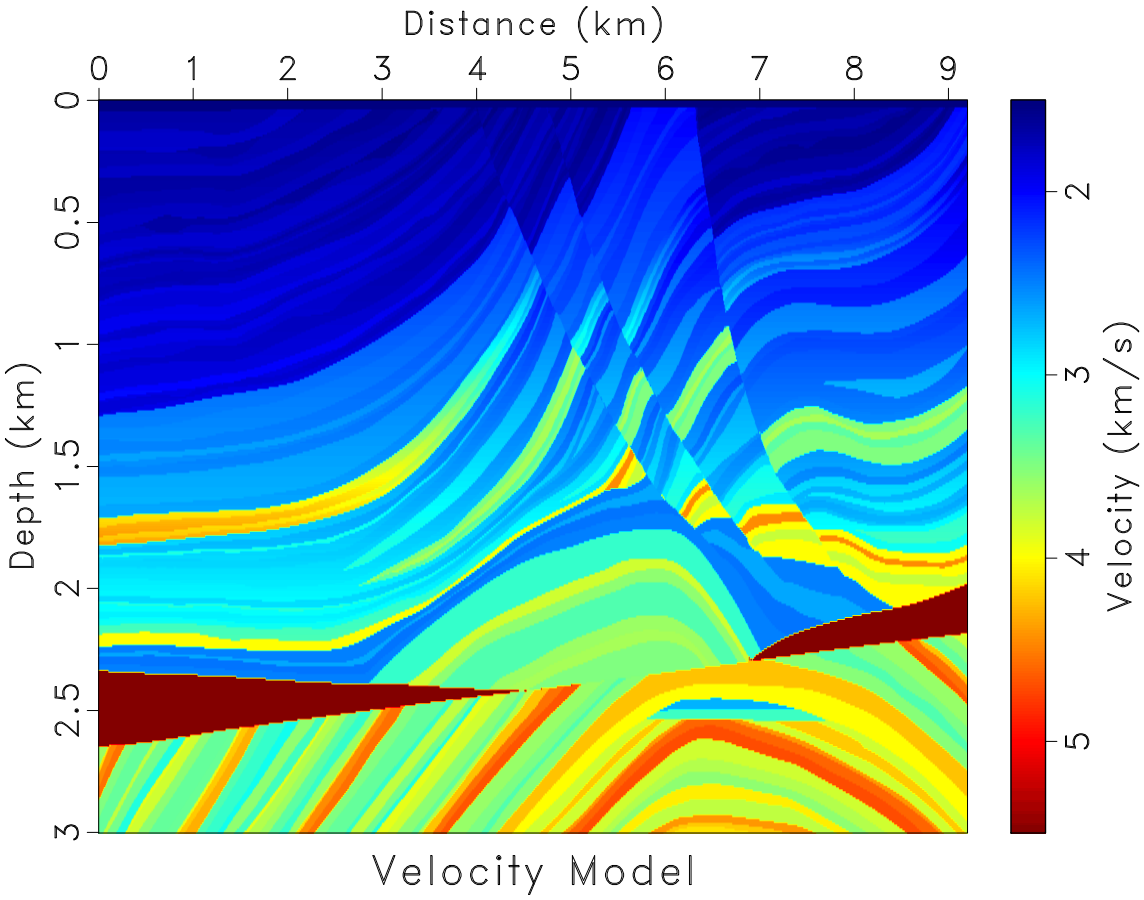

Figure 5.3: Marmousi velocity model. chapter-rtm/marmousi velmar

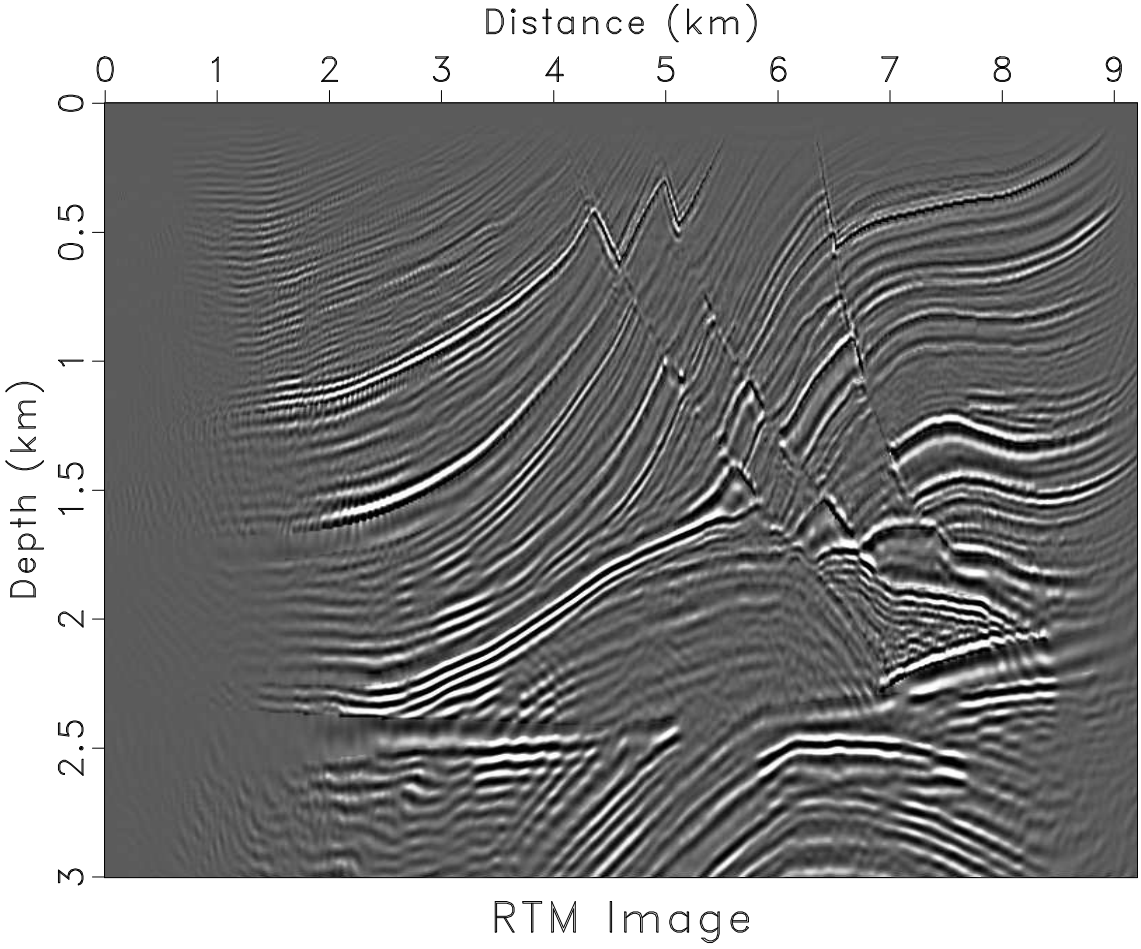

Figure 5.4: FFD RTM image for Marmousi model. chapter-rtm/marmousi rtmmar

The third example is the Sigsbee. It was one of the data sets released by The Subsalt Multiples Attenuation and Reduction Technology Joint Venture (SMAART JV) between September 2001 and November 2002. These synthetic data model the geologic setting found on the Sigsbee escarpment in the deep water Gulf of Mexico. Additional information may be found at `http://www.delphi.tudelft.nl/SMAART/`. Figure 5.5 displays the migration velocity model. The maximum frequency is 60 Hz. The shot interval is 45.72 m and the receiver interval is 22.86 m. The horizontal space grid size is 22.86 m and the depth grid size is 7.62 m. The time step is 1 ms. Figure 5.6 shows the corresponding FFD RTM result by 500 shots.

The third example is the 2004 BP benchmark model 5.7. This model was originally developed as a velocity-analysis benchmark dataset, in conjuction with the workshop "Estimation of Accurate Velocity Macro Models in Complex Structures" at the 2004 EAGE meeting in Paris, France (Billette and Brandsberg-Dahl, 2004). The maximum frequency is 60 Hz. The horizontal space grand vertical space grid sizes are both 12.5 m. The shot interval is 50 m and the receiver interval is 12.5 m. The time step is 1 ms. Figure 5.8 displays the corresponding FFD RTM image. Note that the inner and outer flanks of the salt body are clearly imaged.

Next model represents a cross section through the foothills of the Canadian rockies. It was created for the paper (Gray and Marfurt, 1995). This dataset was created at the Amoco Tulsa Research Lab in 1994 by Mike O'Brien as part of a project to study methods for attacking statics in land data. The geology of the model is completely invented, not based on any specific play. It contains many different types of near-surface geology, generally representing geology thought to be responsible for

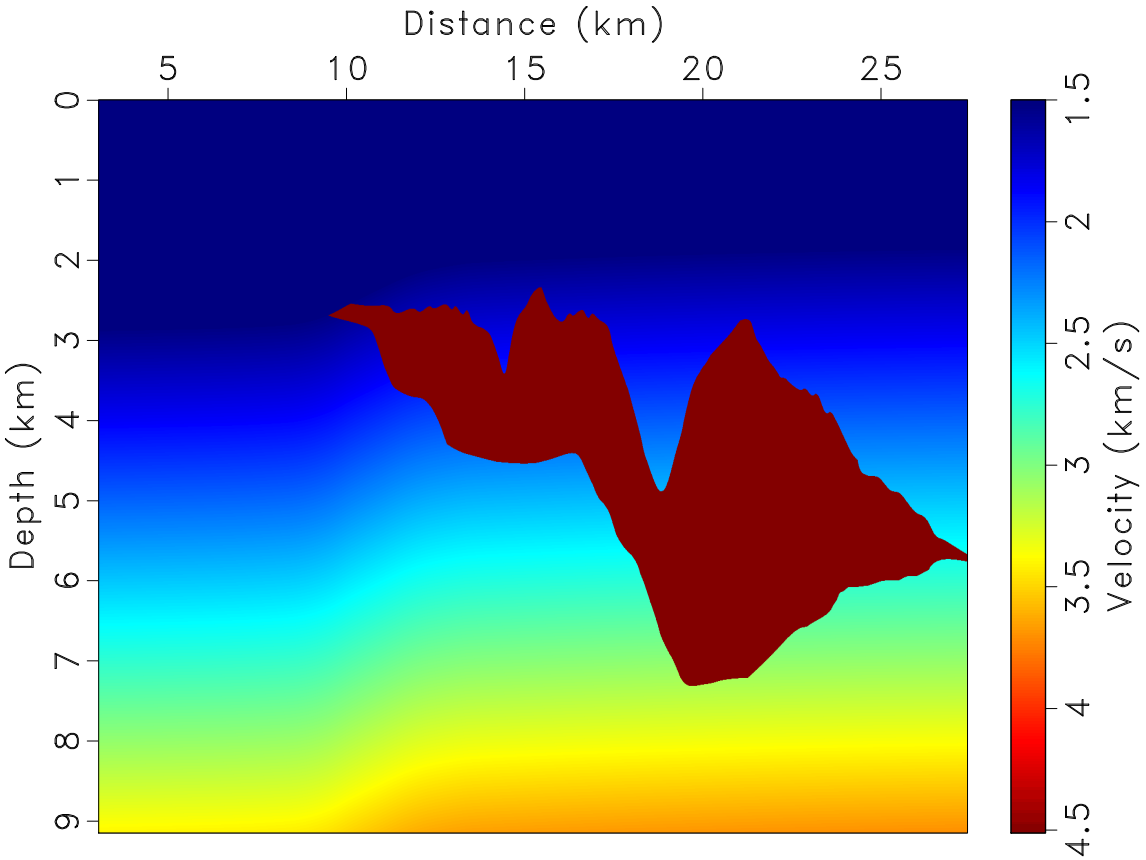

Figure 5.5: Sigsbee Velocity model. chapter-rtm/sigsbee velsig

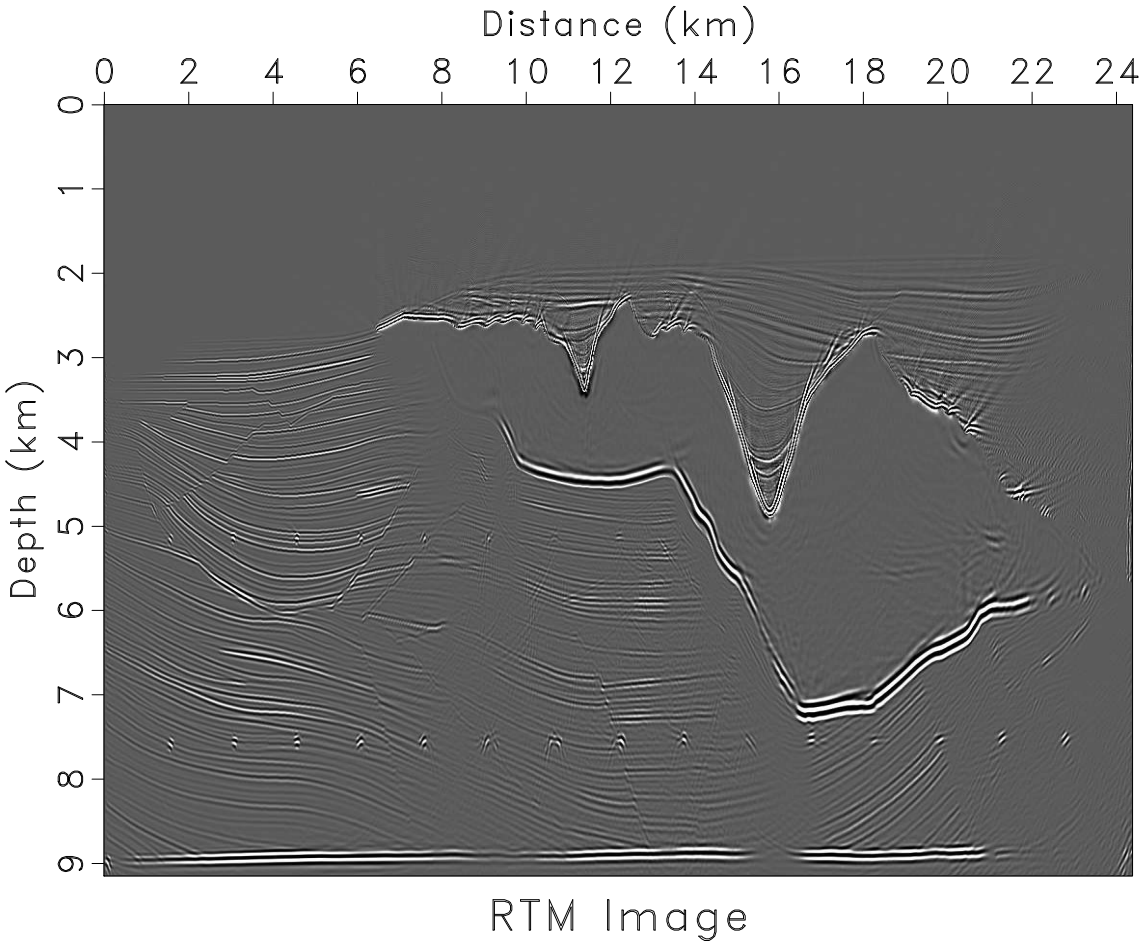

Figure 5.6: FFD RTM image for Sigsbee model. chapter-rtm/sigsbee rtmsig

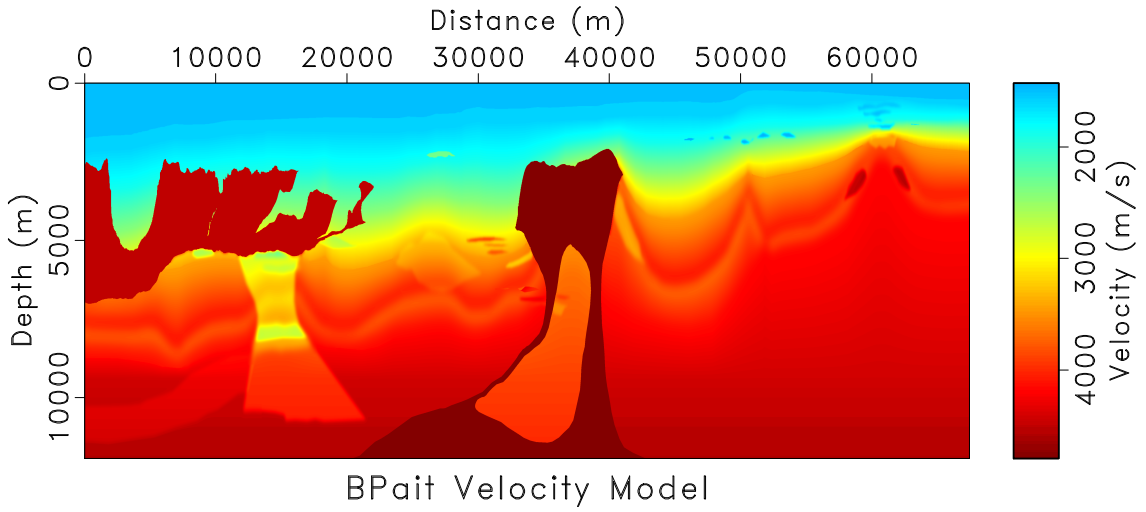

Figure 5.7: BP 2004 Benchmark velocity model. chapter-rtm/bprtm velbp

statics. The model is 2D, purely acoustic, with a constant density. The model was used in two internal Amoco reports (F94-G-0059 and F95-G-0033) but was never published externally by Amoco. The model was released to a few academic institutions in the late 1990's. It is being released again in 2008 `http://software.seg.org` by popular request, courtesy of BP and Joe Dellinger.

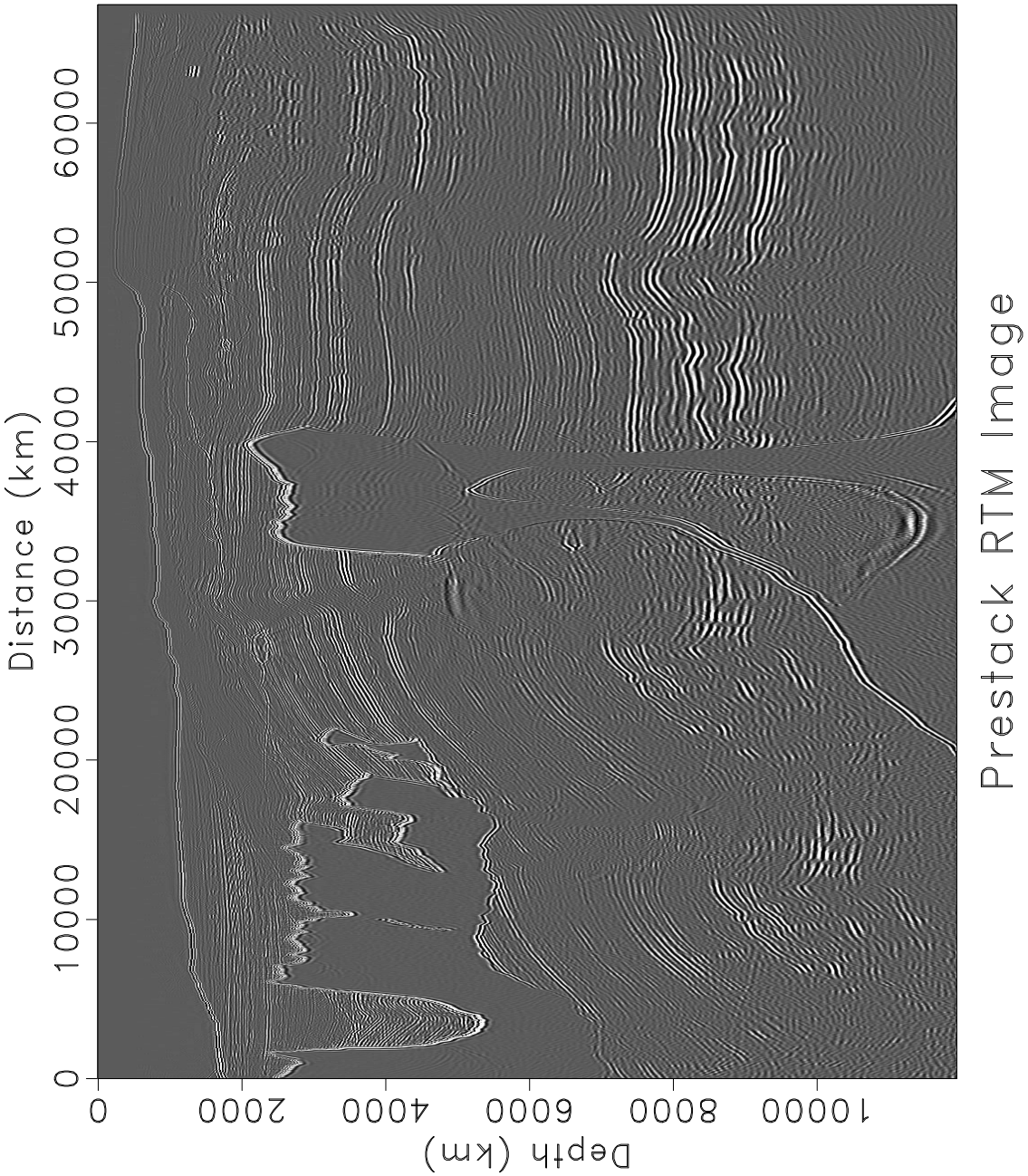

Figure 5.8: FFD RTM image for BP 2004 Benchmark model. chapter-rtm/bprtm rtmbp

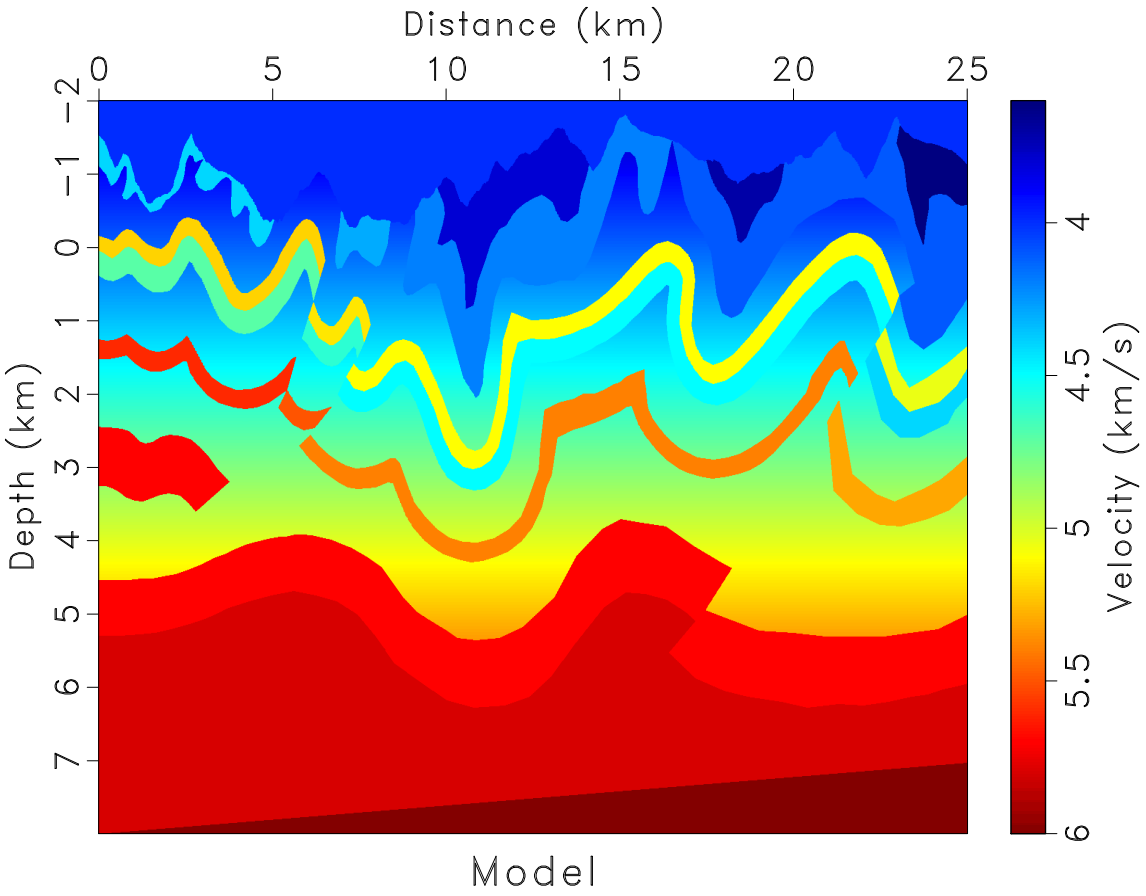

Figure 5.9: Velocity model. chapter-rtm/model94 velocity94

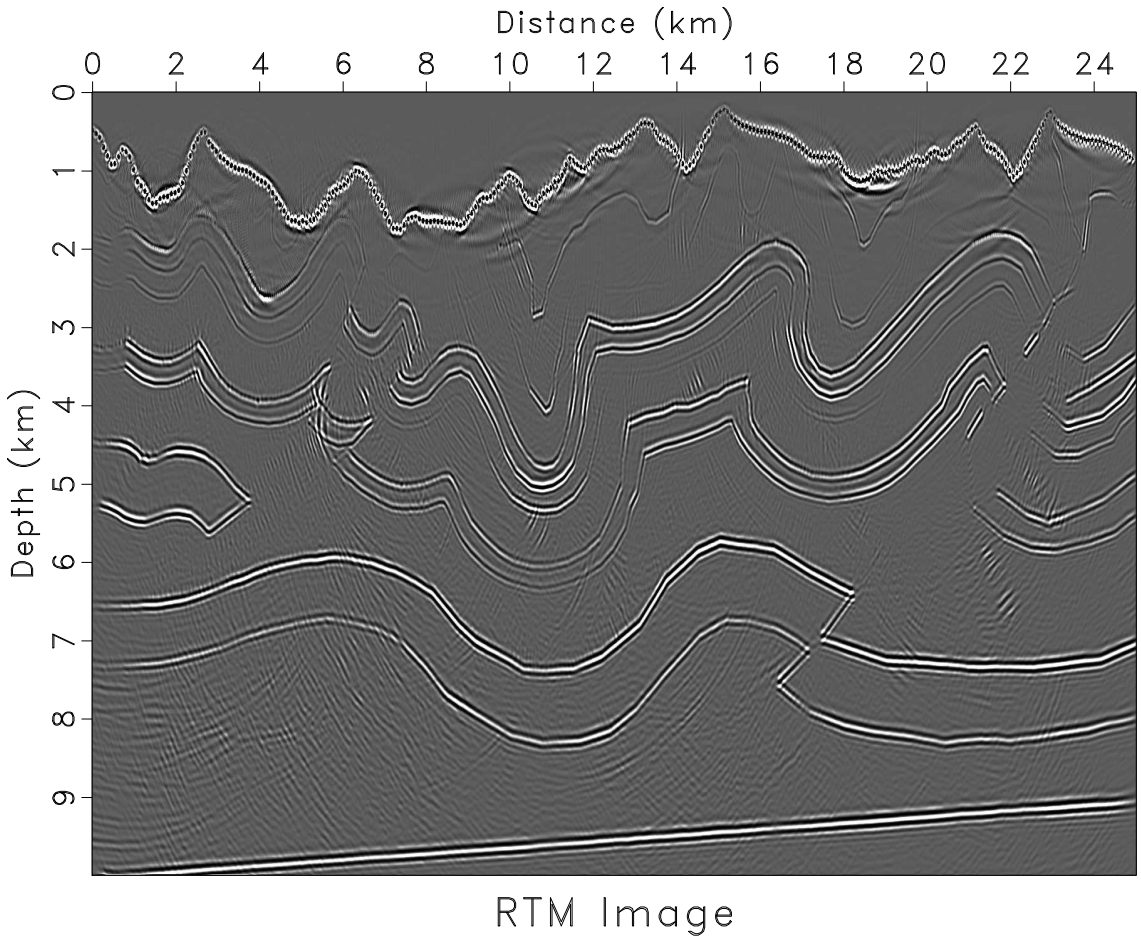

Figure 5.10: FFD RTM image. chapter-rtm/model94 ffdrtm94

The maximum frequency is 100 Hz. The shot interval is 90 m and the receiver interval is 15 m. The horizontal space grid size is 15 m and the depth grid size is 10 m. The time step is 1 ms. Figure 5.10 displays the corresponding FFD RTM image. Note that the image clearly reflects the topography of the model.

Next example is a VTI model generated at Hess Corporation. Figure 5.11,5.12 and 5.13 show the input VTI model parameters. The maximum frequency is 50 Hz. There are 720 shots, with 30.48 m interval and the receiver interval is 12.192 m. The horizontal and vertical space grid sizes are both 6.096 m. The time step is 1 ms. Figure 5.14 displays a VTI RTM image by the propsed FFD method. Note that the subsalt reservoirs are well imaged to the correct locations, which are attached to the right edge of the salt body.

Figure 5.16 displays a TTI RTM image by the propsed TTI FFD method. One can clearly observe anticlines, salt body flanks, and faults from the image. Figure 5.15 show the input TTI model parameters. This dataset was released by BP as the 2007 BP Anisotropic Velocity-analysis Benchmark dataset (Shah, 2007). The maximum frequency is 50 Hz. There are 1574 shots, with 50 m interval and the receiver interval is 12.5 m. The horizontal and vertical space grid sizes are both 6.25 m. The time step is 1 ms.

Finally, I apply FFD RTM to a real dataset provided by BP. It is a 2D line selected from a 3D survey in the Western Gulf of Mexico Deep Water. There are 236 shots, with 150 m interval and the receiver interval is 25 m. The input parameters

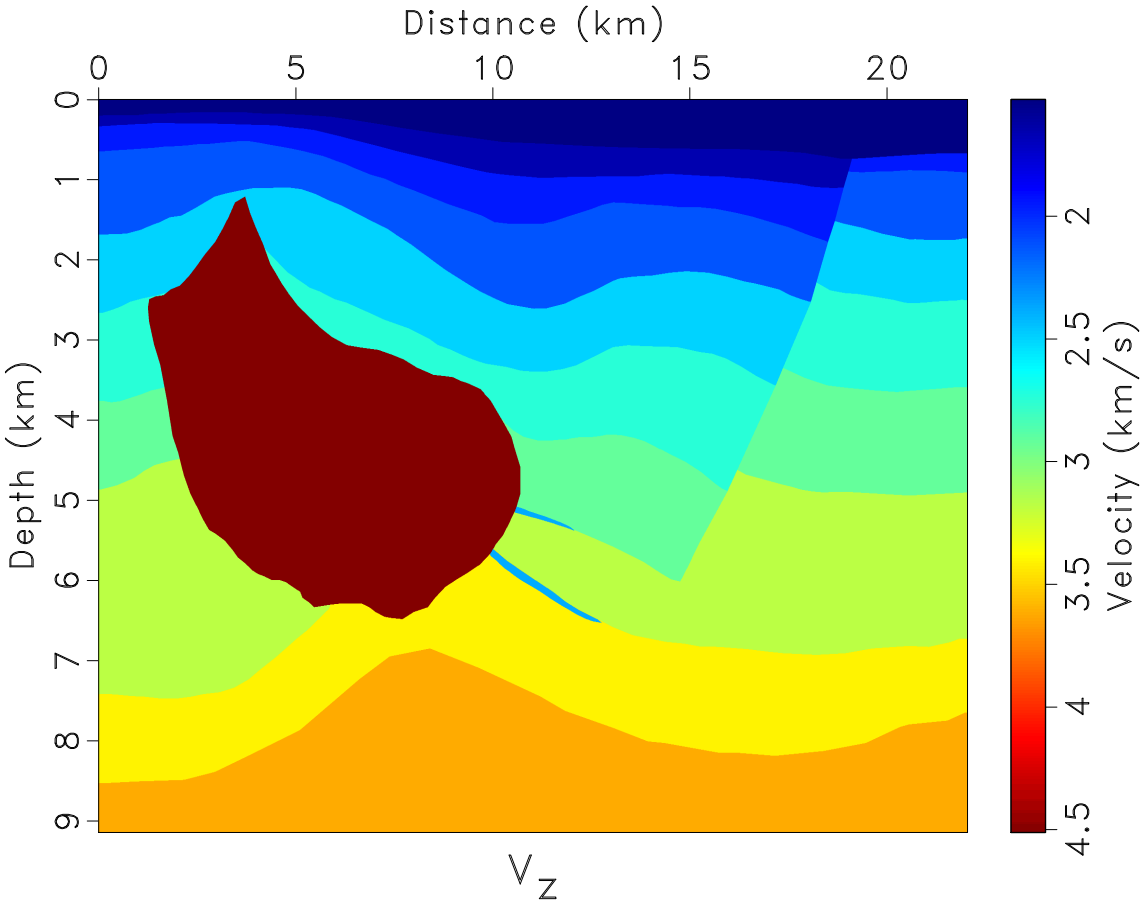

Figure 5.11: Vertical velocity. chapter-rtm/hessvti vph

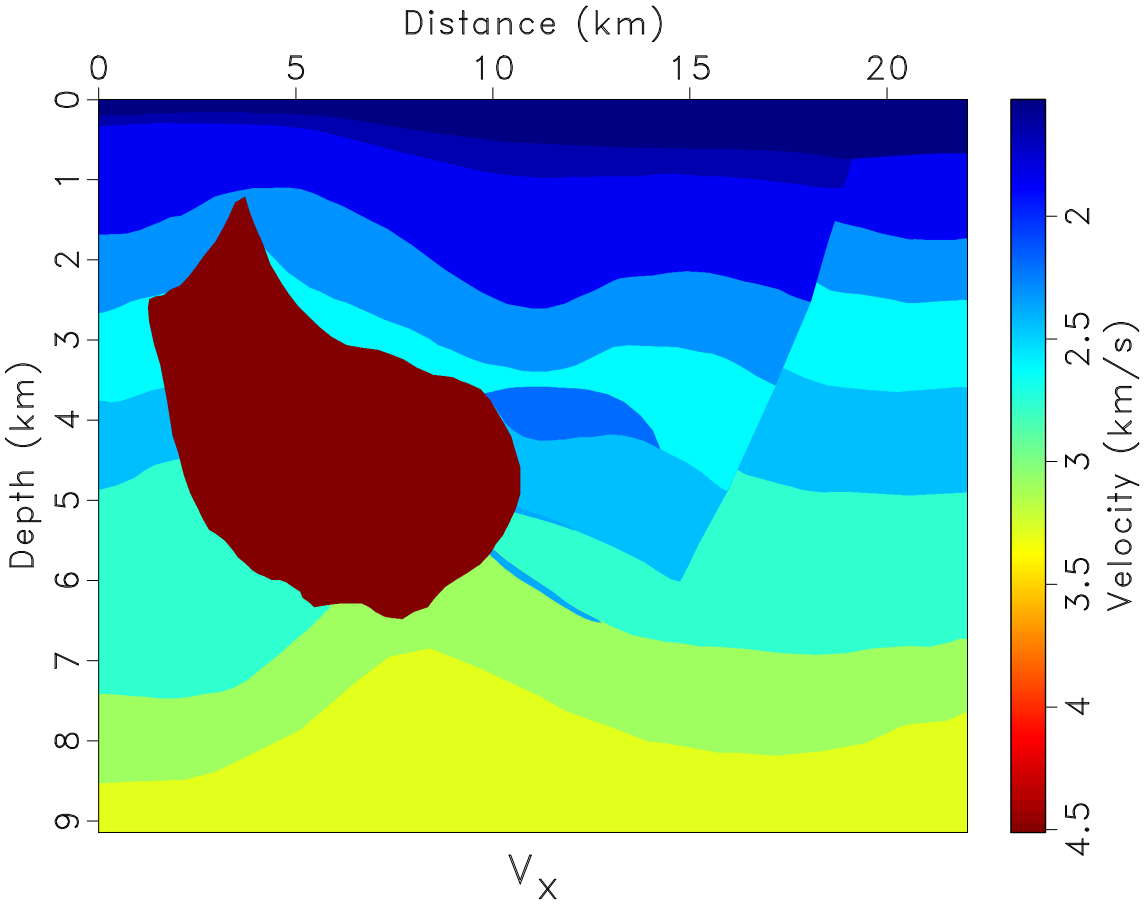

Figure 5.12: Horizontal velocity. chapter-rtm/hessvti vxh

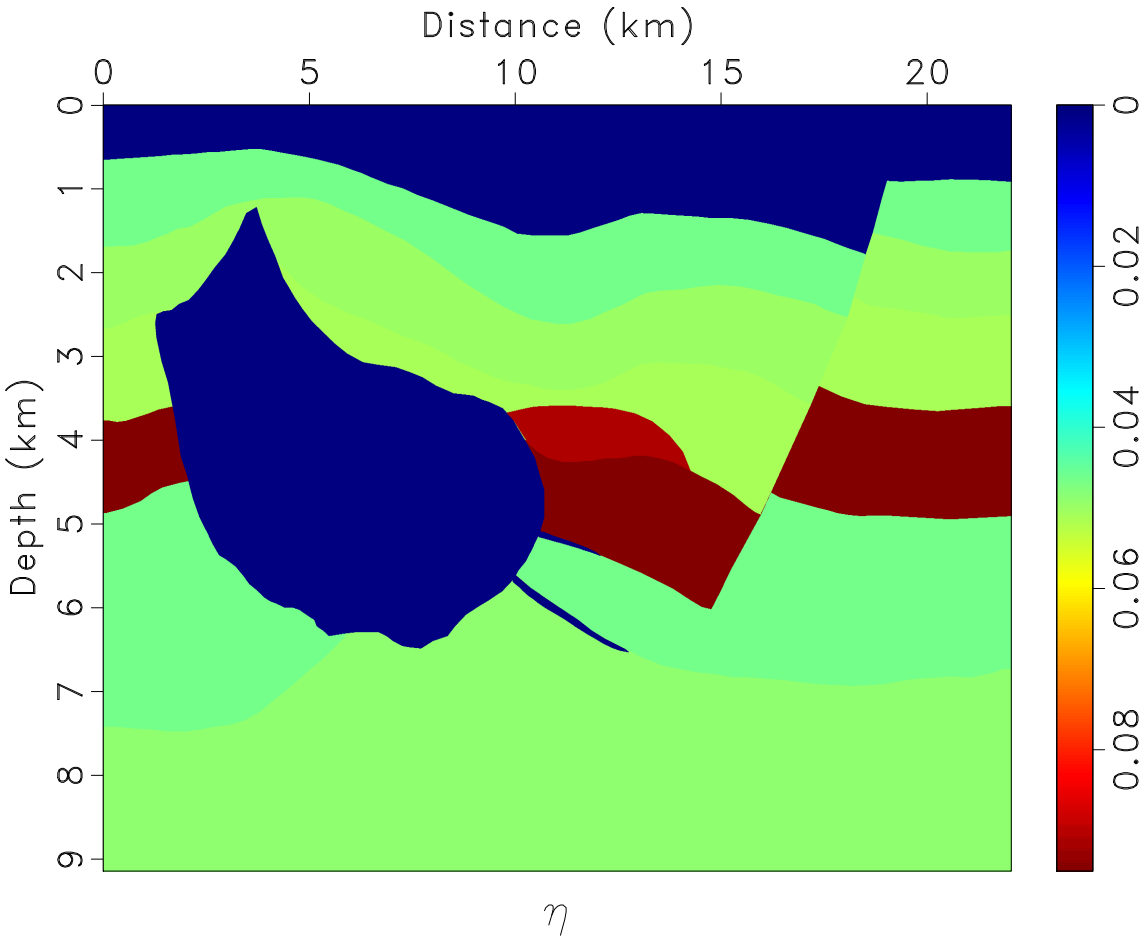

Figure 5.13: The anisotropic η parameter. chapter-rtm/hessvti etah

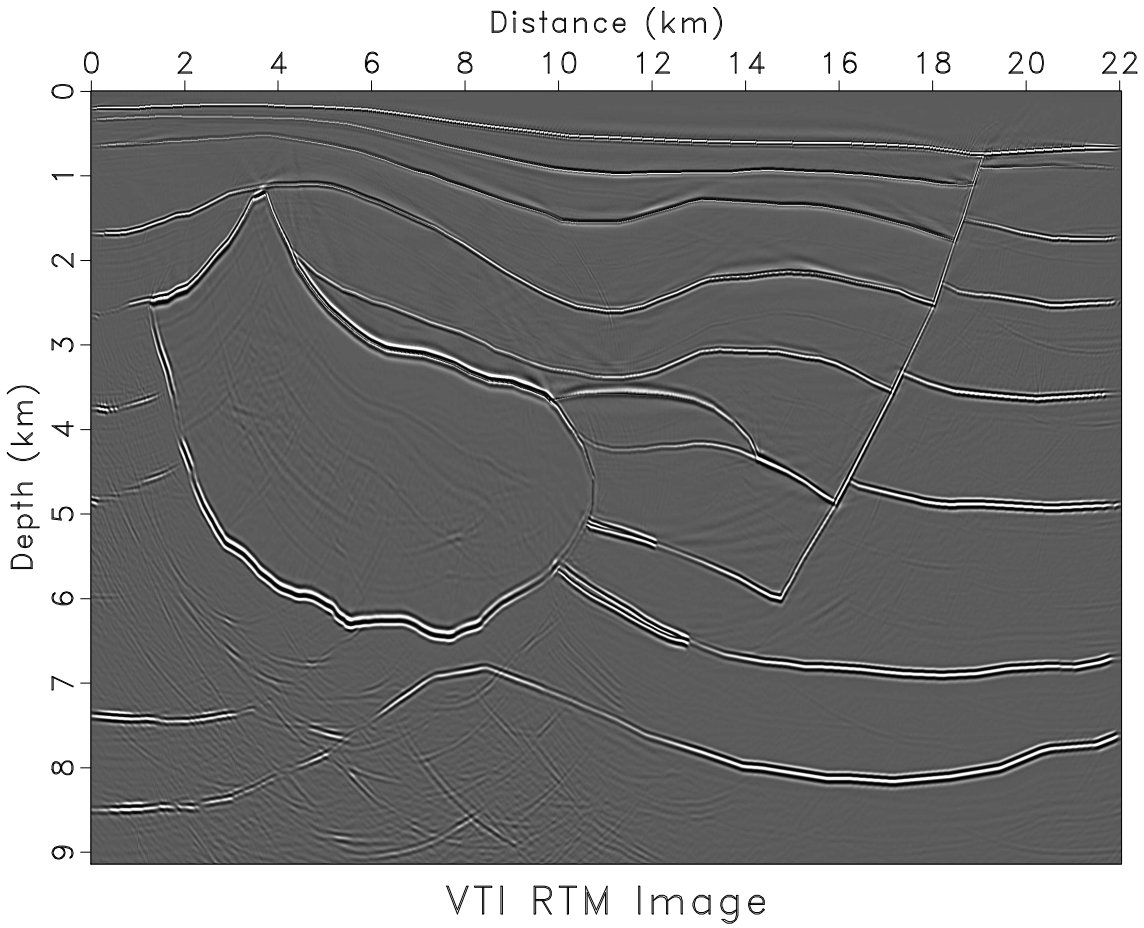

Figure 5.14: VTI FFD RTM image. chapter-rtm/hessvti hvtiffdrtm

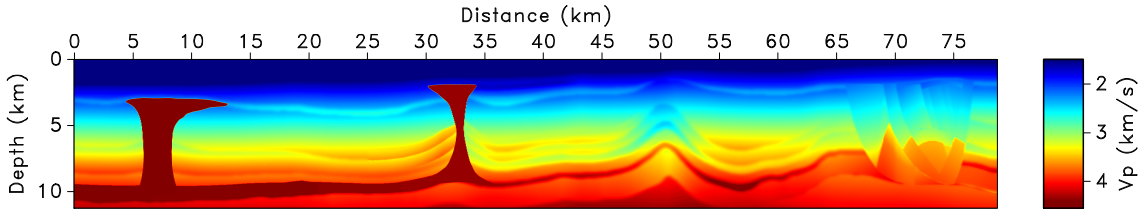

(a)

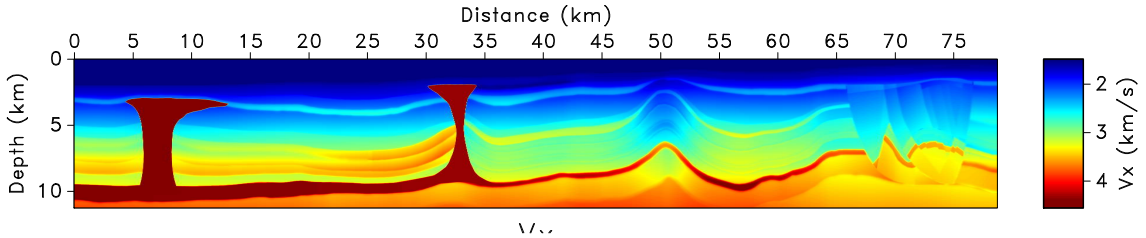

(b)

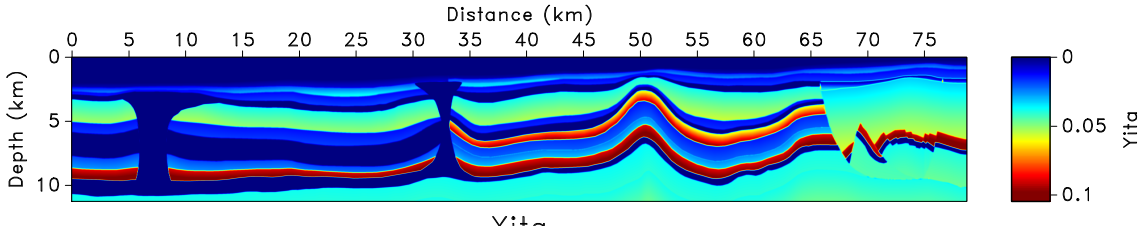

(c)

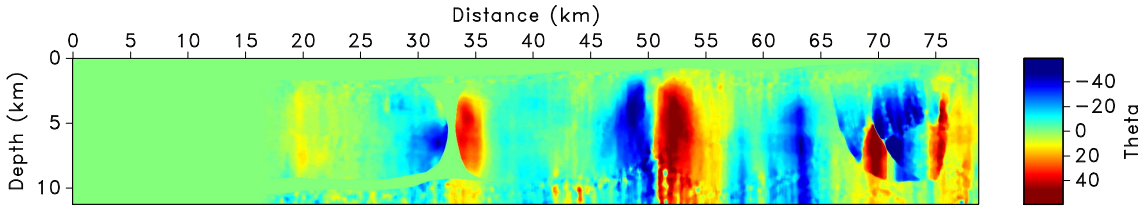

(d)

Figure 5.15: The 2D BP TTI model. a: v_z. b: v_x. c: η. d:θ. chapter-rtm/bptti vp,vx,yita,theta

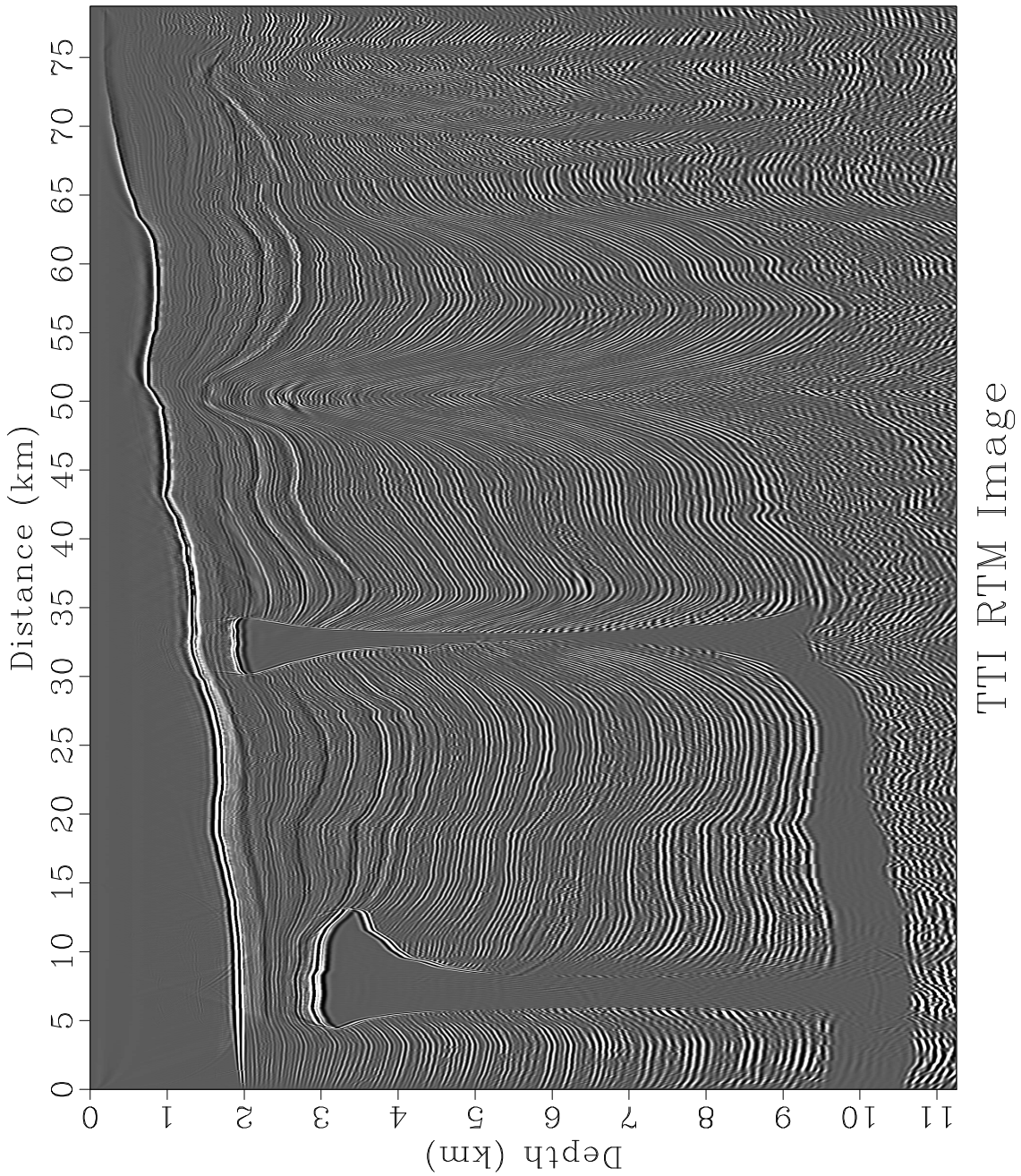

Figure 5.16: TTI RTM image of the 2D BP TTI model, shown in Figure 5.15. chapter-rtm/bptti ttimg

are v_z (Figure 5.17), v_x (Figure 5.18), η (Figure 5.19), and θ (Figure 5.20). The dip angle is converted from 3D angle parameters, which include both tilt and azimuth parameters. Figure 5.20 displays some apparent artifacts coming from the inaccuracy of the original 3D parameters. The horizontal and vertical space grid sizes are both 12.5 m. The maximum frequency is 23 Hz. The time step is 2 ms. Figure 5.21 displays the output TTI RTM image by TTI FFD method. Although adopting the challenging dip parameters (Figure 5.20) as input, TTI FFD is still stable in this test. It indicates two salt bodies located in the area. From the figure, one can observe the sedimentary layers. The target is located in the subsalt sediments adjacent to the left salt body.

CONCLUSIONS

In this chapter, I present examples of the application of FFD to RTM in isotropic, VTI and TTI models. Both synthetic and real data examples illustrate that the FFD method can be used in reverse-time migration to enhance its accuracy and stability. All examples are reproducible using Madagascar software `http://www.ahay.org`.

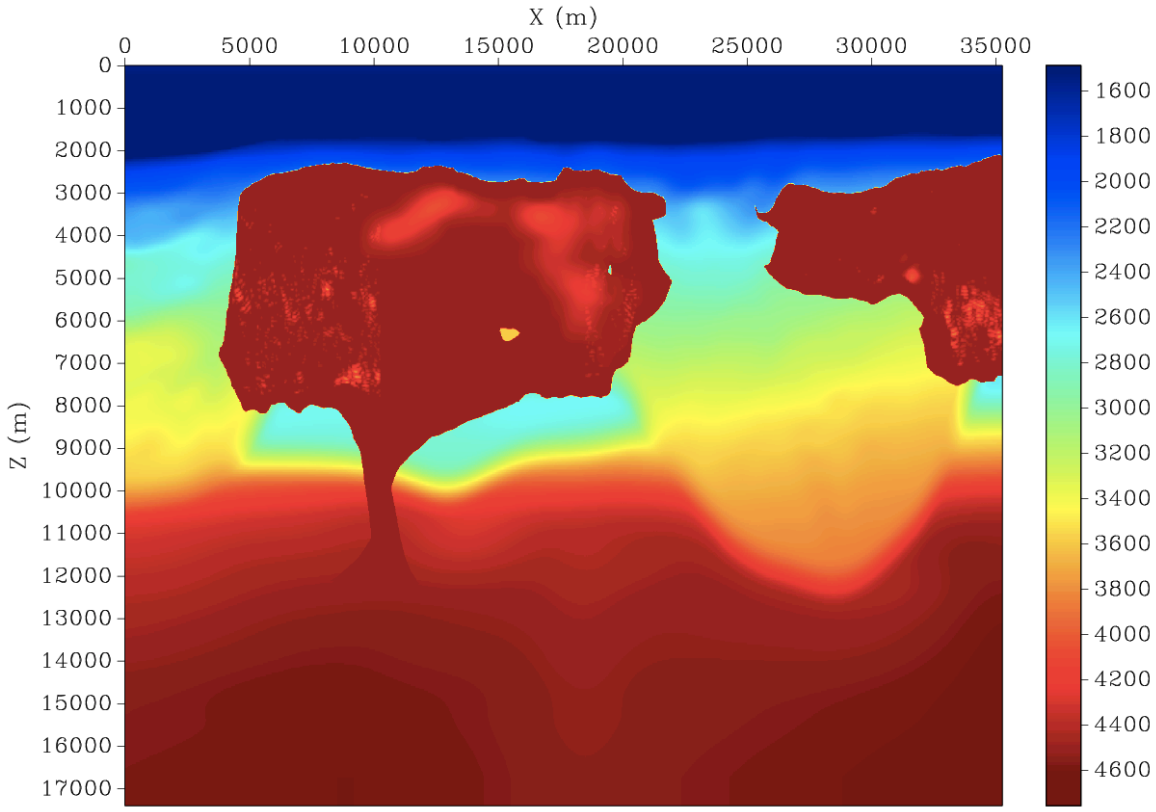

Figure 5.17: 2D Western Gulf of Mexico Deep Water TTI model: v_z (m/s). chapter-rtm/gom v0n2

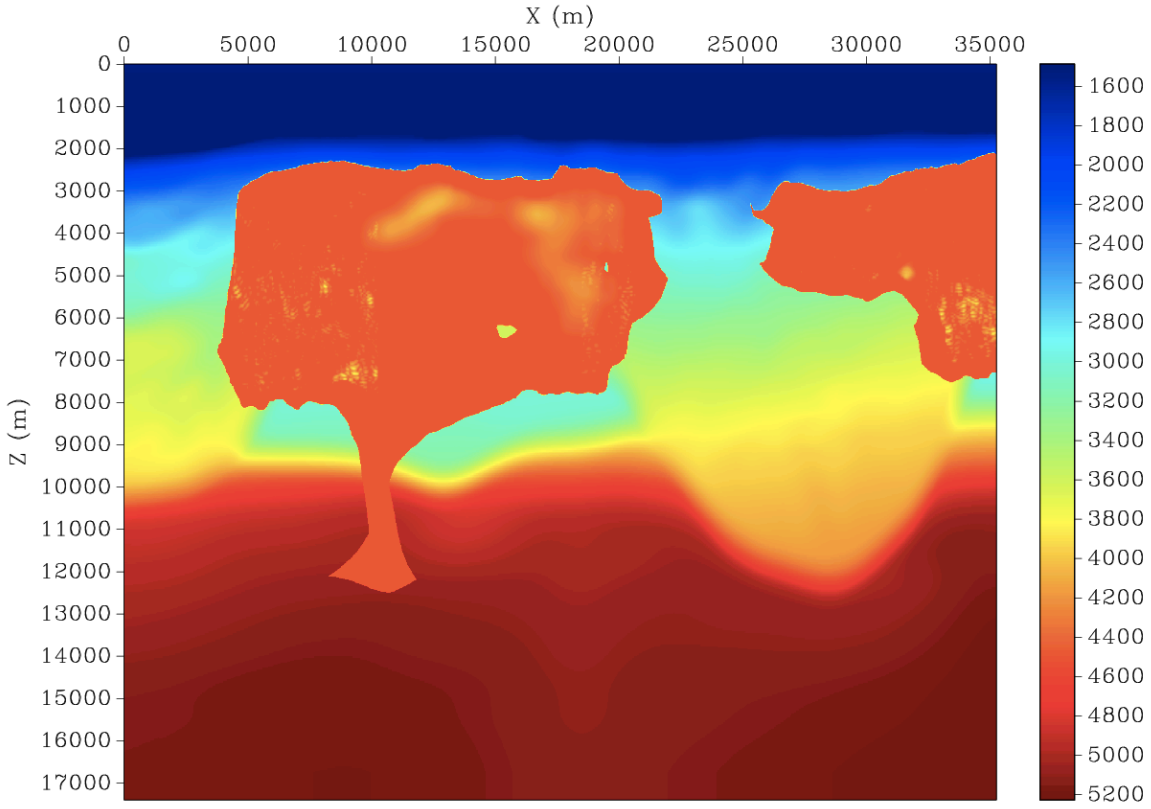

Figure 5.18: 2D Western Gulf of Mexico Deep Water TTI model: v_x (m/s). chapter-rtm/gom vxn2

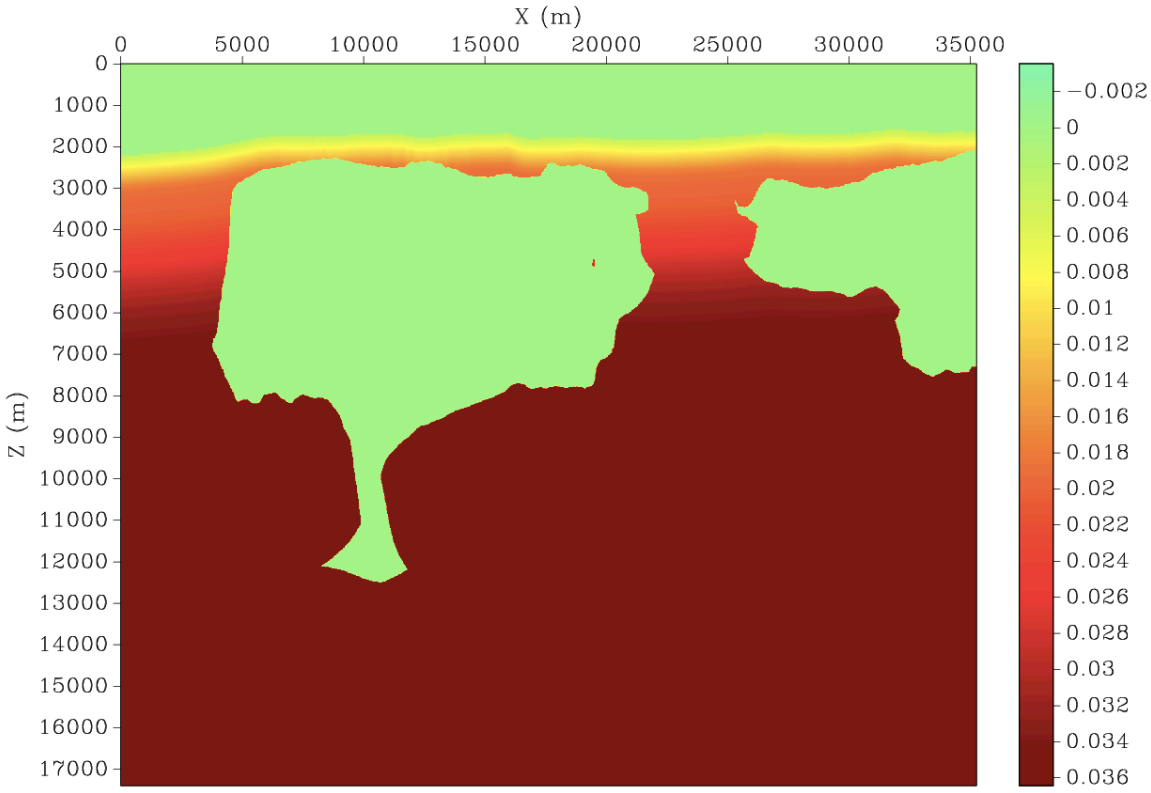

Figure 5.19: 2D Western Gulf of Mexico Deep Water TTI model: η. chapter-rtm/gom yitan

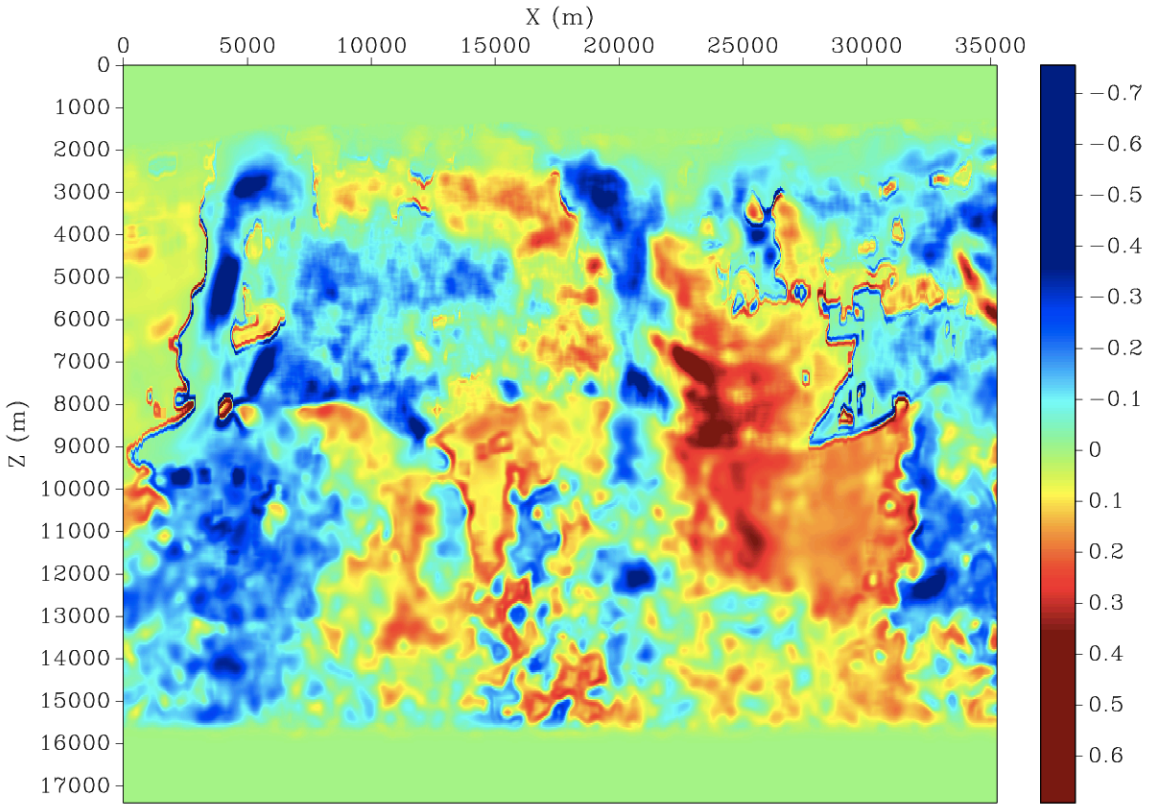

Figure 5.20: 2D Western Gulf of Mexico Deep Water TTI model: θ. chapter-rtm/gom setan2

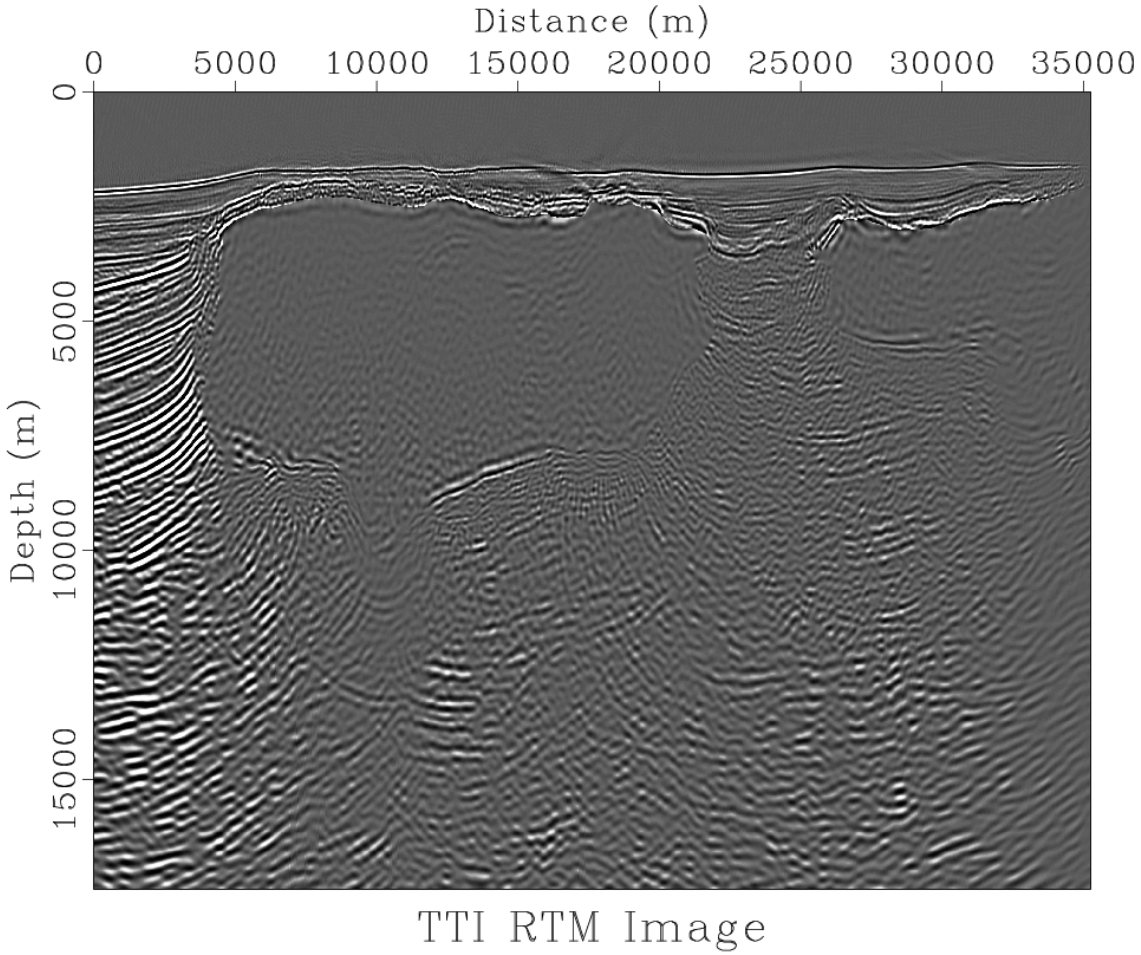

Figure 5.21: 2D TTI RTM image for the Western Gulf of Mexico Deep Water. chapter-rtm/gom imgtti

Chapter 6

Conclusions

Summary

Nowadays, subsalt oil and gas exploration is drawing more and more attention from the hydrocarbon industry. Accurate and efficient numerical wave propagation in variable velocity media is crucial for seismic modeling and seismic migration, particularly for reverse-time migration. In sedimentary rocks, anisotropic phenomena are often observed as a result of layering lithification, which is described as transversely isotropic (TI). Fractures in rocks caused by stresses in the crust may induce orthorhombic anisotropy. Tectonic movement of the crust may rotate the rocks and tilt the natural vertical orientation of the symmetry axis (VTI), causing a tilted TI (TTI) anisotropy. Wavefields in anisotropic media are well described by the anisotropic elastic-wave equation. However, in practice, seismologists often have difficulty in working with shear waves and prefer to deal with scalar wavefields.

Conventional P-wave modeling may contain shear-wave numerical artifacts in the simulated wavefield. Those artifacts as well as sharp changes in symmetry-axis tilting may introduce severe numerical dispersion and instability in modeling. In recent years, thanks to advances in supercomputer technology, spectral methods have become feasible for large-scale problems. A number of spectral methods are proposed to provide solutions which can completely avoid the shear-wave artifacts.

Different from conventional pseudo-spectral methods, these methods approximate the space-wavenumber mixed-domain propagation matrix instead of a Laplacian filter. In heterogeneous media, these space-wavenumber mixed-domain approximation methods may cost several Fourier transforms per time step.

In order to achieve a better cost-accuracy trade-off, I have developed three novel methods for seismic wave extrapolation in heterogeneous media. The first method involves cascading a Fourier Transform operator and a finite difference operator to form a chain operator: Fourier Finite Differences (FFD). FFD method can be as accurate as the parameter interpolation approach employed by Etgen and Brandsberg-Dahl (2009) but at a cost of only one Fast Fourier Transform (FFT) and inverse Fast Fourier Transform (IFFT) operation. In order to extend the two-way FFD method from constant-density to variable-density media, I have adopted the FFD operator for coupled first-order wave-propagation equations using staggered spatial and temporal grids. This novel FFD operator may prove useful in applications to quality control that require high accuracy. The second method is presented as a novel FD scheme: Lowrank Finite Differences (LFD), which is based on the lowrank approximation of the mixed-domain space-wavenumber propagator. The derived FD scheme matches the spectral response in the mixed space-wavenumber domain for a wide range of spatial wavenumbers. As a result, this technique promises higher accuracy than that of the conventional, explicit FD method. Finally, I propose lowrank FFD (LFFD) method, replacing the original 4th-order FD operator based on Taylor's expansion around zero wavenumber, in FFD with an 8th-order LFD operator to reduce dispersion in the TTI case.

Discussion

All of the three methods start from the mixed-domain operator and try to decrease the computional cost in three different ways. The FFD method is more efficient than the velocity interpolation method. This advantage is more apparent in the anisotropic case: it costs only one forward and inverse Fast Fourier Transform and there is no need for several interpolations for different parameters with the corresponding computational burden of several FFTs and IFFTs. The LFD method provides novel FD schemes with adapted coefficients. It is free of FFTs and compared to spectral methods, it may be more suitable for parallel computing on distributed multi-processors especially when partitioning is necessary for the model domain. As an accurate FD method, I also propose to apply it to the TTI FFD method to replace the original 4th-order FD operator. As a result, the new Lowrank FFD (LFFD) operator effectively reduces the dispersion and is more accurate in the TTI case.

The lowrank approximation method is more accurate than these three methods. However, the cost is higher: it costs a small number of FFT operations per time step, which corresponds to the approximation rank. However, its advantage is a direct control on the accuracy-efficiency trade-off by controlling the rank of the approximation and the corresponding approximation error. The lowrank approximation method is a more general method to handle complicated mixed-domain operators. I demonstrated this point with pseudo-acoustic orthorhombic modeling by lowrank method. The successful application of lowrank approximation to orthorhombic modeling implies that it should be possible to apply LFD or LFFD method to pseudo-acoustic orthorhombic modeling to reduce the computational cost.

All of the three methods proposed in this dissertation can be applied to both isotropic and anisotropic media. In TTI media, there is no coupling of qP-wave and qSV-wave by these methods. Furthermore, there are no particular constraints on anisotropic parameters required for stability. Results from synthetic experiments illustrate the stability of the proposed methods in complicated velocity models. Although I present only 2-D examples, the proposed methods can be further optimized and implemented in 3-D case. These methods can be used in seismic imaging by reverse-time migration to enhance its accuracy and stability.

Bibliography

Alkhalifah, T., 1998, Acoustic approximations for processing in transversely isotropic media: Geophysics, **63**, 623–631.

———, 2000, An acoustic wave equation for anisotropic media: Geophysics, **65**, 1239–1250.

———, 2003, An acoustic wave equation for orthorhombic anisotropy: Geophysics, **68**, 1169–1172.

Alkhalifah, T., and I. Tsvankin, 1995, Velocity analysis for transversely isotropic media: Geophysics, **60**, 1550–1566.

Baysal, E., D. D. Kosloff, and J. W. C. Sherwood, 1983, Reverse time migration: Geophysics, **48**, 1514–1524.

———, 1984, A two-way nonreflecting wave equation: Geophysics, **49**, 132–141.

Billette, F. J., and S. Brandsberg-Dahl, 2004, The 2004 BP velocity benchmark: 67th Annual EAGE Meeting, EAGE, Expanded Abstracts, B305.

Biondi, B., 2006, 3-D seismic imaging: Soc. Expl. Geophys.

Biondi, B., and G. Shan, 2002, Prestack imaging of overturned reflection by reverse time migration: 72nd Ann. Internat. Mtg., Soc. Expl. Geophys., 1284–1287.

Bleistein, N., Y. Zhang, S. Xu, G. Zhang, and S. H. Gray, 2005, Migration/inversion: think image point coordinates, process in acquisition surface coordinates: Inverse Problems, **21**, 1715–1744.

Carroll, J., 2011, Exxon Finds Biggest Oil Field in Gulf of Mexico Since 1999: http://www.bloomberg.com/news/2011-06-08/exxon-mobil-reports-3-discoveries-in-gulf-of-mexico.html.

Cerjan, C., D. Kosloff, R. Kosloff, and M. Reshef, 1985, A nonreflecting boundary condition for discrete acoustic and elastic wave equations: Geophysics, **50**, 705–708.

Chapman, C., 2004, Fundamentals of seismic wave propagation: Cambridge University Press.

Chattopadhyay, S., and G. A. McMechan, 2008, Imaging conditions for prestack reverse-time migration: Geophysics, **73**, S81–S89.

Cheng, J., and W. Kang, 2012, Propagating pure wave modes in 3D general anisotropic media, Part I: P-wave propagator: 82nd Ann. Internat. Mtg., Soc. Expl. Geophys., Accepted.

Chevron, 2006, Chevron Announces Record Setting Well Test at Jack: http://www.chevron.com/news/press/Release/?id=2006-09-05.

Chu, C., B. K. Macy, and P. D. Anno, 2011, Approximation of pure acoustic seismic wave propagation in tti media: Geophysics, **76**, WB97–WB107.

Chu, C., and P. Stoffa, 2008, A pseudospectral-finite difference hybrid approach for large-scale seismic modeling and RTM on parallel computers, *in* 78th Ann. Internat. Mtg: Soc. of Expl. Geophys., 2087–2091.

Chu, C., and P. L. Stoffa, 2011, Application of normalized pseudo-Laplacian to elastic wave modeling on staggered grids: Geophysics, **76**, T113–T121.

Claerbout, J. F., 1985, Imaging the earth's interior: Blackwell Scientific Publications.

Claerbout, J. F., and S. M. Doherty, 1970, Coarse grid calculations of waves in inhomogeneous media with application to delineation of complicated seismic structure: Geophysics, **35**, 407–418.

———, 1972, Downward continuation of moveout-corrected seismograms: Geophysics, **37**, 741–768.

Crawley, S., S. Brandsberg-Dahl, and J. McClean, 2010, 3d TTI RTM using the

pseudo-analytic method: 80th Ann. Internat. Mtg., Soc. Expl. Geophys., 3216–3220.

Dablain, M. A., 1986, The application of high-order differencing to the scalar wave equation: Geophysics, **51**, 54–66.

Dellinger, J. A., S. H. Gray, G. E. Murphy, and J. T. Etgen, 2000, Efficient 2.5-D true-amplitude migration: Geophysics, **65**, 943–950.

Du, X., R. P. Fletcher, and P. J. Fowler, 2010, Pure P-wave propagators versus pseudo-acoustic propagators for RTM in VTI meida: 72nd Annual EAGE Meeting, EAGE, Expanded Abstracts, Accepted.

Duveneck, E., and P. M. Bakker, 2011, Stable P-wave modeling for reverse-time migration in tilted TI media: Geophysics, **76**, S65–S75.

Duveneck, E., P. Milcik, P. M. Bakker, and C. Perkins, 2008, Acoustic VTI wave equations and their application for anisotropic reverse-time migration: 78th Ann. Internat. Mtg., Soc. Expl. Geophys., 2186–2190.

Engquist, B., and L. Ying, 2007, Fast directional multilevel algorithms for oscillatory kernels: SIAM J. Sci. Comput., **29**, 1710–1737.

———, 2009, A fast directional algorithm for high frequency acoustic scattering in two dimensions: Commun. Math. Sci., **7**, 327–345.

Etgen, J., 1986, Prestack reverse time migration of shot profiles, *in* SEP-50: Stanford Exploration Project, 151–170.

———, 1989, Accurate wave equation modeling, *in* SEP-60: Stanford Exploration Project, 131–148.

Etgen, J., and S. Brandsberg-Dahl, 2009, The pseudo-analytical method: application of pseudo-Laplacians to acoustic and acoustic anisotropic wave propagation: 79nd Annual International Meeting, SEG, Expanded Abstracts, 2552–2556.

Etgen, J., S. H. Gray, and Y. Zhang, 2009, An overview of depth imaging in exploration geophysics: Geophysics, **74**, WCA5–WCA17.

Etgen, J., and C. Regone, 1998, Strike shooting, dip shooting, widepatch shooting - Does prestack depth migration care? A model study.: 68th Ann. Internat. Mtg, Soc. of Expl. Geophys., 66–69.

Farmer, P. A., I. F. Jones, H. Zhou, R. I. Bloor, and M. C. Goodwin, 2006, Application of reverse time migration to complex imaging problems: First Break, **24**, 65–73.

Finkelstein, B., and R. Kastner, 2007, Finite difference time domain dispersion reduction schemes: Journal of Computational Physics, **221**, 422–438.

Fletcher, R. P., X. Du, and P. J. Fowler, 2009, Reverse time migration in tilted transversely isotropic (TTI) media: Geophysics, **74**, WCA179–WCA187.

Fomel, S., 2004, On anelliptic approximations for qP velocities in VTI media: Geophysical Prospecting, **52**, 247–259.

Fomel, S., L. Ying, and X. Song, 2010, Seismic wave extrapolation using a lowrank symbol approximation: 80th Ann. Internat. Mtg., Soc. Expl. Geophys., 3092–3096.

———, 2012, Seismic wave extrapolation using lowrank symbol approximation: Geophysical Prospecting.

Fornberg, B., 2002, A practical guide to pseudo-spectral methods (cambridge monographs on applied and computational mathematics): Cambridge University Press.

Fowler, P. J., X. Du, and R. P. Fletcher, 2010a, Coupled equations for reverse time migration in transversely isotropic media: Geophysics, **75**, S11–S22.

———, 2010b, Recursive integral time extrapolation methods for scalar waves: 80th Ann. Internat. Mtg., Soc. Expl. Geophys., 3210–3215.

Fowler, P. J., and R. King, 2011, Modeling and reverse time migration of orthorhombic pseudo-acoustic P-waves: 81th Ann. Internat. Mtg., Soc. Expl. Geophys., 190–195.

Fowler, P. J., and C. Lapilli, 2012, Generalized pseudospectral methods for modeling and reverse-time migration in orthorhombic media: 74th Annual EAGE Meeting, EAGE, Expanded Abstracts, AO22.

Gazdag, J., 1981, Modeling of the acoustic wave equation with transform methods: Geophysics, **46**, 854–859.

Geller, R. J., and N. Takeuchi, 1995, A new method for computing highly accurate DSM synthetic seismograms: Geophys. J. Int., **123**, 449–470.

———, 1998, Optimally accurate second-order time domain finite difference scheme for the elastic equation of motion: 1-D case: Geophys. J. Int., **135**, 48–62.

Gray, S. H., and K. J. Marfurt, 1995, Migration from topography: Improving the near-surface image: J. Can. Soc. Expl. Geophys., **31**, 18–24.

Grechka, V., L. Zhang, and J. W. Rector, 2004, Shear waves in acoustic anisotropic media: Geophysics, **69**, 576–582.

Holberg, O., 1987, Computational aspect of the choice of operator and sampling interval for numerical differentiation in large scale simulation of wave phenomena: Geophysical Prospecting, **35**, 629–655.

———, 1988, Towards optimum one-way wave propagation: Geophysics, **36**, 99–114.

Jackson, M. P. A., and C. J. Talbot, 1986, External shapes, strain rates and dynamics of salt structures: Geol. Soc. Am. Bull., **97**, 305–323.

Kindelan, M., A. Kamel, and P. Sguazzero, 1990, On the construction and efficiency of staggered numerical differentiators for the wave equation: Geophysics, **55**, 107–110.

Kosloff, D. D., and E. Baysal, 1982, Forward modeling by a Fourier method: Geophysics, **47**, 1402–1412.

Levin, S. A., 1984, Principle of reverse time migration: Geophysics, **49**, 581–583.

Liu, F., S. A. Morton, S. Jiang, L. Ni, and J. P. Leveille, 2009a, Decoupled wave equations for P and SV waves in an acoustic VTI media: 79th Ann. Internat. Mtg., Soc. Expl. Geophys., 2844–2848.

———, 2009b, Decoupled wave equations for p and sv waves in an acoustic vti media: 79th Ann. Internat. Mtg., Soc. Expl. Geophys., 2844–2848.

Liu, F., G. Zhang, S. A. Morton, and J. P. Leveille, 2011, An effective imaging condition for reverse-time migration using wavefield decomposition: Geophysics, **76**, S29–S39.

Liu, Y., and M. K. Sen, 2009, A new time-space domain high-order finite-difference method for the acoustic wave equation: Journal of computational Physics, **228**, 8779–8806.

———, 2011, Finite-difference modeling with adaptive variable-length spatial operators: Geophysics, **76**, T79–T89.

Loewenthal, D., L. Lu, R. Roberson, and J. Sherwood, 1976a, The wave equation applied to migration: Geophysical Prospecting, **24**, 380–399.

Loewenthal, D., L. Lu, R. Roberson, and J. W. C. Sherwood, 1976b, The wave equation applied to migration: Geophys. Prosp., **24**, 380–399.

Mast, T. D., L. P. Souriau, D. Liu, M. Tabei, A. I. Nachman, and R. C. Waag, 2001, A k-space method for large-scale models of wave propagation in tissue: IEEE Trans. Ultrason. Ferroelect. Freq. Contr., **48**, 341–354.

McClellan, J. H., and T. W. Parks, 1972, Equiripple approximation of fan filters: Geophysics, **37**, 573–583.

McMechan, G. A., 1983, Migration by extrapolation of time-dependent boundary values: Geophys. Prosp., **31**, 413–420.

Mousa, W. A., M. van der Baan, S. Boussakta, and D. C. McLernon, 2009, Designing

stable extrapolators for explicit depth extrapolation of 2D and 3D wavefields using projections onto convex sets: Geophysics, **74**, S33–S45.

Mufti, I. R., J. A. Pita, and R. W. Huntley, 1996, Finite-difference depth migration of exploration-scale 3-d seismic data: Geophysics, **61**, 776–794.

Mulder, W. A., and R. E. Plessix, 2004, A comparison between one-way and two-way wave-equation migration: Geophysics, **69**, 1491–1504.

Pestana, R. C., and P. L. Stoffa, 2010, Time evolution of the wave equation using rapid expansion method: Geophysics, **75**, T121–T131.

Reshef, M., D. Kosloff, M. Edwards, and C. Hsiung, 1988, Three-dimensional acoustic modeling by the Fourier method: Geophysics, **53**, 1175–1183.

REUTERS, 2009, BP makes "giant" oil find in gulf of mexico: http://www.reuters.com/article/GCA-Oil/idUSTRE58133V20090902.

Ristow, D., and T. Ruhl, 1994, Fourier finite-difference migration: Geophysics, **59**, 1882–1893.

Sava, P., and S. Fomel, 2005, Riemannian wavefield extrapolation: Geophysics, **70**, T45–T56.

Shah, H., 2007, The 2007 BP anisotropic velocity-analysis benchmark: 70th Annual EAGE Meeting, EAGE, workshop.

Sheriff, R. E., 2002, Encyclopedic dictionary of applied geophysics: Society of Exploration Geophysics.

Shragge, J., 2008, Riemannian wavefield extrapolation:non-orthogonal coordinate systems: Geophysics, **73**, T11–T21.

Song, J., 2001, The optimized expression of a high dimensional function/manifold in a lower dimensional space: Chinese Scientific Bulletin, **46**, 977–984.

Song, X., and T. Alkhalifah, 2012, Modeling of pseudo-acoustic p-waves in orthorhombic media with lowrank approximation: Geophysics, in review.

Song, X., and S. Fomel, 2011, Fourier finite-difference wave propagation: Geophysics, **76**, T123–T129.

Song, X., S. Fomel, and L. Ying, 2012a, Lowrank finite-differences and lowrank fourier finite-differences for seismic wave extrapolation in the acoustic approximation: Geophysical Journal International, in review.

Song, X., S. Fomel, L. Ying, and T. Ding, 2011, Lowrank finite-differences for wave extrapolation: 81th Ann. Internat. Mtg., Soc. Expl. Geophys., 3372–3376.

Song, X., K. Nihei, and J. Stefani, 2012b, Seismic modeling in acoustic variable-density media by fourier finite differences: 82th Ann. Internat. Mtg., Accepted.

Soubaras, R., 1996, Explicit 3-D migration using equiripple polynomial expansion and laplacian synthesis: Geophysics, **61**, 1386–1393.

Soubaras, R., and Y. Zhang, 2008, Two-step explicit marching method for reverse time migration: 78th Ann. Internat. Mtg., Soc. Expl. Geophys., 2272–2276.

Symes, W. W., 2007, Reverse time migration with optimal checkpointing: Geophysics, **72**, SM213–SM221.

———, 2008, Migration velocity analysis and waveform inversion: Geophysical Prospecting, **56**, 765–790.

Tabei, M., T. D. Mast, and R. C. Waag, 2002, A k-space method for coupled first-order acoustic propagation equations: J. Acoust. Soc. Am., **111**, 53–63.

Takeuchi, N., and R. J. Geller, 2000, Optimally accurate second order time-domain finite difference scheme for computing synthetic seismograms in 2-D and 3-D media: Phys. Earth Planet. Int., **119**, 99–131.

Tal-Ezer, H., D. Kosloff, and Z. Koren, 1987, An accurate scheme for seismic forward modeling: Geophysical Prosecting, **35**, 479–490.

Tarantola, A., 1984, Inversion of seismic reflection data in the acoustic approximation: Geophysics, **49**, 1259–1266.

Technology, O., 2009, Offshore technology - Thunder Horse Field, Gulf of Mexico: http://www.offshore-technology.com/projects/crazy_horse.

Thomsen, L., 1986, Weak elastic anisotropy: Geophysics, **51**, 1954–1966.

Tsvankin, I., 1997, Anisotropic parameters and P-wave velocity for orthorhombic media: Geophysics, **62**, 1292–1309.

———, 2005, Seismic signature and analysis of reflection data in anisotropic media: Elsevier Science.

Tsvankin, I., and V. Grechka, 2011, Seismology of azimuthally anisotropic media and seismic fracture characterization: Society of Exploration Geophysicists.

Versteeg, R., 1994, The Marmousi experience: Velocity model determination on a synthetic complex data set: The Leading Edge, **13**, 927–936.

Wards, B. D., G. F. Margrave, and M. P. Lamoureux, 2008, Phase-shift time-stepping for reverse-time migration, *in* 78th Ann. Internat. Mtg: Soc. of Expl. Geophys., 2262–2266.

Whitmore, N. D., 1983, Iterative depth migration by backward time propagation: 53rd Ann. Internat. Mtg., Soc. Expl. Geophys., 382–385.

Wu, W., L. R. Lines, and H. Lu, 1996, Analysis of high-order, finite-difference schemes in 3-D reverse-time migration: Geophysics, **61**, 845–856.

Xu, S., Y. Zhang, and B. Tang, 2011, 3D angle gathers from reverse time migration: Geophysics, **76**, S77–S92.

Yoon, K., K. J. Marfurt, and W. Starr, 2004, Challenges in reverse-time migration: 74th Ann. Internat. Mtg., Soc. Expl. Geophys., 1057–1061.

Yoon, K., C. Shin, S. Suh, L. R. Lines, and S. Hong, 2003, 3D reverse-time migration using the acoustic wave equation: An experience with the SEG/EAGE data set: The Leading Eage, **22**, 38–41.

Zhan, G., R. C. Pestana, and P. L. Stoffa, 2012, Decoupled equations for reverse time migration in tilted transversely isotropic media: Geophysics, **77**, T37–T45.

Zhang, H., G. Zhang, and Y. Zhang, 2009, Removing S-wave noise in TTI reverse time migration: 79th Ann. Internat. Mtg., Soc. Expl. Geophys., 2849–2853.

Zhang, H., and Y. Zhang, 2008, Reverse time migration in 3D heterogeneous TTI media: 78th Ann. Internat. Mtg., Soc. Expl. Geophys., 2196–2200.

———, 2011, Reverse time migration in vertical and tilted orthorhombic media: 81th Ann. Internat. Mtg., Soc. Expl. Geophys., 185–189.

Zhang, Y., and G. Zhang, 2009, One-step extrapolation method for reverse time migration: Geophysics, **74**, A29–A33.

Zhang, Y., H. Zhang, and G. Zhang, 2011, A stable TTI reverse time migration and its implementation: Geophysics, **76**, WA3–WA9.

Vita

Xiaolei Song was born in Shidao, Weihai, China in April, 1984. She graduated from Rongcheng No.1 High School in Weihai, China in 2002, and went on to complete the degree of Bachelor and Master in Peking University in 2006 and 2008 respectively. She came to The University of Texas at Austin in 2008 to pursue the degree of doctor in Geophysics.

Permanent address: 9801 Stonelake Blvd, Austin, TX 78759

This dissertation was typeset with LaTeX[†] by the author.

[†]LaTeX is a document preparation system developed by Leslie Lamport as a special version of Donald Knuth's TeX Program.